# Transition of wire-disturbed cylinder wake flow

PROEFSCHRIFT

ter verkrijging van de graad van doctor aan de
Technische Universiteit Eindhoven, op gezag van de
rector magnificus, prof.dr.ir. C.J. van Duijn, voor een
commissie aangewezen door het College voor
Promoties in het openbaar te verdedigen
op maandag 27 juni 2011 om 16.00 uur

door

İlhan Yıldırım

geboren te Lofça, Bulgarije

Dit proefschrift is goedgekeurd door de promotor:

prof.dr.ir. A.A. van Steenhoven

Copromotor:
dr.ir. C.C.M. Rindt

Cover design by Atike Dicle Pekel Duhbaci, *Atike Design, Eindhoven.*

# Contents

# Introduction

## 1.1 Background

Nature comprises a lot of examples of fluid flows around objects. Most of these examples are characterized by wakes involving the chaotic motions of eddies, which attracted scientists for many centuries. An illustration of such a wake flow in nature is the von Kármán vortex street observed in the atmosphere as shown in Figure 1.1a. The flow patterns around the Alejandro Selkirk Island of the Juan Fernandez Islands (also known as Robinson Crusoe Islands) are made visible by the clouds. The wind blowing above the ocean surface is disturbed by a 1640 m high mountain on the island and a vortex street is created.

Knowledge of bluff body wake flows has a great importance for many engineering applications. Therefore, it has become a favorite topic of research for centuries. For example, the pioneering work of Leonardo da Vinci provided insight into fluid dynamics through many sketches of vortical patterns around bridge legs as shown in Figure 1.1b and initiated the development of fluid dynamics as a scientific field [2].

One reason for the importance of wake flow analysis is due to the vortex induced vibration at a particular frequency. A classical example of this phenomenon is the Tacoma Bridge incident happened in 1940. The bridge collapsed because the wake caused the bridge structure to oscillate at its natural frequency, see Figure 1.2(left). The influence of the wakes on transport properties, such as heat and momentum, is another important aspect of wake flow analysis. For example, placing another cylinder in proximity can influence the heat transfer from a cylinder, a typical configuration found in electronic cooling systems, see Figure 1.2, and heat exchangers. Wake interactions also affect the fluid forces acting on a body as well as they can enhance

(a)                                                                    (b)
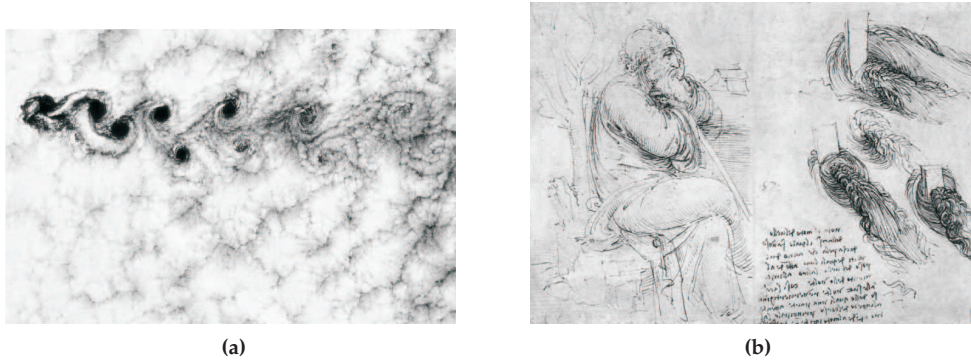
**Figure 1**.**1:** *Flow behind bluff bodies; (a) Cloud visualization of von Kármán vortex street around the Alejandro Selkirk Island. (Figure is reproduced from DeFelice et al. [1]) (b) The sketches of Leonardo da Vinci showing the eddies passing bridge legs.*
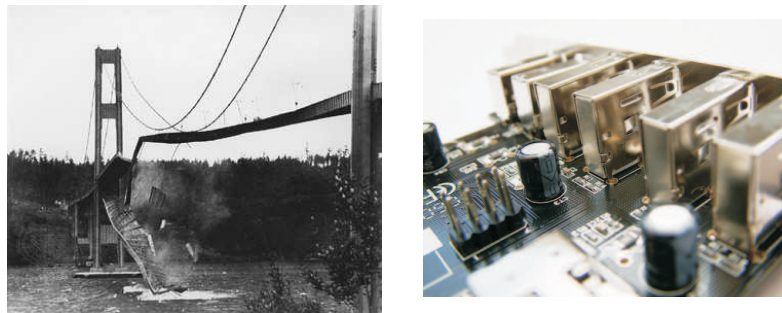


**Figure 1**.**2:** *Two examples for importance of wake analysis for engineering applications; Left: Tacoma bridge, Right: A typical electronic circuit board with several bluff body structures.*

noise generation. Race cars and aircraft landing gears are two typical examples of such type of configurations. Therefore, the knowledge about wake vortices is important in the design of a wide range of structures, such as the ones given above, submarine periscopes, chimneys, skyscrapers etc.

Due to its simple geometry, the flow around circular cylinders has become a central topic in many researches. One of the first studies on the stability of cylinder wake flows was performed by von Kármán at the beginning of the twentieth century. He modeled the wake using a point vortex approach and determined the necessary criterion for the stability of the wake. von Kármán 's approach was discussed in detail by Lamb [3]. Roshko [4, 5] performed extensive experimental studies on cylinder wakes using hot-wire anemometry. He measured the shedding frequencies at a wide range of Reynolds numbers and suggested a universal relation between the

Reynolds number and the shedding frequency. A lot of effort was made to explain the physics of circular cylinder wake dynamics. The physical mechanism of two-dimensional vortex shedding is discussed in the works of Gerrard [6, 7], Green and Gerrard [8]. They showed that vortex shedding for low Reynolds numbers can be characterized by vortex splitting and high shear stress occurring in the near-wake. Unal and Rockwell [9] investigated the near wake vortex formation from the context of absolute instability and showed that the shear layer separating from the cylinder shows an exponential variation of fluctuating kinetic energy with distance downstream of the cylinder.

However, the above mentioned studies were limited to the two-dimensional aspects of the flow. The three-dimensional aspects of wake flows behind circular cylinders are thoroughly reviewed and discussed by Williamson [10, 11]. He grouped the circular cylinder flow into various regimes according to the Reynolds number. The laminar vortex shedding regime extends from a Reynolds number of $49$ to $140 - 194$ and the flow regime between $Re = 190$ and $260$ is denoted as the three-dimensional wake transition regime. This regime is associated with two modes of shedding, Mode-A and Mode-B.

It is shown in various studies that under the influence of 'disturbances' cylinder wake flows exhibit different flow structures. For example, Ren et al. [12] showed that by heating the cylinder a different transition regime can be found which was named as Mode-E. Zhang et al. [13] studied the influence of the presence of a wire in the vicinity of a cylinder on transition and characterized the wake transition regime as Mode-C, which shows different properties than Mode-A and Mode-B. For the case of a rotating cylinder, it was shown by Stojkovic et al. [14] that there exist two shedding modes, Shedding Mode I and Shedding Mode II. Shedding Mode I is associated with a deflected von Kármán vortex street while Shedding Mode II shows the formation of a single vortex shed with a much lower frequency than for Shedding Mode I.

## 1.2   Classification of secondary flows in cylinder wakes

In cylinder wake terminology, 'primary instability' usually refers to the instability which results in the formation of von Kármán vortex shedding. The term 'secondary instability' is attributed to the instability mechanism which occurs in the transition of a cylinder wake from two-dimensions to three-dimensions by the generation of streamwise, i.e. secondary, vortical structures.

### 1.2.1   Mode-A and Mode-B

The wake transition of a circular cylinder was originally described by Roshko [4]. His study was mainly based on hot-wire measurements of a cylinder wake. He identified the Reynolds number range $150 < Re < 300$ as the 'transition range' based on the
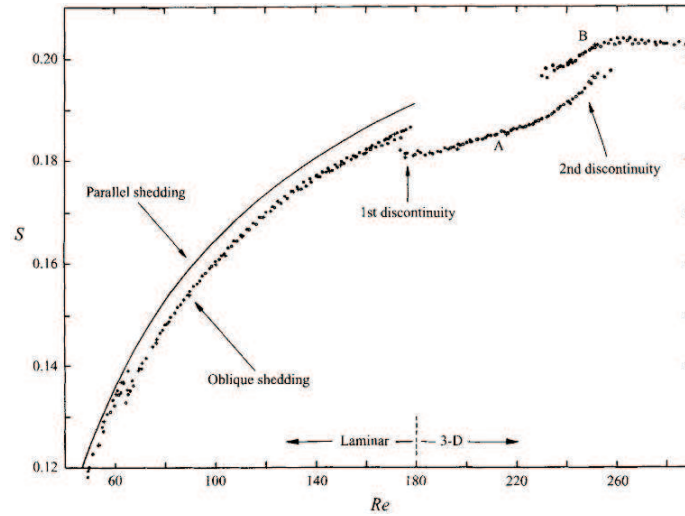
**Figure 1.3:** *Strouhal number Reynolds number relationship in laminar and transition regimes. (Figure is reproduced from Williamson [11])*

irregularities in the velocity signals. Hama [15] showed that in this Reynolds number range the von Kármán vortices are forming three-dimensional wavy structures. However, not until Williamson [16], the transition regime was associated with the discontinuities in the Strouhal-Reynolds number (St-Re) curve as shown in Figure 1.3. Experiments of Williamson [16] showed that the cylinder wake transition occurs via the generation of secondary vortices in the wake at the corresponding Reynolds number of the discontinuities. He suggested two different modes for the cylinder transition regime, namely Mode-A and Mode-B, each having distinct properties.

Mode-A is associated with the first discontinuity in the St-Re curve where there is a drop in shedding frequency. At this stage of the flow, the primary vortices deform in a wavy fashion along their length during the shedding process. This results in the local spanwise formation of vortex loops, which become stretched in the braid region of the primary vortices to form streamwise vortex pairs, as shown in Figure 1.4 (left). This type of wake transition can be seen over the Reynolds number range of $160 < Re < 240$ with a characteristic spanwise wavelength of $3 - 4$ cylinder diameters. Mode-A transition also exhibits dislocations and complex temporal behavior [11, 17]. Williamson [11] proposed that Mode-A originates from an elliptic instability of the vortex cores in the near-wake. This theory was further investigated in Leweke and Williamson [18] and Thompson et al. [19]. Another approach of describing the onset of the vortex loops is provided by Brede et al. [20]. They identified a centrifugal instability of the braid region between the primary vortices using the analysis of particle image velocimetry data. The conclusion of Brede et al. [20] was that the
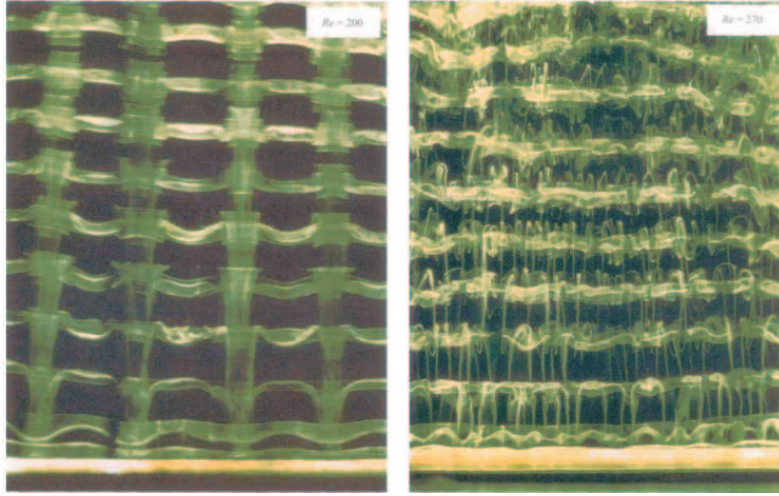
**Figure 1.4:** *Top-views of Mode-A (left) transition at $Re = 200$ and Mode-B (right) transition at $Re = 270$. (Figure is reproduced from Williamson [10]).*

interaction of the primary vortices in this braid region is the main amplification mechanism.

On the other hand, for Reynolds numbers $Re \geq 240$, the flow goes into a different state named as Mode-B, see Figure 1.4 (right). This state is characterized by formation of fine-scale streamwise vortices with a spanwise wavelength of approximately one cylinder diameter. Mode-B is associated with the second discontinuity in the St-Re curve where there is an increase in the shedding frequency. The onset of Mode-B transition was discussed as the manifestation of a hyperbolic instability in the braid shear layers [11, 18, 19]. Brede et al. [20] concluded that Mode-B vortices originate from the instability of the separating shear layer in the near-wake which results in a different topology of the Mode-B vortices than those in Mode-A.

Furthermore, linear [21] and nonlinear [22, 23] numerical stability computations have provided quantitative data by establishing precise stability limits for the two-dimensional flow. Mode-A appears at $Re = 189$ where the two-dimensional wake becomes linearly unstable to three-dimensional disturbances with a spanwise wavelength of $\lambda_z/D = 3.96$ [21, 23]. Mode-A instability is subcritical with a small range of hysteresis [16, 21]. Later, Barkley et al. [24] showed that this hysteresis of Mode-A extends down to $Re \simeq 180$.

Stability results of Mode-B shedding indicate that the two-dimensional wake becomes linearly unstable at $Re = 259$ with a spanwise wavelength $\lambda_z = 0.82$ [21]. Unlike Mode-A, this bifurcation is supercritical and without a hysteresis [23]. The branch of Mode-B solutions bifurcates in the direction of increasing Reynolds number and pure Mode-B states do not exist below this Reynolds number as shown in
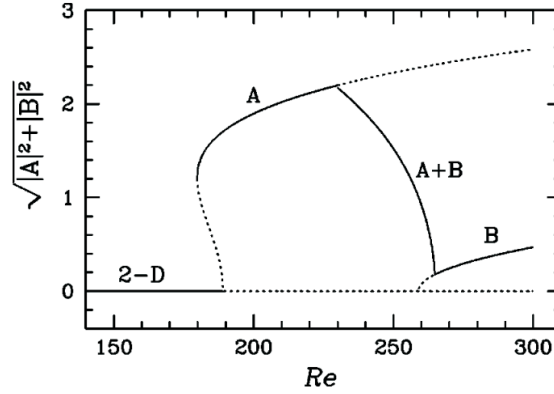
**Figure 1.5:** *Bifurcation diagram for amplitude equations. Shown are the steady states for these equations with solid lines indicating stable states. The 2D branch has $A = B = 0$. The A branch has $B = 0$, the B branch has $A = 0$, and the $A + B$ branch is a mixed-mode branch with both $A, B \neq 0$. The norm is $\sqrt{A^2 + B^2}$. (Figure and caption are reproduced from Barkley et al. [24].)*

Figure 1.5.

The transition from Mode-A to Mode-B occurs over the Reynolds number range $Re = 210 - 270$. During this transition, the flow energy is shifting gradually from Mode-A to Mode-B [11, 16, 23]. The low-dimensional model of Barkley et al. [24] on mixed-mode transition scenario showed that the transition is not hysteretic, rather it is a reversible interpolation between Mode-A and Mode-B, see Figure 1.5. The consequence of this interaction is that Mode-A has a destabilizing effect on Mode-B and Mode-B has a stabilizing effect on Mode-A.

Besides Mode-A and Mode-B, another quasi-periodic three-dimensional insta-bility of the circular cylinder wake was predicted by Barkley and Henderson [21]. Subsequently, Blackburn et al. [25] showed that this instability is the third state to bi-furcate from a two-dimensional base state with increasing Reynolds number, which shows itself as a traveling wave in the weakly nonlinear case. The quasi-periodic bifurcation occurs at $Re \approx 377$ with $\lambda_z/D \approx 1.8$ [25].

## 1.2.2 Mode-E

By heating the cylinder a different transition regime can be found in the wake of a circular cylinder which was named as Mode-E by Ren et al. [12].

Maas et al. [26] showed that for a horizontally placed heated cylinder a three-dimensional transition in the wake flow occurs at Richardson number $Ri > 0.3$ and $Re = 117$. The transition takes places in the wake via escaping thermal plumes from the primary vortices as exemplified for $Ri = 1$ in Figure 1.6. Maas et al. [26] measured the average spanwise wavelength of the vortical structures around 1.8 D.
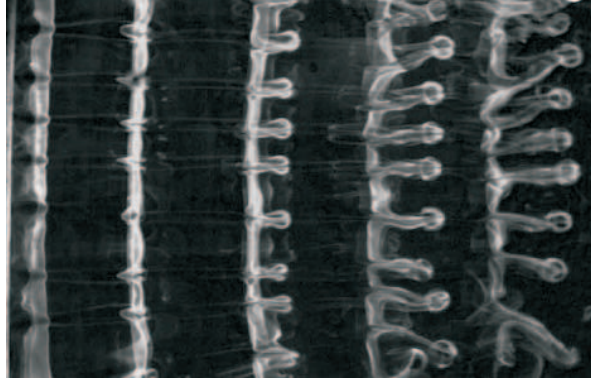
**Figure 1**.6: *Top-view of Mode-E transition in heated cylinder wake with $Ri = 1.0$, $\lambda_z = 1.8D$, $Re = 117$. The cylinder is located at the bottom and the flow is from left to right. (Figure is reproduced from Maas et al. [26])*

Further physical description of the wake was made by Ren et al. [27]. They showed that the vortex formation process is different for the 'in-plume' position (where the plume escapes further downstream) and the 'out-of-plume' position. For the 'in-plume' positions an upward motion occurs directly behind the cylinder, which separates the vortices from the cylinder wall and enhances the formation of the upper vortices and weakens the formation of the lower ones.

The three-dimensional transition by escaping mushroom type structures, i.e. thermal plumes, was also found for $Re = 85$ and $Ri = 1$ [12]. Ren et al. [12] further discussed the transition mechanism for Mode-E as the manifestation of mushroom-type structures in the far-wake and $\Lambda$-shaped structures in the near-wake. At the intermediate stage a characteristic lift-up process takes place in the center region between the legs and head of the $\Lambda$-shaped structures which results in the extraction of hot fluid out of the upper vortex core. Due to this lift-up process, mushroom-type structures are generated in the form of escaping vortex rings in the far-wake. Furthermore, Ren et al. [12] showed that the whole Mode-E transition is a self-sustaining cyclic process which starts with the generation of streamwise vorticity due to a spanwise temperature gradient.

### 1.2.3 Mode-C

There is an other three-dimensional transition pattern observed in bluff-body wakes. This mode is named as Mode-C after Zhang et al. [13] and has been observed in several flow configurations, such as wire disturbed cylinder wakes, flows behind rings, cylinder-cylinder interactions.

The first evidence of Mode-C appeared in the computations and experiments of
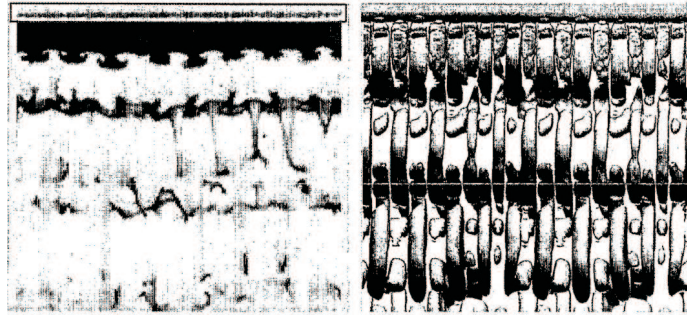
**Figure 1.7:** *Flow visualization (left) and numerical simulation(right) of Mode-C transition in wired cylinder wake. The cylinder is located at the top and the flow is from top to bottom. (Figure is reproduced from Zhang et al. [13])*

Zhang et al. [13] when a tiny wire was placed close to a circular cylinder, see Figure 1.7. In their flow visualization experiments, they observed that Mode-C transition takes place over a Reynolds number range of $170 < Re < 270$. Numerical simulations at $Re = 210$ displayed a spanwise periodicity of $1.8$ cylinder diameters. They found a larger decrease in shedding frequency than Mode-A at the same Reynolds number when compared to their corresponding two-dimensional flows. Furthermore, based on the velocity spectra obtained from hot-film measurements, they proposed that the Mode-C flow goes into a three-dimensional periodic stage at $Re = 170$ and into a quasi-periodic stage at $Re = 200$. To clarify the effect of a symmetric disturbance, Zhang et al. [13] performed numerical simulations for the case of symmetrically placed wires, which showed a Mode-C transition pattern with a spanwise wavelength of $2.2$ cylinder diameters.

Another flow type where Mode-C transition takes place is the flow behind circular rings as shown in Figure 1.8. Using Floquet stability calculations, Sheard et al. [29] identified this mode as the primary transition mode in the aspect ratio (AR) range of $3.9 \lesssim AR \lesssim 8$, with a spanwise wavelength of approximately $1.7$ ring cross-section diameters. They suggested that a subharmonic Mode-C instability occurs as a result of the asymmetry about the wake centerline imposed by the curvature of the wake. Further nonlinear characterization of Mode-C was made by Sheard et al. [28] using Direct Numerical Simulations. They showed that for the flow past a ring with $AR = 5$, Mode-C instability produces a period-doubling in the wake through supercritical and non-hysteretic transition. A typical vorticity pattern for Mode-C transition is shown in Figure 1.8b. Subsequently, Sheard et al. [30] provided additional computational results and first experimental observations about the existence of the subharmonic mode Mode-C. Later, Sheard et al. [31] showed that the period-doubling nature of the wake is maintained by a cycle of convection of the perturbation vorticity from the near-wake.
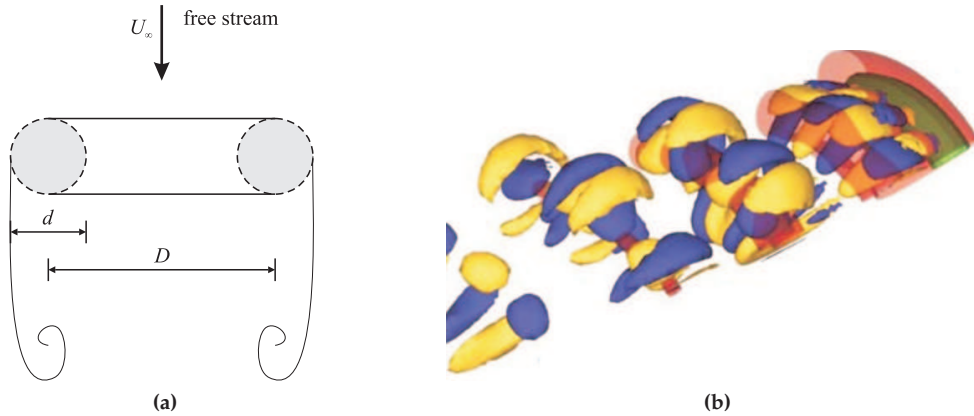
**Figure 1**.**8:** *Flow behind rings. (a) Diagram for flow behind rings. Aspect ratio is defined as $AR = D/d$ (b) Mode-C transition in ring flow with $AR = 5$, $\lambda_d = 2d$, $Re = 170$. (Figure is reproduced from Sheard et al. [28])*

Carmo et al. [32] also found Mode-C in the wake transition of the flow around staggered arrangements of equi-diameter circular cylinders for different relative positions. The structure and onset characteristics of Mode-C were analyzed using linear and non-linear stability analyses as well as Direct Numerical Simulations. They showed that Mode-C appears in the near-wake of the downstream cylinder with an intermediate spanwise wavelength between Mode-A and Mode-B with a period-doubling character.

### 1.2.4 Rotating cylinder wake

The rotation of a cylinder in a uniform flow modifies the wake flow patterns and vortex shedding. The rotation effect results in an acceleration of the flow on one side and a deceleration on the other side. Hence, the pressure on the accelerated side becomes lower than that on the decelerated side, resulting in a mean lift force. Such a phenomenon is referred to as the Magnus effect and rotating cylinder configuration has been subject of interest for many researchers [14, 33–38].

Previously, it has been shown numerically and for low rotation rates also experimentally that for a rotating cylinder there exist two instability areas where the vortex shedding is not suppressed [14, 33, 35, 37, 38]. These instability areas are indicated as Shedding Mode I and Shedding Mode II. Shedding Mode I shows the classic von Kármán Vortex Street, which becomes asymmetric when the cylinder is rotating. On the other hand, Shedding Mode II is associated with single shed vortex which has one-order-of-magnitude lower shedding frequency and is found numerically only in a narrow range of the rotation rate [14]. There is no experimental evidence of the

existence of this mode.

## 1.3   Objectives

On the basis of previous investigations, it is clear that disturbances alter the vortex shedding patterns in the transitional regime of a circular cylinder. The natural modes of shedding, namely Mode-A and Mode-B, have been investigated extensively by many researchers. In the last decade, Mode-C transition around rings has drawn much attention due to its unique characteristics and there is a comprehensive numerical literature about it. However, a detailed knowledge of the flow physics based on experimental observations is lacking for the case of a cylinder with a control wire nearby, for which Mode-C is originally shown by Zhang et al. [13], as well as for Shedding Mode II of the rotating cylinder case. This thesis aims to scientifically contribute to the knowledge of wake modification of circular cylinders in those areas.

   Therefore, the main objectives of this thesis are as follows:

- Characterizing the laminar two-dimensional wake flow for the wired cylinder case, investigating its vortex characteristics and vortex shedding process.

- Investigating the wake flow for the wired cylinder case in the transition regime, verifying Mode-C type transition, examining its period-doubling character and establishing a physical explanation for the existence of period-doubling.

- Characterizing the wake transition using fluctuating flow properties and energy content of the wake as well as vortex characteristics.

- Investigating the secondary instability region of rotating cylinders and experimentally validating the so-called Shedding Mode II.

## 1.4   Thesis outline

Chapter 1 gives a brief introduction on the secondary instabilities in circular cylinder wakes.

   In Chapter 2, an overview of methodology used in the research is given. After introduction of the problem and governing equations, a brief introduction of the Spectral Element method is given. The experimental part of this research involves the usage of Electrolytic Tin-precipitation method and Particle Image Velocimetry to obtain qualitative and quantitative information, respectively.

   Chapter 3 focuses on the effect of a wire on the laminar two-dimensional flow. For that purpose the flow at $Re = 100$ has been investigated numerically. The effect of different wire positions on velocity fluctuations and shedding frequency is

given. Vortex dynamics of wired cylinder wake is examined using the Point Vortex approach. Individual vortex strengths and trajectories are presented.

In Chapter 4, analysis of period-doubling mechanism in Mode-C transition is presented. The wire is fixed at a position of $(x_w/D, y_w/D) = (0.75, 0.75)$ with respect to the cylinder center. Experimental results are used to examine the period-doubling character of the wake and to establish a physical explanation for the existence. The results are assessed using velocity fluctuation characteristics, shedding frequency and vorticity patterns.

Chapter 5 concentrates on the characterization of the Mode-C wake transition. The discussion of Chapter 4 is extended by investigating the fluctuating flow properties and energy characteristics of Mode-C wake. Discrete energy components of Mode-C wake at particular frequencies are calculated using the energy spectrum obtained from PIV experiments. Vortex strengths and trajectories are presented for the transition regime. Furthermore, the change in shedding frequency is associated with the wire effecting the separating shear layer.

In Chapter 6, experimental results of the Shedding Mode II are presented. The flow field is investigated qualitatively using flow visualization experiments and quantitatively using side-view PIV measurements. Instantaneous vorticity patterns are used to evaluate vortex shedding. Shedding frequencies are compared to the literature values.

Finally in Chapter 7, the conclusions of this study are summarized and recommendations for future research are presented.

# Research Methodology

## 2.1 Problem definition

The present investigation mainly focuses on the wake flow of a circular shaped cylinder with a near-wake wire disturbance. The configuration consists of two circular cylinders with diameters $D$ and $d$, respectively, as shown in Fig. 2.1a. The corresponding diameter ratio is $D/d = 50$ in the numerical simulations and $D/d = 100$ in the experiments. Since the diameter ratio is quite large, the smaller cylinder will be denoted as a wire throughout the text.

The position of the wire is determined in a Cartesian coordinate system $(x, y, z)$ whose origin is at the center of the main cylinder. The coordinates $(x_w, y_w)$ represent the position of the wire with respect to the center of the cylinder. The freestream velocity $U_\infty$ is in the $+X$ direction which is denoted as the streamwise direction in Figure 2.1b. The figure also shows the global coordinate system with corresponding axis labels as well as the vorticity vector $\boldsymbol{\omega} = (\omega_x, \omega_y, \omega_z)$ with corresponding rotation directions.

The Reynolds number $Re = DU_\infty/\nu$ for the main cylinder is $Re \approx \mathcal{O}(10^2)$ in this study. Considering the diameter ratio between the cylinder and the wire, the Reynolds number for the wire is $Re \approx \mathcal{O}(1)$ which indicates that no vortex shedding occurs from the wire itself.

In the remainder of this chapter, the methodology used in the present research will be discussed briefly. Firstly, the governing equations are summarized. Secondly, a summary of the numerical method, including temporal and spatial discretization and computational details, is presented. Thirdly, a brief overview of the experimental system, measurement configurations and techniques is given. Finally, the basics of the Point Vortex model are summarized.
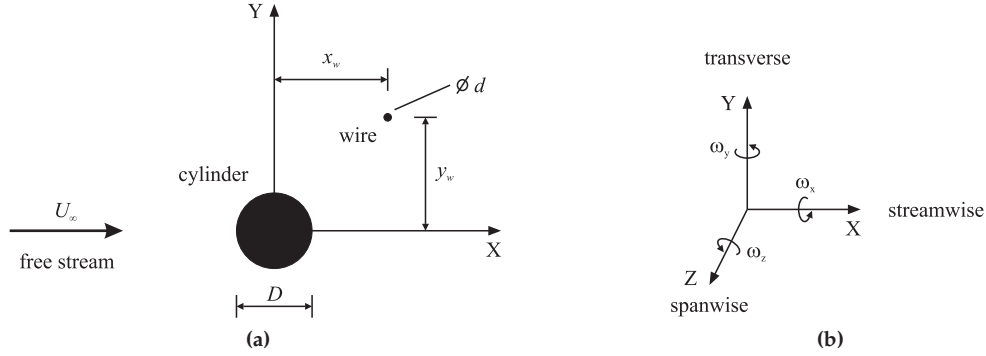
**Figure 2**.1: *Presentation of (a) Cylinder-wire configuration, (b) Global coordinate system and axis labels.*

## 2.2 Governing equations

The flow around a cylinder is governed by the Navier-Stokes equation for an incompressible and Newtonian fluid. The differential form of the mass and momentum conservation equations are:

$$\boldsymbol{\nabla} \cdot \boldsymbol{u} = 0 \tag{2.1}$$

$$\frac{\partial \boldsymbol{u}}{\partial t} + (\boldsymbol{u} \cdot \nabla)\boldsymbol{u} = -\frac{1}{\rho}\nabla p + \nu\nabla^2 \boldsymbol{u} \tag{2.2}$$

In the equations $\boldsymbol{u} = (u, v, w) = u\boldsymbol{i} + v\boldsymbol{j} + w\boldsymbol{k}$ is the velocity vector, $\rho$ represents the density, $p$ the pressure, $t$ the time and $\nu$ the kinematic viscosity.

The Equations 2.1 and 2.2 can be converted into non-dimensional form by introducing the following dimensionless variables;

$$\boldsymbol{x}^* = \frac{\boldsymbol{x}}{D}, t^* = \frac{tU_\infty}{D}, \boldsymbol{u}^* = \frac{\boldsymbol{u}}{U_\infty}, p^* = \frac{p - p_\infty}{\rho U_\infty^2} \tag{2.3}$$

Substituting these dimensionless variables into Equations 2.1 and 2.2 results in the non-dimensional form of the convervation equations:

$$\boldsymbol{\nabla} \cdot \boldsymbol{u} = 0 \tag{2.4}$$

$$\frac{\partial \boldsymbol{u}}{\partial t} + (\boldsymbol{u} \cdot \boldsymbol{\nabla})\boldsymbol{u} = -\nabla p + \frac{1}{Re}\nabla^2 \boldsymbol{u} \tag{2.5}$$

For simplicity the asterisks have been removed from the non-dimensional variables in the equations.

The vorticity is defined as the curl of the velocity, $\boldsymbol{\omega} = \nabla \times \boldsymbol{u}$. The result of this

operation is the vorticity vector of the form $\boldsymbol{\omega} = (\omega_x, \omega_y, \omega_z) = \omega_x \boldsymbol{i} + \omega_y \boldsymbol{j} + \omega_z \boldsymbol{k}$. The vorticity components can be written as:

$$\boldsymbol{\omega} = \left( \frac{\partial w}{\partial y} - \frac{\partial v}{\partial z}, \frac{\partial u}{\partial z} - \frac{\partial w}{\partial x}, \frac{\partial v}{\partial x} - \frac{\partial u}{\partial y} \right) \tag{2.6}$$

The vorticity components represent the local rotation of a fluid element with respect to the corresponding axis which are shown in Figure 2.1b.

The equation for the rate of change of vorticity is obtained by taking the curl of Equation 2.5. After some vector manipulations and in the absence of the density effects, the equation for vorticity transport then becomes

$$\underbrace{\frac{\partial \boldsymbol{\omega}}{\partial t} + (\boldsymbol{u} \cdot \nabla)\boldsymbol{\omega}}_{\text{I}} = \underbrace{(\boldsymbol{\omega} \cdot \nabla)\boldsymbol{u}}_{\text{II}} + \underbrace{\frac{1}{Re} \nabla^2 \boldsymbol{\omega}}_{\text{III}} \tag{2.7}$$

where the terms I-III have the following physical significance:

**Term I:** This term describes the material derivative of vorticity. The rate of change of vorticity of a fluid element corresponds to the angular acceleration of the fluid particle, which can change due to the unsteadiness in the flow or due to the motion of the fluid particle as it moves from one point to another.

**Term II:** This term represents the rate of change of vorticity due to vortex stretching and tilting. This term vanishes in two-dimensional flows.

**Term III:** This term represents the rate of change of vorticity due to diffusion.

## 2.3 Numerical method

Two-dimensional numerical simulations are used for the flow assessment in the laminar two-dimensional flow regime. The unsteady Navier-Stokes equations are solved using an operator splitting approach in combination with a pressure correction method. In this solution technique velocity and pressure terms are decoupled, yielding a convection-diffusion problem for the velocity terms $u$ and $v$ (in the two-dimensional case) and a Poisson equation for the pressure related correction term $p^*$. This solution procedure was proposed and implemented by Timmermans [39] and Timmermans et al. [40]. Later, this procedure was used by Kieft et al. [41] and extended by Ren et al. [12] for mixed-convection problems. A brief overview of the temporal and spatial discritization techniques is given below. Further details and the step-by-step solution procedure can be found in Timmermans [39], Timmermans et al. [40], Kieft [42] and Ren [43].
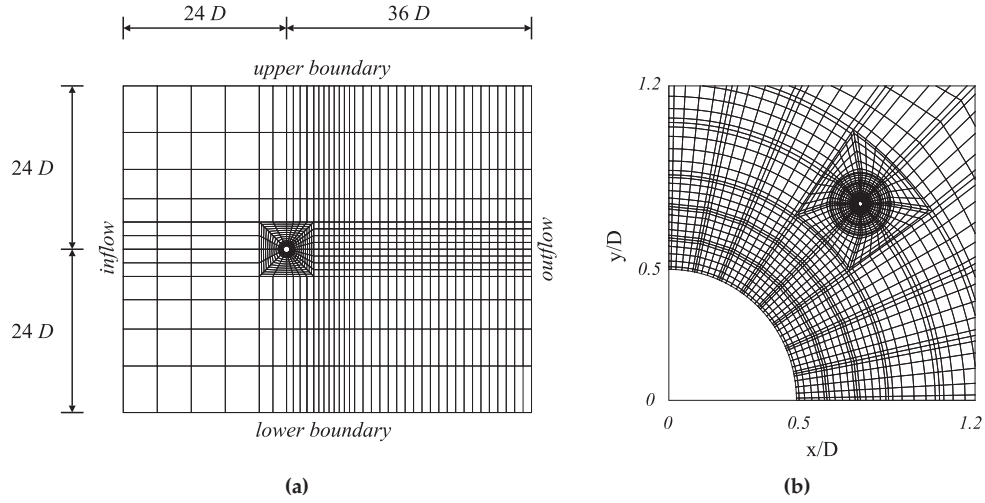
**Figure 2.2:** *Domain and grid properties. (a) Quadrilateral elements, domain size and boundary locations of the whole domain, (b) Quadrilateral elements and calculation points around the wire. The solution in each element is approximated with $6^{th}$-order polynomials.*

## 2.3.1   Temporal discretization

For the temporal discretization the operator splitting approach is used [43]. The governing discretized set of equations is integrated forward in time using different time steps. The convection term is treated differently than the diffusion and pressure terms due to its nonlinear nature. The convection equation is integrated forward in time by an explicit third-order Taylor-Galerkin scheme, which contains three explicit time steps within one implicit time step. The diffusion equation is treated implicitly using a second-order Backward Difference scheme. Because of the memory storage limitations, an iterative technique is used and the solution of the linear system is obtained using a pre-conditioning conjugate gradient method.

The pressure term is treated using a pressure-correction method. An intermediate velocity is calculated taking the pressure at the former time step. However, the calculated velocity field is not divergence-free. Hence, it is used to determine a pressure related correction term, $p^*$. For this, a pressure Poisson equation is formed for $p^*$, by taking the divergence of the equation for the pressure difference of the last two time steps and by enforcing the incompressibility constraint. Later this pressure related correction term is used to calculate a corrected divergence-free velocity field.

| | | | |
|---|---|---|---|
| inflow | $u = 1$ | $v = 0$ | $\partial p^*/\partial n = 0$ |
| outflow | $\partial u/\partial n = 0$ | $\partial v/\partial n = 0$ | $p^* = 0$ |
| upper & lower | $\partial u/\partial n = 0$ | $v = 0$ | $\partial p^*/\partial n = 0$ |
| cylinder & wire | $u = 0$ | $v = 0$ | $\partial p^*/\partial n = 0$ |

**Table 2**.1: *Boundary conditions for the calculation domain. $u$ and $v$ denote, respectively, the horizontal and vertical velocity components and $p^*$ is the pressure related correction term. $\partial/\partial n$ denotes the normal derivative.*

### 2.3.2 Spatial discretization

A high-order Spectral Element Method (SEM) is used for the spatial discretization of the conservation equations [44]. A typical grid is shown in Figure 2.2. SEM can be considered as a combination of a Finite Element Method (FEM) and a Spectral Method (SM). It combines the advantages of FEM and SM. FEM brings its advantage of flexibility in the decomposition of complex domains into elements. The use of high-order approximation functions within such an element as in SM results in spectral convergence and high accuracy [42].

The principle of SEM is rather straightforward. The matrix equations for the approximate solution at the nodal points are constructed using the Galerkin Finite Element Method. The integrals of the flow equations are multiplied by the local weighting functions and evaluated using Legendre-Gauss-Lobatto quadrature [45].

### 2.3.3 Boundary conditions

The boundary locations are shown in Figure 2.2a and the prescribed boundary conditions are summarized in Table 2.1. Dirichlet boundary conditions are used for the velocity components at the inflow. A no-slip constraint is applied for the cylinder and wire surfaces. The normal velocity at the upper and lower boundaries is set to zero, $v = 0$. In combination with $\partial u/\partial n = 0$, this implies a zero tangential stress at these boundaries. At the outflow boundary, homogeneous Neumann boundary conditions are applied for both of the velocity components.

The pressure correction scheme requires the use of homogeneous Neumann boundary conditions for the pressure Poisson equation except for the outflow where the use of stress-free boundary conditions for the velocity imposes $p^* = 0$.

### 2.3.4 Computational details

The configuration that has been studied consists of two circular cylinders with diameters $D$ and $d$ respectively, as given in Figure 2.1a. The corresponding diameter ratio in the numerical simulations is $D/d = 50$. This diameter ratio is two times the experimental value due to the computational consideration. The domain size

| $Re$ | $N_{elem}$ | $N_{point}$ | $U_\infty$ | $\Delta t$ |
|------|-----------|------------|-----------|-----------|
| 80   | 1230      | 44766      | 0.8       | 0.03      |
| 100  | 1230      | 44766      | 1.0       | 0.03      |
| 120  | 1230      | 44766      | 1.2       | 0.03      |

**Table 2**.**2:** *Computational details for the non-wired cases.*

| $x_w/D$ | $y_w/D$ | $N_{elem}$ | $N_{point}$ | $U_\infty$ | $\Delta t$ |
|---------|---------|-----------|------------|-----------|-----------|
| 0.75    | 0.5     | 932       | 33965      | 1.0       | 0.004     |
| 0.75    | 0.625   | 932       | 33965      | 1.0       | 0.004     |
| 0.75    | 0.75    | 932       | 33965      | 1.0       | 0.004     |
| 0.75    | 0.875   | 932       | 33965      | 1.0       | 0.004     |
| 0.75    | 1.0     | 982       | 35765      | 1.0       | 0.004     |
| 0.75    | 1.5     | 946       | 34457      | 1.0       | 0.004     |
| 0.75    | 2.0     | 984       | 35837      | 1.0       | 0.004     |
| 0.5     | 0.875   | 1378      | 50117      | 1.0       | 0.004     |
| 0.625   | 0.875   | 1288      | 46865      | 1.0       | 0.004     |
| 0.875   | 0.875   | 1362      | 49541      | 1.0       | 0.004     |
| 1.0     | 0.875   | 1400      | 50909      | 1.0       | 0.004     |

**Table 2**.**3:** *Computational details for the wired cases. [$Re = 100$].*

is chosen such that the wake flow region under consideration is not influenced by the boundaries. Ren [43] performed an extensive study on the effect of the domain size on the accuracy of solution. Based on his study, the dimensions of the two-dimensional calculation domain are chosen as $60D \times 48D$, as shown in Figure 2.2a. The cylinder has been placed $24D$ downstream of the inflow and $24D$ away from the upper and lower boundaries. The same domain size is used for all of the two-dimensional simulations.

The simulation parameters are presented in Tables 2.2 and 2.3 for non-wired and wired cases, respectively. The calculation domain is decomposed into $N_{elem} = \mathcal{O}(10^3)$ quadrilateral elements for the non-wired case and the wired cases. For each element the solution is approximated by using a sixth-order polynomial expansion. Thus, within each element there are $7 \times 7$ calculation points resulting in a total number of calculation points of $N_{point} = \mathcal{O}(10^5)$. After a trial simulation for the $(x_w/D, y_w/D) = (0.75, 0.75)$ case, it is concluded that increasing grid resolution to $N_{elem} \approx 60000$ does not change the accuracy of the results much. Due to the necessity of using a smaller time step for the wired case, a lower grid resolution is used to keep the computational costs reasonable. Non-dimensional time steps of $0.03$ and $0.004$ are used for the non-wired and wired cases, respectively. These time steps correspond to a Courant number of approximately $0.3$ for both cases.

| Reference | Method | Strouhal number $St = f_{shed}D/U_\infty$ |
|---|---|---|
| Williamson [46] | experimental | 0.165 |
| Williamson and Brown [47] | experimental, curve fit $St = 0.2665 - 1.018/\sqrt{Re}$ | 0.165 |
| Mittal and Raghuvanshi [48] | numerical | 0.168 |
| Present study | numerical | 0.166 |

**Table 2**.**4:** *Comparison of Strouhal numbers for flow past a circular cylinder for a Reynolds number of $Re = 100$.*

In addition, special care was taken for the elements on the surface of both the main cylinder and the wire in order to represent the geometry accurately. Especially the grid around the wire had to be fine enough to resolve the shear layers around it, as seen in Figure 2.2b. From Table 2.3, it can be seen that for the wired cases of $(x_w/D, y_w/D) = (0.5 - 1.0, 0.875)$ larger number of elements are used. This is due to the fact that for those cases embedding a relatively fine mesh into a relatively coarse mesh needed better special treatment to keep the element aspect ratio close to $1$.

As an extra validation of the simulation results, the non-dimensional shedding frequency is compared to the values in literature [46–48] as shown in Table 2.4. The comparison has been performed for the shedding frequency of the non-wired single cylinder flow for $Re = 100$. From the table it is seen that the result of present simulation is consistent with the results from literature.

## 2.4 Experimental system and techniques

The experimental study involves the application of two different experimental techniques to different flow configurations. Both the electrolytic tin-precipitation method and Particle Image Velocimetry (PIV) are used for qualitative and quantitative evaluation of the flow behind the non-wired cylinder, the wired cylinder and the rotating cylinder.

### 2.4.1 Flow system and set-up

**Towing tank**

The experiments are performed in a towing tank with dimensions of $L \times W \times H = 500\,\text{cm} \times 50\,\text{cm} \times 75\,\text{cm}$ as shown in Figure 2.3 [42, 43]. The towing tank walls made of $15\,\text{mm}$ thick single piece glass which provides optical accessibility from all directions. The bottom and the side walls are insulated using foam to prevent heat transfer and hence convective motions in the tank.
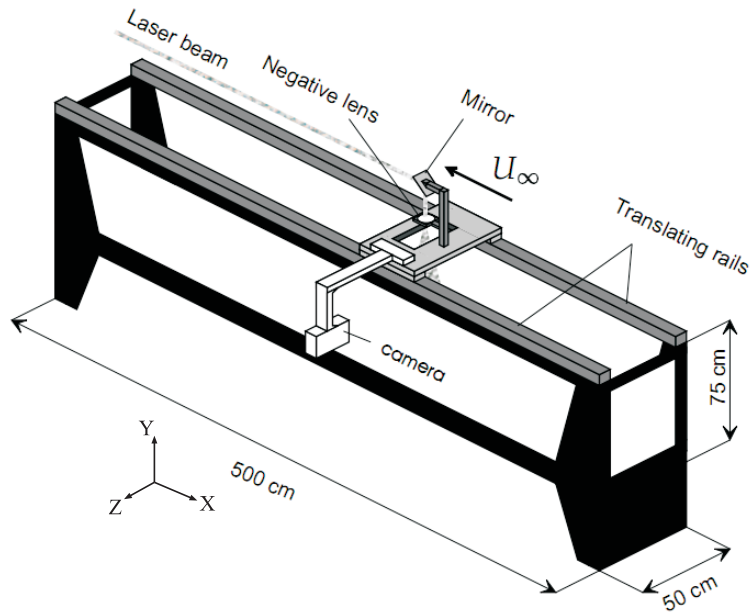
**Figure 2.3:** *Sketch of the towing tank used for experiments. (Figure is reproduced from Ren [43].)*

The test model is mounted on a moving carriage system which is placed on the top of the side walls. The carriage is pulled along the guiding rails by an electric motor. The speed of the carriage is controlled by setting the rotational speed of the electric motor. This towing system has the capability of reaching a maximum forward speed of $20\,\mathrm{mm\,s^{-1}}$.

The speed of the carriage corresponds to the free-stream velocity $U_\infty$ in the cylinder coordinate system. The water temperature is measured before every experiment to accurately calculate the kinematic viscosity value. This kinematic viscosity value, along with the desired Reynolds number, is used to calculate the corresponding free-stream velocity. The experiments were conducted at flow velocities ranging from $6\,\mathrm{mm\,s^{-1}}$ to $16\,\mathrm{mm\,s^{-1}}$, corresponding to Reynolds numbers of 100 to 250 based on the diameter of the cylinder.

**Experimental models**

A cylinder with diameter $D = 15\,\mathrm{mm}$ is used for the non-wired and wired experiments. The cylinder diameter is chosen considering the speed range of the towing system and Reynolds number range of the transition regime. The wire used in the experiments has a diameter of $d = 0.15\,\mathrm{mm}$, corresponding to a diameter ratio of $D/d = 100$.
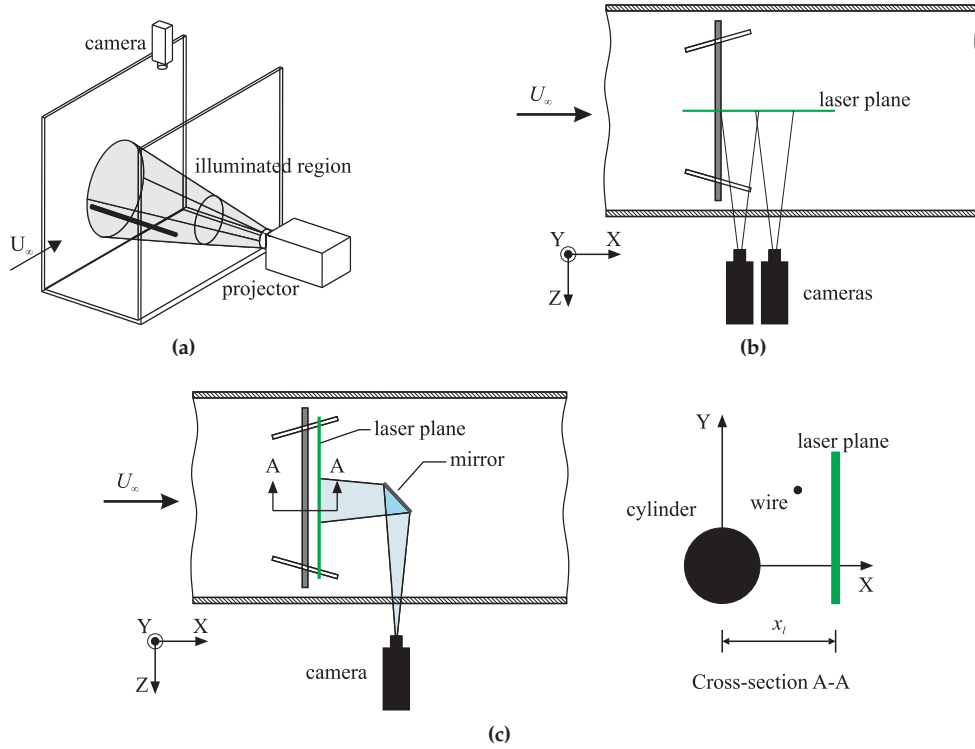
**Figure 2**.4: *Measurement configurations. (a) Three-dimensional flow visualization configuration, (b) Side-view configuration, (c) Back-view configuration.*

The cylinder is mounted parallel to the bottom and perpendicular to the side walls. Two circular perspex end plates with a diameter of $180\,\text{mm}$ are attached to the end of the cylinder. The end plates are rotated towards the middle of the tank with an angle of $18°$ with respect to the free-stream direction to ensure parallel shedding of the primary von Kármán vortices. The length of the cylinder is $L = 450\,\text{mm}$. However due to the inward rotated end plates the length of the middle section of the cylinder, which faces the free-stream directly, is $L = 320\,\text{mm}$. This corresponds to an aspect ratio of $L/D = 21.3$. The cylinder is placed in the middle of the water level so that top and bottom surface effects are negligible. The distance from the cylinder center to the top free surface and bottom wall equals $20\,\text{D}$.

**Measurement configurations**

Figure 2.4 shows the three different measurement configurations which are used throughout the experiments. The first configuration is used for the three-dimensional

flow visualization experiments, see Figure 2.4a. The flow field behind the cylinder is illuminated using a slide projector. A camera is placed at the top of the set-up for recording the images.

Figure 2.4b illustrates the second configuration, which is used for the investigation of the evolution of the primary, i.e. spanwise, vortices. This configuration is used for both flow visualization experiments and PIV measurements. The flow field is illuminated by a vertical laser sheet in the $XY - plane$ with a thickness of $3\,mm$. In the PIV experiments, the images are recorded synchronously with two side-by-side cameras to cover a larger field-of-view. The data obtained from the two-camera configuration is combined in the post-processing stage.

The third configuration is used for the investigation of the evolution of the secondary, i.e. streamwise, vortices. The layout of this configuration is shown in Figure 2.4c. The laser plane is located in the $YZ - plane$ with a thickness of $3\,mm$. The images are recorded through a mirror placed in the downstream of the wake. The size of the mirror is $100\,mm \times 100\,mm$ and is placed at an angle of $45°$ with respect to the free-stream direction. The effect of the mirror on vortex shedding is evaluated using top-view flow visualization experiments as shown in Figure 2.5. At the mirror position of $x_m = 10D$, parallel shedding of von Kármán vortices could not be achieved, as indicated with an arrow in Figure 2.5a. On the other hand, when the mirror center is located $x_m = 16D$ downstream of the cylinder, a clear parallel shedding is seen for both low, $Re = 100$, and high, $Re = 215$, Reynolds number flows as shown in Figure 2.5b and 2.5c, respectively. At this position, the generation of secondary vortices is not affected by the mirror.

## 2.4.2   Electrolytic tin-precipitation method

Flow visualization is a powerful technique to locate flow structures and analyze them qualitatively. For this purpose an electrolytic tin-precipitation method is used [49]. The method is previously used in visualizations of flow structures behind heated cylinders [26, 43]. The implementation of the method is straightforward and illustrated in Figure 2.6.

The technique is implemented by covering the surface of the cylinder with a tin foil of thickness $0.07\,mm$. The tin foil is connected to the positive pole (anode) of a power supply. A conducting plate is connected to the negative pole and acts as a cathode. In the present experiments, the cathode is a copper plate positioned at the downstream side of the towing tank where it does not effect the flow.

When a voltage difference is applied, the following electrolysis reaction occurs resulting in production of white tin(II)-hydroxide particles.

$$
\begin{aligned}
Sn(solid) - 2e^- &\longrightarrow Sn^{2+} \\
Sn^{2+} + 2OH^- &\longrightarrow Sn(OH)_2(solid)
\end{aligned}
\tag{2.8}
$$

**(a)** $Re = 100, x_m/D = 10$     **(b)** $Re = 100, x_m/D = 16$     **(c)** $Re = 215, x_m/D = 16$
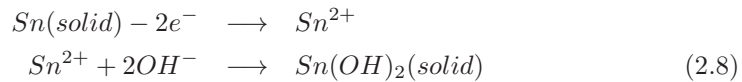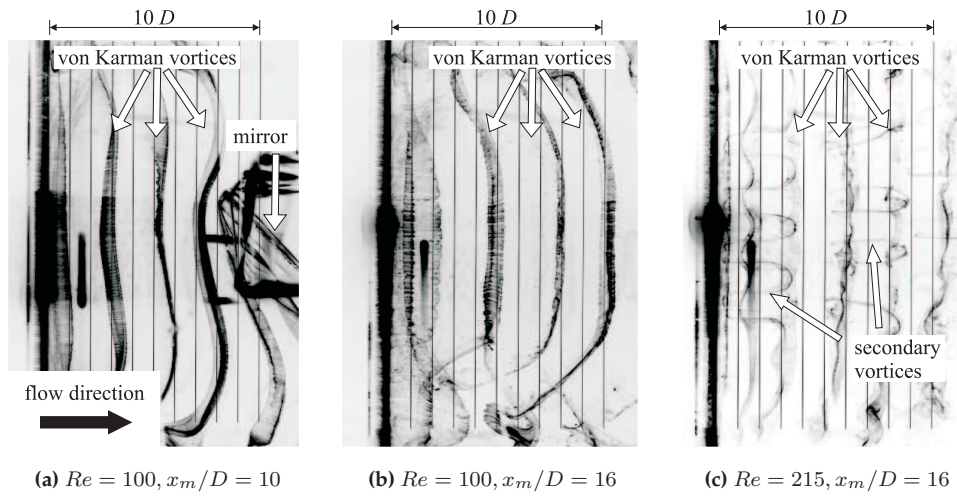
**Figure 2.5:** *Top-view flow visualization experiments to test the effect of the presence of the mirror on the near-wake structures behind the cylinder.*
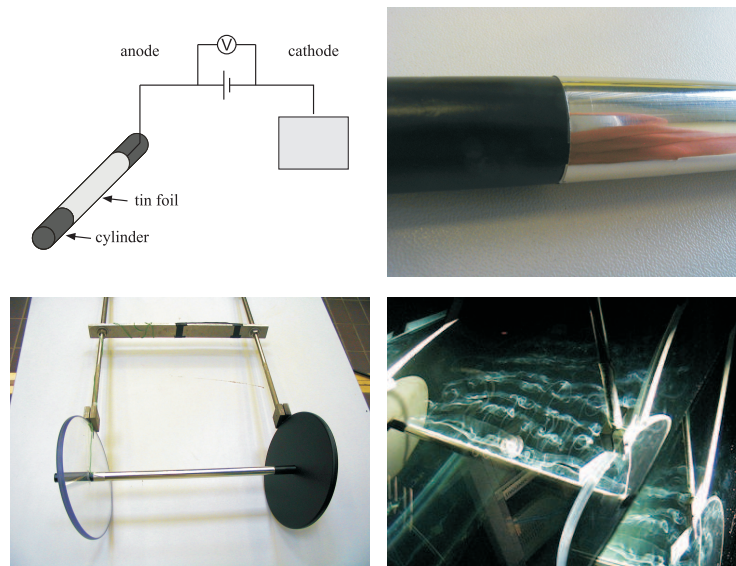


**Figure 2.6:** *Experiment model and technique of electrolytic-tin-precipitation method.*
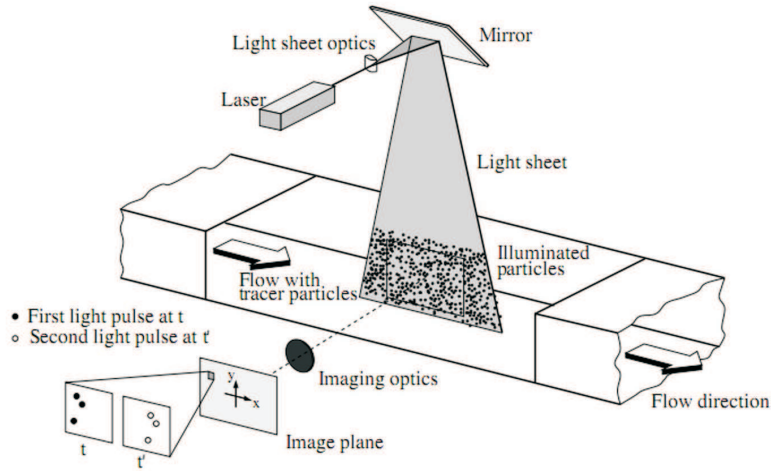
**Figure 2.7:** *Configuration of a typical Particle Image Velocimetry experiment. (Figure is reproduced from Raffel et al. [52])*

The production of particles is directly proportional to the applied voltage and the conductivity of the water. Depending on the free-stream velocity, a voltage difference of $12\,V$ to $15\,V$ is applied during the experiments. To enhance the amount of particles, the conductivity of the water is increased by adding approximately $250\,g$ of table salt to $2\,m^3$ water. The tin(II)-hydroxide particles have a diameter of $\mathcal{O}(1\,\mu m)$ and are not dissolvable in pH-neutral water. Since they are emitted from the surface of the cylinder directly into the boundary layer, the method becomes very useful as a non-intrusive technique to visualize the vortical structures in the wake.

### 2.4.3  Particle Image Velocimetry

Particle Image Velocimetry (PIV) method is used for the quantitative evaluation of the flow field. In this method the instantaneous velocity distribution is measured by evaluating the motion of tracer particles present in the flow [50–52]. Among several methods of PIV, the two-dimensional two-component PIV (2D-2C PIV) method is used in this research. A brief overview of the PIV technique is given below.

**Overview**

A typical PIV configuration is presented in Figure 2.7 where the major components of such a configuration are shown. PIV measures the local flow velocity indirectly using tracer particles added to the fluid. These particles need to be small enough to move with the local fluid flow velocity and big enough to reflect enough light for an accurate recording. The tracer particles are illuminated twice using two laser pulses

| Measurement plane | $XY-plane$ | $YZ-plane\,(x_l/D=4)$ |
|---|---|---|
| Freestream velocity | $U_\infty = 11.2\,\mathrm{mm\,s^{-1}}$ | $U_\infty = 12\,\mathrm{mm\,s^{-1}}$ |
| Kinematic viscosity | $\nu = 0.9333\,\mathrm{mm^2\,s^{-1}}$ | $\nu = 1.0047\,\mathrm{mm^2\,s^{-1}}$ |
| Number of cameras | 2 (side-by-side) | 1 |
| Magnification | $M = 14.53\,\mathrm{px/mm}$ | $M = 15.49\,\mathrm{px/mm}$ |
| Field of view (single camera) | $S_x = 110.12\,\mathrm{mm}$ | $S_y = 77.47\,\mathrm{mm}$ |
| | $S_y = 82.59\,\mathrm{mm}$ | $S_z = 103.29\,\mathrm{mm}$ |
| Field of view (after merging) | $S_x = 211.29\,\mathrm{mm}$ | - |
| | $S_y = 82.59\,\mathrm{mm}$ | - |
| Lens focal length | $f = 50\,\mathrm{mm}$ | $f = 50\,\mathrm{mm}$ |
| Lens aperture | $f_\# = 2.8$ | $f_\# = 2.8$ |
| Exposure time | $t_{exposure} = 25\,\mathrm{ms}$ | $t_{exposure} = 25\,\mathrm{ms}$ |
| Pulse delay | $\Delta t = 1/15\,\mathrm{s}$ | $\Delta t = 1/15\,\mathrm{s}$ |
| Number data files | $N_f = 3500$ | $N_f = 2700$ |

**Table 2.5:** *Summary of PIV experiment details for side-view ($XY-plane$) and back-view ($YZ-plane$) wired cylinder measurements. [Re=180]*

with a time delay of $\Delta t$ in between. The images of the particles are recorded using a high-resolution digital camera.

The local velocity vectors are derived by applying special correlation algorithms to the recorded image frames. The evaluation of the PIV images is carried out by dividing them into smaller sub-domains called 'interrogation windows'. Applying image cross-correlation for each interrogation window gives the local displacement vector $\Delta x$ over time $\Delta t$ for the each corresponding interrogation window, assuming that all the tracer particles in one interrogation window have moved homogeneously between the two laser pulses. Afterwards, the calculation of the local measured velocity is rather straightforward using Equation 2.9.

$$\boldsymbol{u} = \frac{\Delta \boldsymbol{x}}{\Delta t} \tag{2.9}$$

Further details about the PIV method can be found in Adrian [50], Westerweel [51], Raffel et al. [52].

**Image acquisition**

Prior to the experiments, $20\,\mathrm{\mu m}$ diameter Polyamid Seeding Particles (PSP) are added into the water of the towing tank. The seeded flow is illuminated using a single pulsed $200\,\mathrm{mJ}$, $532\,\mathrm{nm}$ Nd-YAG laser. The time between the two laser pulses is fixed to $1/30\,\mathrm{s}$. The TTL signal of the laser is used to trigger the camera system.

Instantaneous flow field images are captured using an image acquisition system which includes two 12-bit MegaPlus ES 2020 cameras, a Redlake Megaplus II Ca-

| Measurement plane | $XY - plane$ | $YZ - plane\ (x_l/D = 4)$ |
|---|---|---|
| Image resolution | $1600\,\mathrm{px} \times 1200\,\mathrm{px}$ | $1600\,\mathrm{px} \times 1200\,\mathrm{px}$ |
| Interrogation window size | $32\,\mathrm{px} \times 32\,\mathrm{px}$ | $32\,\mathrm{px} \times 32\,\mathrm{px}$ |
| Overlap | $50\%$ | $50\%$ |
| Number of vectors(per frame) | $N_x = 98, N_y = 73$ | $N_y = 73, N_z = 98$ |
| | $N_{total} = 7154$ | $N_{total} = 7154$ |
| Spatial resolution | $d_s = 1.10\,\mathrm{mm}$ | $d_s = 1.03\,\mathrm{mm}$ |
| | $d_s = 0.0733\,\mathrm{D}$ | $d_s = 0.0689\,\mathrm{D}$ |
| Replaced vectors | $\approx 0.5\%$ | $\approx 0.5\%$ |

**Table 2.6:** *Summary of PIV data processing parameters for spanwise (XY-plane) and streamwise (YZ-plane) wired cylinder measurements. [Re=180]*

mera Control Console and a computer with NI-PCIe-1430 data acquisition card. The camera has an interline, progressive scan CCD chip with an active area of $11.8\,\mathrm{mm} \times 8.9\,\mathrm{mm}$ and a resolution of $1600\,\mathrm{px} \times 1200\,\mathrm{px}$, which corresponds to a pixel size of $7.4\,\mathrm{\mu m} \times 7.4\,\mathrm{\mu m}$. It has the capability of recording images with $30\,\mathrm{frames/s}$ (fps). However, due to the large data flow in combination with computer recording limitations, the data acquisition rate is limited to $15\,\mathrm{Hz}$ during PIV experiments.

A summary of the experimental details for two types of experiments is given in Table 2.5. As one can notice the camera field of view in both side-view and back-view experiments is close to each other and corresponds to approximately $(S_x, S_y) \approx (7.3D, 5.5D)$ and $(S_y, S_z) \approx (5.2D, 6.9D)$ in terms of cylinder diameters, respectively. However, in the side-view experiments two cameras in side-by-side arrangement is used to cover a larger field of view which resulted in field of view of approximately $(S_x, S_y) \approx (14.1D, 5.5D)$. The remaining recording parameters are the same in both of the experiment types.

**Image processing**

The processing of the images is done using PIVview 3.0 (© PIVTEC GmbH) software. The images of each camera are processed separately using the same method and parameters. A summary of the PIV processing parameters for two different type of experiments is presented in Table 2.6. As one can notice, the major difference between the two types of experiments is the spatial resolution due to different magnification factors. A snapshot of a superposed image pair before image processing is shown in Figure 2.8a.

The images are processed using a multi-grid (grid refinement) algorithm. This method uses a pyramid approach starting with larger interrogation windows on a coarse grid and refining the interrogation windows and grid on each pass. In each pass a cross-correlation with least squares Gaussian sub-pixel peak fitting is performed. Outlier detection is used for filtering the intermediate vector fields. In
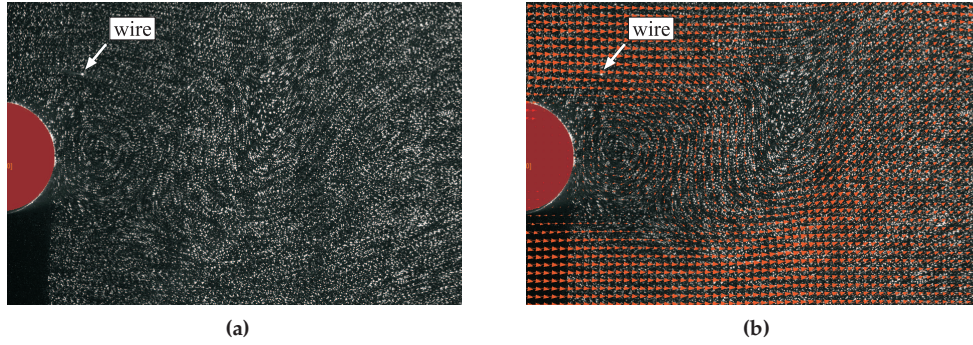
**Figure 2**.8: *An example of image processing procedure; (a) Superposition of two consecutive images, (b) Corresponding vector field of these images. [Re = 180]*

the present experiments, the initial and final interrogation window sizes are set to $96\,\text{px} \times 96\,\text{px}$ and $32\,\text{px} \times 32\,\text{px}$ with $50\%$ overlap in each direction, respectively. This final grid resolution corresponds to a vector field of size $N_x \times N_y = 98 \times 73$ vectors.

Sub-pixel image shifting is enabled in all passes of the multi-grid algorithm. This technique uses a second order method to deform the image data using the displacements values of the previous interrogation passes. In the present work, $3^{rd}$-order B-splines are used for sub-pixel image shifting.

The resulting velocity vectors from the interrogation process are validated using a normalized median test with a threshold value of $2$ [53]. The detected so-called bad vectors are then replaced by using first low order peaks in the correlation plane, second interpolation and third re-evaluation with larger window size. The second and third methods are used only if the previous one did not fulfill the validation criteria. Finally, Gaussian weighted smoothing operation is carried out to remove the possible experimental noise from the resulting data field. The corresponding vector field of the image pair in Figure 2.8a is shown in Figure 2.8b.

**Merging of two vector fields**

As stated above, during the side-view (XY-plane) PIV measurements two image frames are recorded synchronously. After separate processing of the data, the obtained vector fields are merged in the post-processing stage to get a larger vector field. A sample merging procedure is demonstrated in Figure 2.9 showing an instantaneous spanwise vorticity field for a wired case experiment at $Re = 180$. The overlapping region between the two frames is $6$ data points ($\approx 130\,\text{px}$) long in the $x$-direction. Hence, the final merged data field has a size of $N_x \times N_y = 190 \times 73$ data points. The figure represents a challenging example where a vortex is present in the overlapping region. Part of the vortex is measured by two cameras and the velocity
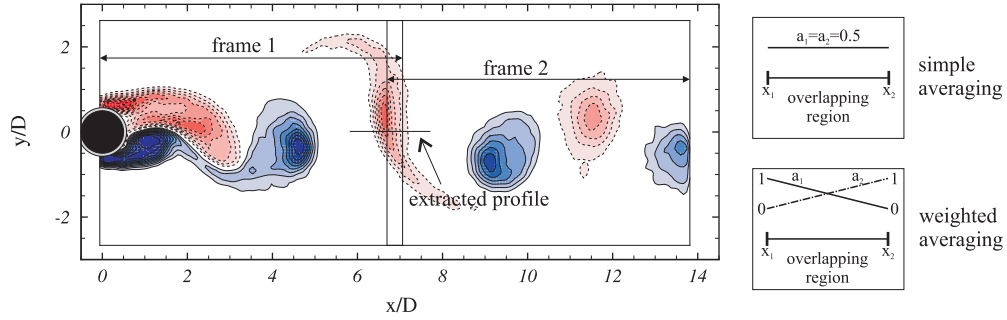
**Figure 2**.9: *Instantaneous spanwise vorticity contours after merging, [Re = 180]. Two different frames are labeled as frame 1 and frame 2 and indicated with arrows. To assess the averaging methods which are given on the right hand side velocity and vorticity data is extracted along the indicated line.*

field needs to be continuous through the frame boundaries.

The merging approach of two independently measured vector fields is similar to the one used in Herpin et al. [54] where they have used a simple averaging in the overlapping region. In their method it is assumed that a flow variable $\varphi$ in the overlapping region can be simply calculated by taking a linear combination of the data from frame 1 and frame 2 as follows.

$$\varphi = a_1 \varphi_1 + a_2 \varphi_2 \tag{2.10}$$

with $a_1$ and $a_2$ being the corresponding weighting coefficients. To find the optimum averaging method two methods are tested; simple averaging and weighted averaging. The results are assessed by plotting the extracted spanwise vorticity and velocity profiles on the wake centerline which is indicated in Figure 2.9 as 'extracted profile'.

In the first method, the weighting coefficients are assumed to be equal and constant, $a_1 = a_2 = 0.5$. These coefficients correspond to a simple averaging operation and the result is presented in Figure 2.10. It is clear from the figure that close to the frame boundaries, deviations are present in the merged vorticity and velocity profiles. This deviation is much more severe in the vorticity profile than in the velocity profiles. The major cause of the deviation is the effect of image boundaries on PIV interrogation and data calculations.

To minimize these boundary effects, a linear weighted averaging method is used. The weighting coefficients $a_1$ and $a_2$ are taken as linear functions of the horizontal

**Figure 2**.**10:** *Extracted spanwise vorticity, horizontal and vertical velocity profiles after simple averaging in the overlapping region. Each symbol in the figures corresponds to a PIV grid point.*

distance within the overlapping region, as shown in Figure 2.9 and formulated as

$$a_1 = \frac{-x}{x_2 - x_1} + \frac{x_2}{x_2 - x_1}$$
$$a_2 = 1 - a_1 \tag{2.11}$$

The results of the merging are presented in Figure 2.11 which clearly shows that the boundary effects are minimized in the merged profiles.

**Vortex identification**

Vortices are defined using the $\lambda_2$-method. The variable $\lambda_2$ is

$$\lambda_2 = \left( \frac{\partial u}{\partial x} + \frac{\partial v}{\partial y} \right)^2 - 4 \left( \frac{\partial u}{\partial x} \frac{\partial v}{\partial y} - \frac{\partial u}{\partial y} \frac{\partial v}{\partial x} \right), \tag{2.12}$$

which is the discriminant of the non-real eigenvalues of the velocity gradient tensor.

It has been shown that regions with negative values of $\lambda_2$ indicate the presence of vortical structures, see Jeong and Hussain [55], Vollmers [56]. Therefore, a vortex can be defined as a region that is bounded with a closed $\lambda_2$ contour line. Although the numerical value that defines the contour level is free to choose, in this analysis the value is set to be $-0.1$. So, any closed contour region where $\lambda_2 \leq -0.1$ is defined as a vortex. Figure 2.12 shows the comparison of a PIV experiment and a SEM calculation for the $Re = 100$ wired case. The contour plots indicate non-dimensional spanwise vorticity and solid lines indicate $\lambda_2 = -0.1$ contours. There is a clear similarity between the measurement and the simulation.

Once the vortex is defined, the calculation of its strength and location is straight-
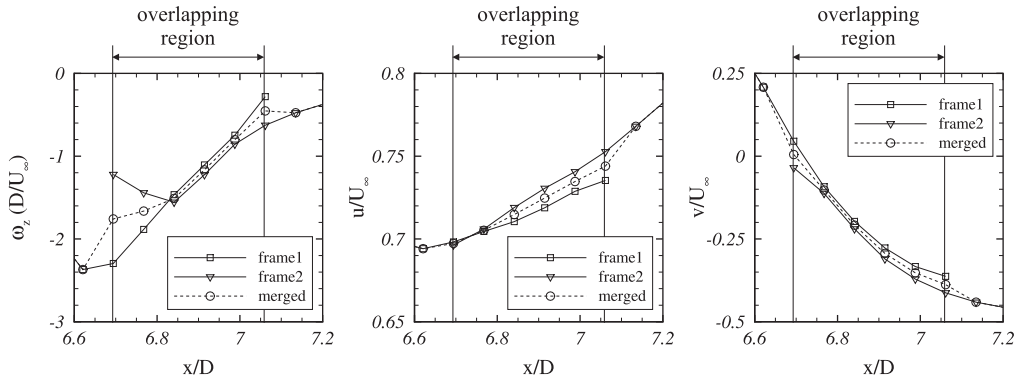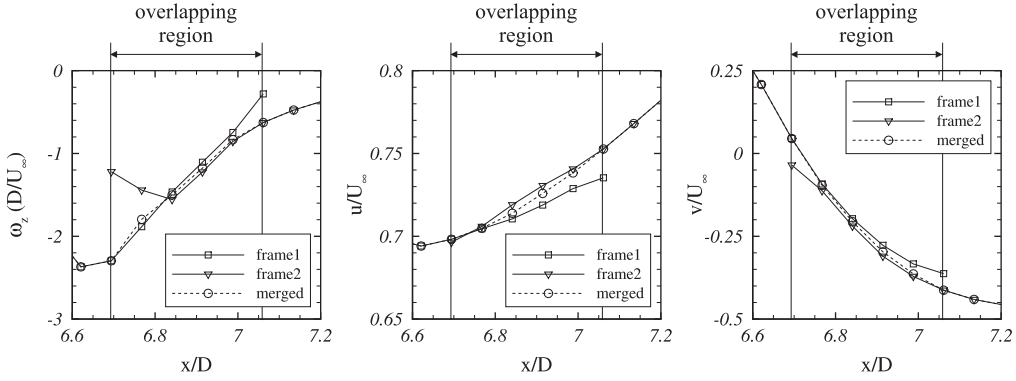
**Figure 2**.11: *Extracted spanwise vorticity, horizontal and vertical velocity profiles after weighted averaging in the overlapping region. Each symbol in the figures corresponds to a PIV grid point.*

forward. The circulation, i.e. strength, of a vortex is given by the area integral:

$$\Gamma = \int_A \omega_z \, \mathrm{d}A \tag{2.13}$$

where the area $A$ is encircled by the constant $\lambda_2$ contour line. An unstructured triangular grid within a vortex area is used to perform the numerical integration. The position of a vortex is determined by the location of its center, the coordinates of which are calculated as:

$$x_c \;=\; \frac{1}{\Gamma} \int_A \omega_z x \, \mathrm{d}A \tag{2.14}$$

$$y_c \;=\; \frac{1}{\Gamma} \int_A \omega_z y \, \mathrm{d}A \tag{2.15}$$

Trajectories are extracted by tracking the vortex centers after formation. Each trajectory was plotted by tracking one single vortex from formation until its exit of the calculation domain. Two vortices were tracked individually for each case, i.e. one from the upper row and one from the lower row. The wake orientation was then calculated by taking the mean of upper and lower vortex trajectories.

**Experimental uncertainty**

A first estimation of the uncertainty is performed according to Raffel et al. [52]. They have provided possible error sources of PIV experiments and approximate order of magnitude of errors. Based on their analysis, the random measurement uncertainty in PIV analysis is found to be $\sigma_{rms} \approx 2.23\%$ for $XY - plane$ experiments and $\sigma_{rms} \approx 4.94\%$ for $YZ - plane$ experiments.
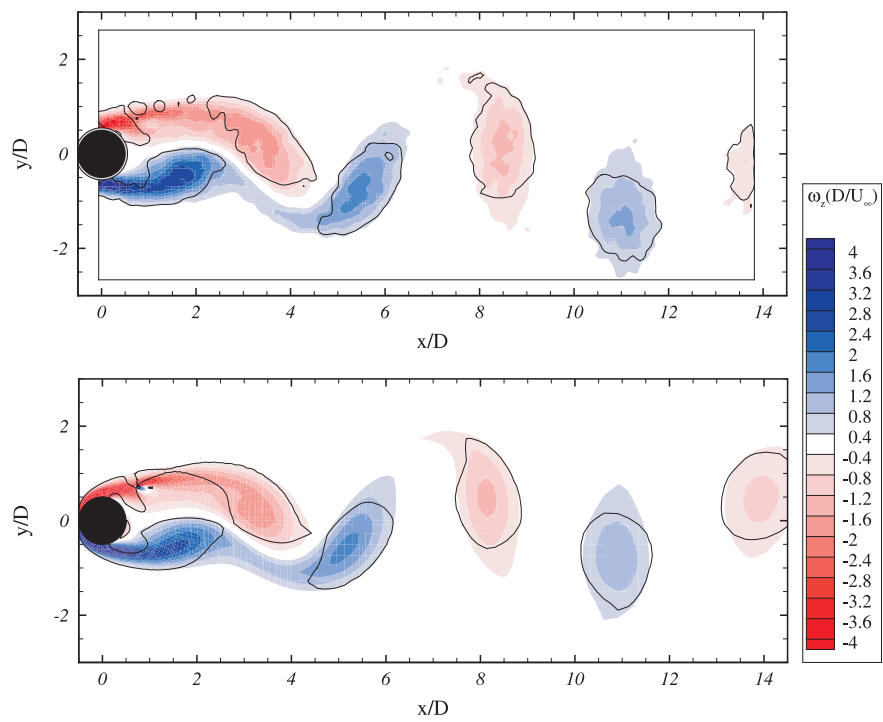
**Figure 2**.**12:** *Definition of a vortex using $\lambda_2$-method. Upper and lower figures show PIV measurement and SEM calculation, respectively. Solid lines represent the contour line of $\lambda_2 = -0.1$. [$Re = 100$]*
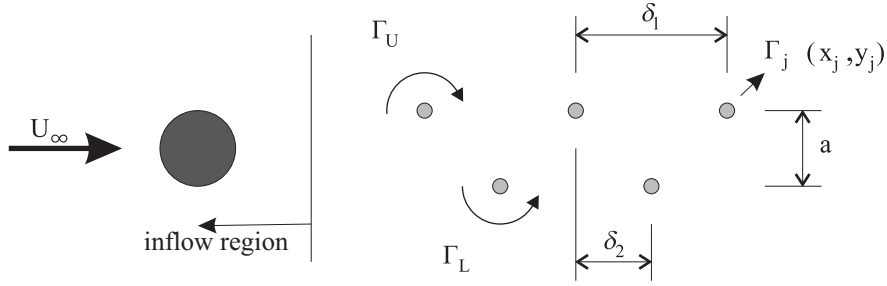
**Figure 2**.**13:** *Point vortex model used for the analysis of the wake behind the inflow region.*

A second approach for calculating the random error is given by Herpin et al. [54] for the merged velocity fields. During the merging procedure the root-mean-square (rms) values of the differences between the two velocity fields in the overlapping region are calculated. These rms values can be thought of as a random error or measurement uncertainty of two independent experiments. Based on their approach, the rms value is calculated as $(u_{frame1} - u_{frame2})_{rms} \approx 0.95\%U_\infty$ for the horizontal velocity component and $(v_{frame1} - v_{frame2})_{rms} \approx 1.22\%U_\infty$ for the vertical component in side-view (XY-plane) measurements. These values are on the same order of magnitude with the uncertainity values of Herpin et al. [54].

## 2.5   Point Vortex Model

The interaction of different vortices in the circular cylinder wake determines the behavior of the wake as a whole. A simple approach to model these interactions is the Point Vortex Model. The vortex arrangement and configuration of the Point Vortex Model is shown in Figure 2.13. In this model, every single vortex located at $(x_j, y_j)$ in the wake is assumed to be a point vortex with strength $\Gamma_j$. The vortices are assumed to be away from the formation region. The velocity of a point vortex at the location $(x_j, y_j)$ is equal to the summation of velocities induced by other vortices [57]. This formulation under a constant horizontal free-stream velocity $U_\infty$ takes the form:

$$u_j = U_\infty - \frac{1}{2\pi} \sum_{i(\neq j)} \frac{\Gamma_j(y_j - y_i)}{(x_i - x_j)^2 + (y_i - y_j)^2} \tag{2.16}$$

$$v_j = \frac{1}{2\pi} \sum_{i(\neq j)} \frac{\Gamma_j(x_j - x_i)}{(x_i - x_j)^2 + (y_i - y_j)^2} \tag{2.17}$$

The derivation of the Point Vortex equations is made under the assumption of infinitely long vortex rows. Due to the finite size of the calculation domain in this research, the vortex rows are of finite length. This situation creates fluctuations in

the trajectories at both ends of the calculation domain. In order to overcome this problem, an inflow region is defined. This region has a constant number of vortices which are positioned according to the stability criterion of von Kármán , $a/\delta_1 = 0.281$. The vortices in the inflow region are allowed to move only in the $x - direction$ with the velocity of $u = U_\infty - \Gamma/(\delta_1\sqrt{8})$. As soon as a vortex leaves the inflow region all the restrictions on its position and motion are removed.

The relative position of vortices with respect to each other is determined by the spacing ratio of $\delta_1/\delta_2$. The ratio $\delta_1/\delta_2$ for a specific upper vortex is defined as the distance to the previously shed upper vortex divided by the distance to the previously shed lower vortex, see Figure 2.13.

# Vortex dynamics in a wire-disturbed cylinder wake for $Re = 100$*

## 3.1 Introduction

Parallel to the studies of single cylinder flow, many researchers have conducted flow control studies with the aim of suppressing vortex shedding. The most recent review on flow control studies can be found in Choi et al. [58]. One of the methods for vortex shedding suppression is using an external control cylinder in the near-wake. Most of the studies of this wake control method consist of the investigation physical mechanisms of wake interaction between the cylinder and a control cylinder.

Strykowski and Sreenivasan [59] studied the mechanism of flow suppression by using an external control cylinder for low Reynolds numbers in the laminar, two-dimensional periodic flow regime. They performed experiments at different Reynolds numbers with different sizes and positions of the control cylinder. They discussed that for small Reynolds numbers there exists a region in which the control wire can be placed, which leads to maximum effectiveness in damping and vortex shedding suppression. This region is in the near-wake of the cylinder, outside the maximum vorticity line of the steady wake and its shape depends on the Reynolds number of the main cylinder flow and the diameter ratio. Although, they did not achieve a suppression for $Re > 80$, they obtained considerable reduction of the

---

*This chapter is adapted from: I. Yildirim, C.C.M. Rindt, A.A. van Steenhoven. Vortex dynamics in a wire-disturbed cylinder wake. *Physics of Fluids*, 22:094101, 2010.

shedding frequency. They concluded their experiments with an explanation of the suppression mechanism using the approach of interacting shear layers as introduced by Gerrard [6]. By placing the control cylinder in the near-wake the concentrated vorticity diffuses such that the attraction force between the opposing shear layers decreases. This reduction results in a lower shedding frequency. The configuration at low Reynolds numbers was further studied by Mittal and Raghuvanshi [48], Dipankar et al. [60], Kuo et al. [61], Marquet et al. [62].

Several studies concentrated on the control and analysis of high Reynolds number flows. Sakamoto and Haniu [63] performed wind tunnel experiments at Reynolds number of $65000$ and diameter ratio of approximately $18$. Their study concentrated on the effect of the control cylinder on fluid forces and shedding frequencies by placing the control cylinder very close to the main cylinder. Dalton et al. [64] used flow visualization studies in addition to numerical simulations to study the suppression of vortex shedding at moderate Reynolds numbers. They noted that the minimum values for drag and lift coefficients depend on the gap ratio between the two cylinders and the angle of attack of the main flow.

The afore mentioned studies on the effect of a control cylinder all focus on the near-wake dynamics like vortex formation mechanisms, drag and shedding characteristics. However, little attention has been paid to the dynamics and properties of the shed vortices in the far-wake. Ahlborn et al. [65] used empirical methods to derive relations between the drag, shedding frequency and some properties of the wake of a single cylinder. However, their study did not include any discussion about the wake trajectories. The behavior of the wake trajectories in the heated cylinder case was studied by Kieft et al. [41, 66] by means of Particle Tracking Velocimetry and SEM simulations. The observed downwards deflection of the wake was explained using the Point Vortex Model.

Our initial flow visualization experiments showed that the presence of a wire modifies the vortex trajectories in the laminar, two-dimensional periodic flow regime. Sample images from these preliminary experiments are shown in Figure 3.1 where a downwards tendency of the wake axis for the $x_w/D = 0.75$ case and an upwards tendency for the $x_w/D = 1.0$ case are observed. The top-figure shows the visualization result for the non-wired case. A regular staggered pattern of the shed vortices is observed. For $y_w/D = 0.75$ case, the upper vortex row is shifted downwards. This also seems to hold for the lower vortex row although to a lesser extent. For $y_w/D = 1.0$ case, the whole vortex street seems to show a widening where the upper vortices are shifted upwards and the lower vortices downwards. Because the upward motion appears to be larger than the downwards one, the wake axis moves up. Therefore, the present chapter mainly focuses on the wake deflection phenomenon of the wire disturbed cylinder wake.

The flow assessment has been performed at Reynolds number of $Re = 100$ as function of various wire positions using SEM simulations, as summarized in Table
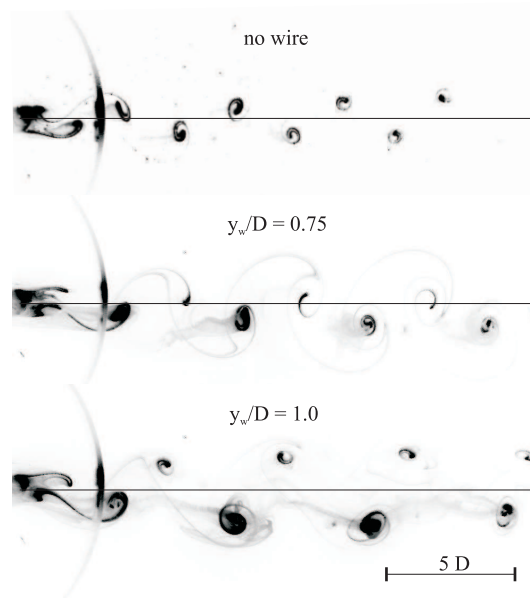
**Figure 3.1:** *Flow visualization images of wire disturbed circular cylinder wake.* [$Re = 100$, $x_w/D = 0.75$]

2.3 in Chapter 2. Firstly, the effect of the wire on the temporal characteristics, such as fluctuating velocity and vortex shedding frequency, are investigated. Secondly, the effect of the wire on the wake behavior is presented by comparing the downstream variation of vortex trajectories, wake centerlines and vortex strengths at different wire positions. A Point Vortex Model is used to understand the relationship between the wake trajectories and vortex properties. Thirdly, the assessment of the vortex strengths and wake deflection is performed. Investigating vorticity flux properties in combination with vortex shedding frequencies provides information about sources of strength differences. Finally, the possible correlation between the wake deflection and lift-drag characteristics of the main cylinder is investigated.

## 3.2 Temporal characteristics of the wake

### 3.2.1 Time-averaged streamwise velocity fluctuations

The time averaged streamwise velocity fluctuations $u_{rms}$ for various wired and non-wired cases at $Re = 100$ are shown in Figure 3.2. The results are obtained from two-dimensional SEM simulations which are summarized in Chapter 2. In Figure 3.2, the "no wire" case represents the single cylinder flow without the effect of the
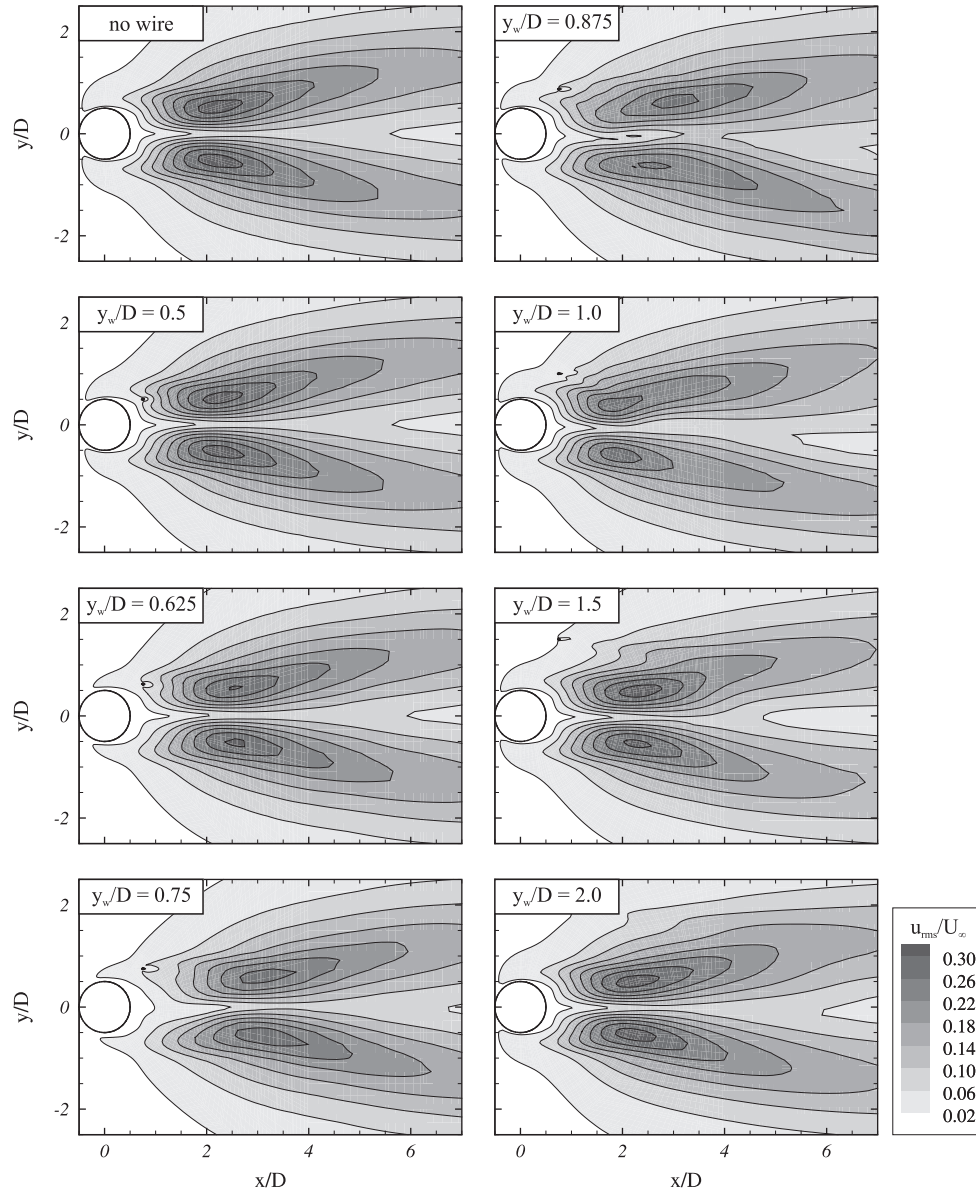
**Figure 3**.**2:** *Time-averaged streamwise velocity fluctuations, $u_{rms}$, contours obtained from SEM simulations. [Re = 100, $x_w/D = 0.75$].*
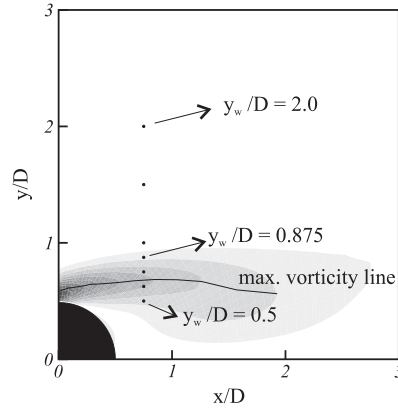
**Figure 3**.3: *Positions of the wire in the time mean vorticity field of the non-wired cylinder flow. The contours represent the mean vorticity in the upper shear layer, while the solid line is the maximum vorticity line, i.e. centerline for the upper shear layer. [$Re = 100$, $x_w/D = 0.75$].*

wire in the near-wake. Detailed observation of Figure 3.2 reveals that placing a wire at one side of the cylinder has two consequences for the $u_{rms}$ results; the change of the fluctuation levels and the change of symmetry of the contours.

For the wire locations of $y_w/D = 0.75, 0.875$ and $1.0$, the differences from the reference non-wired case are clearly noticeable. It is evident from the contour levels for the cases $y_w/D = 0.75, 0.875$ and $1.0$ that the level of horizontal velocity fluctuations is reduced. These observations are quantified by probing the maximum values of the time averaged horizontal velocity fluctuations in the wake for each case, see Table 3.1. The negative values for the difference indicate a reduction of velocity fluctuations. The velocity fluctuation levels are reduced in all cases. However, for the cases $y_w/D = 0.75, 0.875$ and $1.0$, the damping is larger than $10\%$ with $y_w/D = 0.875$ having a maximum of $15.29\%$. For the rest of the wire positions the damping is on the order of a few percent. All the three wire positions with high damping values are above the maximum vorticity line of the non-wired cylinder wake as shown in Figure 3.3, where the wire positions are superposed with the time mean vorticity field of the non-wired cylinder wake. It is likely that the wire-induced vorticity is diffused in the upper shear layer of the main cylinder due to the interaction of the wire generated positive vorticity and cylinder generated negative vorticity for these three wire positions. The trend in the fluctuation difference with respect to the wire position in Table 3.1 indicates that there is an optimal position for the wire where the highest damping of the velocity fluctuations is achieved. This optimal position is $y_w/D = 0.875$ in the present study and above the maximum vorticity line, which is consistent with the conclusions of Strykowski and Sreenivasan [59].

Another effect of the wire is breaking the symmetry in the $u_{rms}$ contour plots. In

| Wire position | $u_{rms}\,|_{max}$ | Difference |
|---|---|---|
| no wire | 0.3205 | |
| $y_w/D = 0.5$ | 0.3174 | -0.97 % |
| $y_w/D = 0.625$ | 0.3046 | -4.96 % |
| $y_w/D = 0.75$ | 0.2844 | -11.26 % |
| $y_w/D = 0.875$ | 0.2715 | -15.29 % |
| $y_w/D = 1.0$ | 0.2826 | -11.83 % |
| $y_w/D = 1.5$ | 0.3181 | -0.75 % |
| $y_w/D = 2.0$ | 0.3182 | -0.75 % |

**Table 3**.**1:** *Maximum levels of velocity fluctuations $u_{rms}$ obtained from SEM simulations. The last column shows the difference with respect to the reference single cylinder case. The negative values indicate reduction in fluctuation levels.*

the reference non-wired case, the $u_{rms}$ contours are perfectly symmetric with respect to the wake center line $y/D = 0$. However, when Figure 3.2 is examined in detail, it can be seen that for all other cases the symmetry is broken. This effect of breaking the symmetry is most pronounced for the cases of $y_w/D = 0.875$ and 1.0. For the $y_w/D = 0.875$ situation, the fluctuation contours in the lower part of the wake are elongated and its maximum point is closer to the cylinder than the maximum point in the upper part. For the $y_w/D = 0.75$ case, the elongated contours are located in the upper part of the wake and the maximum points in the upper and lower parts are located nearly at the same downstream position. These asymmetries in the $u_{rms}$ fields suggest that there might be a difference in the formation process of the upper and lower vortices.

### 3.2.2   Shedding frequency

For further evaluation of the flow field, the vortex shedding frequencies are extracted from the horizontal velocity data $u$ which is obtained by data probing at the position $(x/D, y/D) = (2, 0)$ in the time dependent flow field. The non-dimensional shedding frequency of the vortices is represented by the Strouhal number which is defined as $St = f_{shed}D/U_\infty$. The values of the Strouhal numbers for different wire positions are presented in Figure 3.4. The Strouhal number for the non-wired case is calculated to be $St = 0.166$. This value is indicated as a dashed line in Figure 3.4. Placing the wire at a position of $y_w/D = 0.5$ does not change the shedding frequency. This is in line with the former results for the velocity fluctuations, where for this case a very small reduction was observed. The Strouhal number takes its minimum value when the wire is placed at the position of $y_w/D = 0.875$. This corresponds to a shedding frequency reduction of $9.64\%$ compared to the non-wired case. One can recall from Table 3.1 that this wire position is the one where maximum damping of the velocity fluctuations is found. From that position on, the shedding frequency rises again up
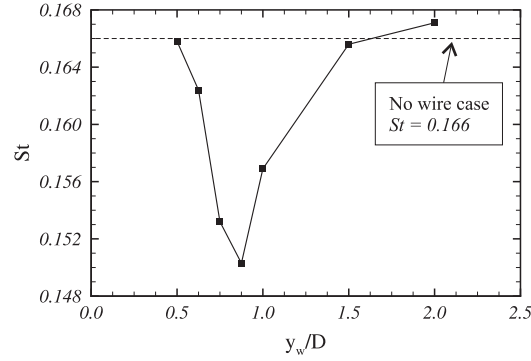
**Figure 3**.**4:** *Non-dimensional shedding frequency, St, as a function of the vertical position,* $y_w/D$. *[Re = 100, $x_w/D = 0.75$.]*

to the value for the non-wired case.

In order to determine the effect of the streamwise coordinate of the wire, also simulations were performed at the vertical position of $y_w/D = 0.875$, for which shedding frequency of the main cylinder was found to be most affected. It was found that the effect of the horizontal position has a minor effect on the shedding frequency when compared to the effect of the vertical position. In Strykowski and Sreenivasan [59], it was shown that the optimum position of the second cylinder for the wake control lies within boundaries of a closed elliptical region which is stretched in streamwise direction and this region shrinks to a very small area for high $D/d$ ratios at a certain Reynolds number. From their conclusions it can be understood that shedding frequency of the main cylinder is more sensitive to the vertical position of the control cylinder than for the horizontal position for a specific configuration. Therefore, the wake dynamics analysis is only performed and reported for the horizontal wire position of $x_w/D = 0.75$.

## 3.3   Analysis of wake behavior

The analysis of the wake behavior is performed by investigating the trajectories and strengths of vortices defined by constant $\lambda_2 = -0.1$ contour. As an example, the vorticity field, vortex boundaries and trajectories of the vortices for the wire positions of $y_w/D = 0.75, 1.0, 2.0$ are shown in Figure 3.5. The figure represents the instants at which the upper vortices are formed. The downward deflection of the wake is noticeable for $y_w/D = 0.75$ in Figure 3.5a. However, the tendency of the wake is upwards in Figures 3.5b and 3.5c in which the wire is positioned at $y_w/D = 1.0$ and $y_w/D = 2.0$, respectively. Moreover, the interaction of the wire-generated vorticity in the upper vortex formation area is seen in Figure 3.5a and 3.5b where the wire is

positioned in or close to the upper shear layer. For the $y_w/D = 2.0$ situation, the wire is clearly out of the shear layer and does not show any vortex shedding.

### 3.3.1   Vortex trajectories and strengths

In order to elucidate the effect of the wire on the cylinder wake behavior, it is necessary to look into the trajectories and strengths of the vortices for the simulated cases. The simulated cases are categorized into three groups according to the tendency of trajectories. In order to be remote of the formation dynamics region and the numerical influences of the outflow boundary, the trajectories are plotted for the domain $8 \leq x/D \leq 32$.

The results for the first group are presented in Figure 3.6. In the cases $y_w/D = 0.5$ and $0.625$, the vortices follow almost the same trajectories with a minor downwards deflections when compared to the single cylinder case. Figure 3.6a shows the vortex trajectories. The deflection is so low that it can be accepted as there is no wake deflection at all for the afore mentioned cases. This is also evident from Figure 3.6b where the wake centerlines are shown. The comparison of the vortex strengths also shows that there is no apparent strength difference between the considered cases and the reference no-wire case, see Figure 3.6c. After these observations one may conclude that placing the wire at the positions of $y_w/D = 0.5$ and $0.625$ do not bring any significant difference by means of vortex trajectories and vortex strengths. However, as stated in the previous section, the velocity fluctuations and the Strouhal numbers are reduced.

The second group contains the cases with wire position $y_w/D = 0.75$ and $0.875$ in which the wake tendency is downwards. The wake properties of these two cases are shown in Figure 3.7. Examining the trajectories in Figure 3.7a shows that there is a uniform downward shift of both upper and lower vortex trajectories for the $y_w/D = 0.75$ case. On the other hand, the trajectories for the $y_w/D = 0.875$ case are not as uniform as for the $y_w/D = 0.75$ case. Despite the downward tendencies of both wakes, it is seen that they show different behaviors when the wake centerline curves for both cases are compared. As shown in Figure 3.7b, the wake centerline shows a linear downward path for the $y_w/D = 0.75$ case. On the other hand, the upward tendency of the upper vortices for $x/D > 17$ in Figure 3.7a is because of the widening of the vortex street which is also seen in the no-wire case.

On the contrary, the wake for the $y_w/D = 0.875$ case shows different characteristics throughout the domain of interest. Firstly, the upper row shows higher upwards deflection for downstream positions of $x/D > 17$. Secondly, the lower vortices are constantly moving downwards with decreasing vertical velocity. This results in a convex trajectory. The combination of these two differences end in a parabola-like wake centerline curve with a minimum vertical position around $x/D \approx 19$, see Figure 3.7b. Therefore the upwards trajectory of the upper vortex row can't be solely because of vortex street widening. When the strengths of these vortices are compa-

**(a)** $y_w/D = 0.75$



**(b)** $y_w/D = 1.0$



**(c)** $y_w/D = 2.0$
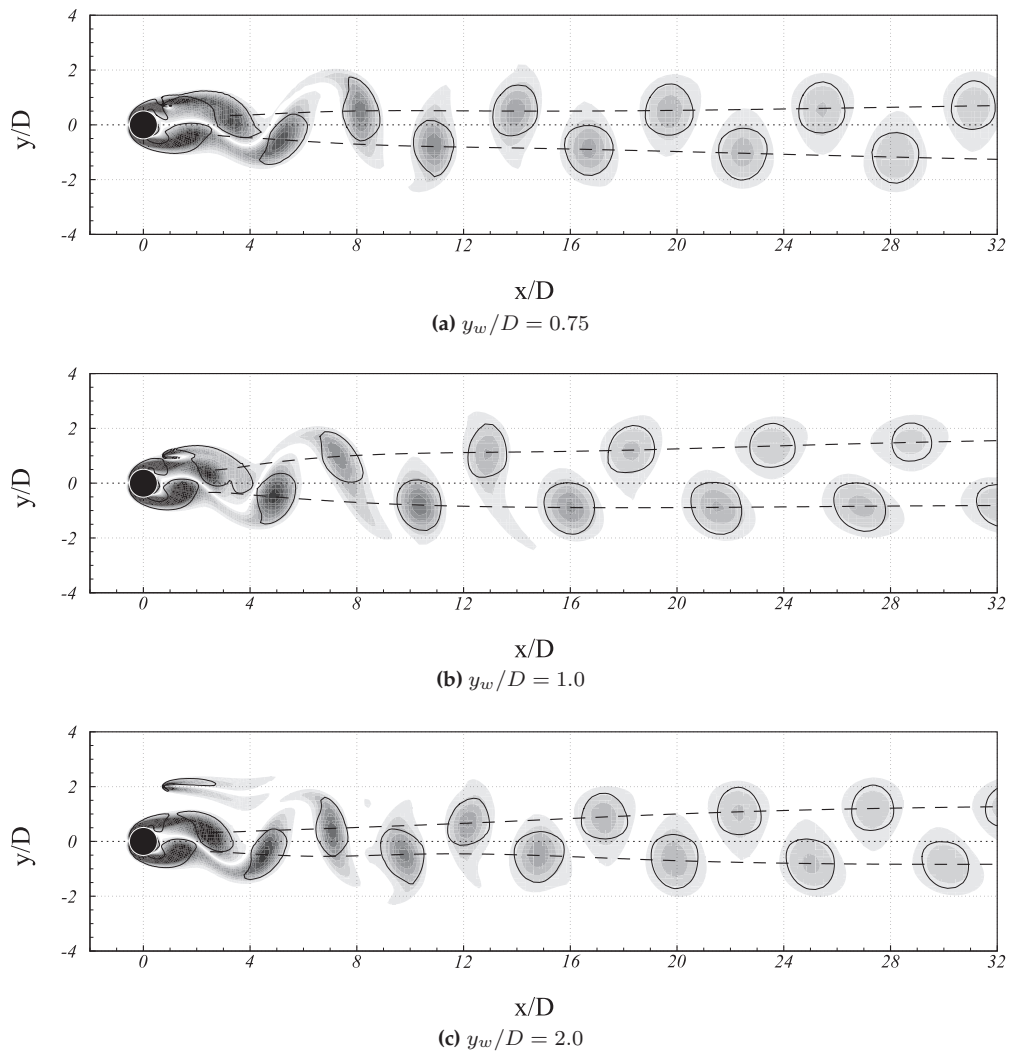
**Figure 3.5:** *Flow field characteristics for the sample cases obtained from SEM simulations. Contour plot indicates the vorticity field, solid lines are $\lambda_2 = -0.1$ contour lines and dashed lines represent the vortex trajectories for the upper and lower vortex rows. [$Re = 100$, $x_w/D = 0.75$].*
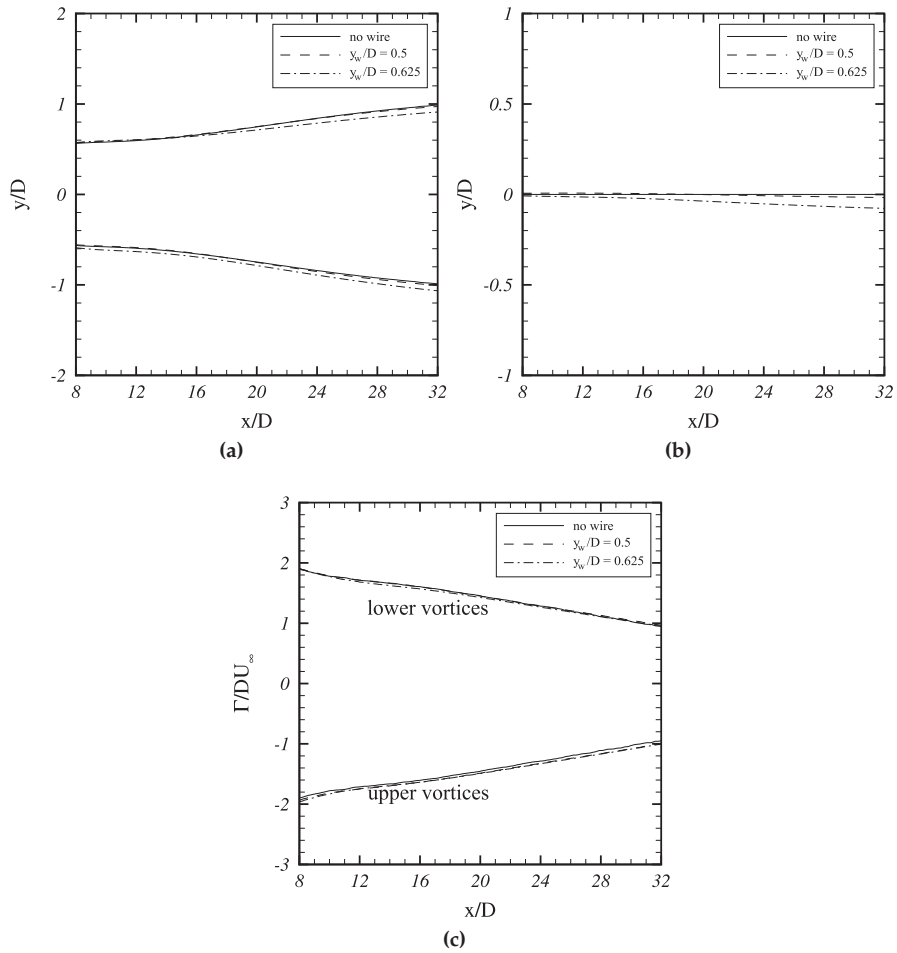
**Figure 3.6:** *Wake properties obtained from SEM simulations at the wire positions of $y_w/D = 0.5$ and $y_w/D = 0.625$. (a) Vortex trajectories, (b) Wake centerlines, (c) Vortex strengths. [$Re = 100$, $x_w/D = 0.75$].*
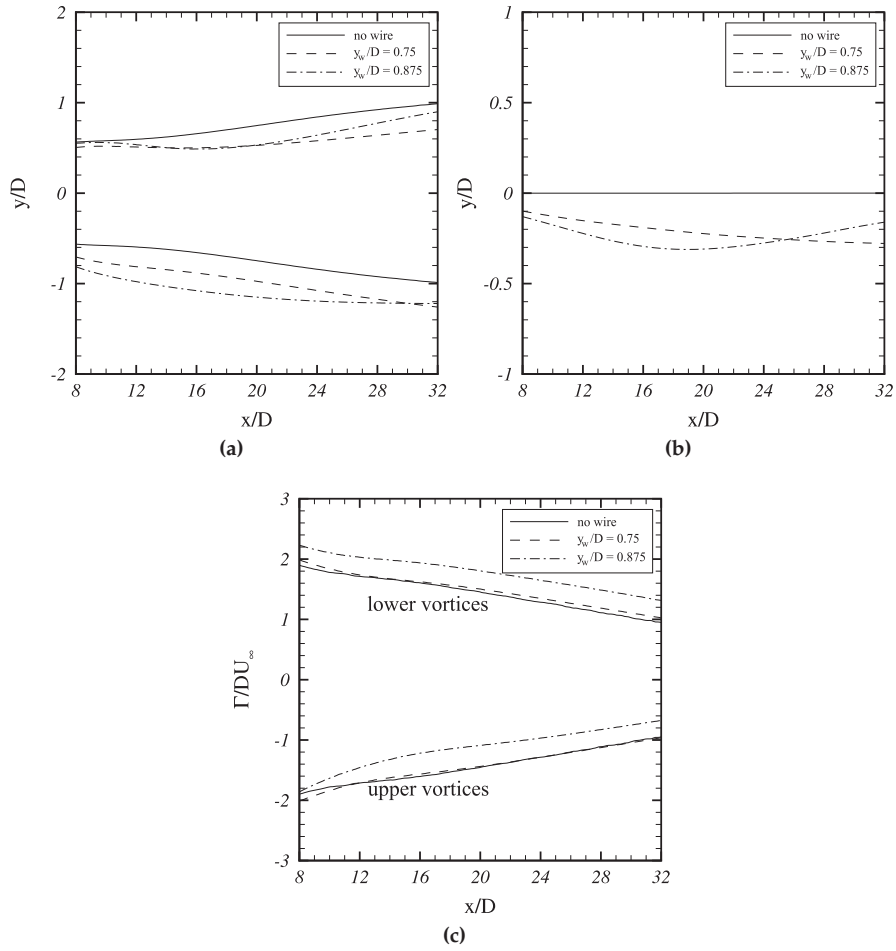
**Figure 3.7:** *Wake properties obtained from SEM simulations at the wire positions of* $y_w/D = 0.75$ *and* $y_w/D = 0.875$. *(a) Vortex trajectories, (b) Wake centerlines, (c) Vortex strengths.* $[Re = 100, x_w/D = 0.75]$.
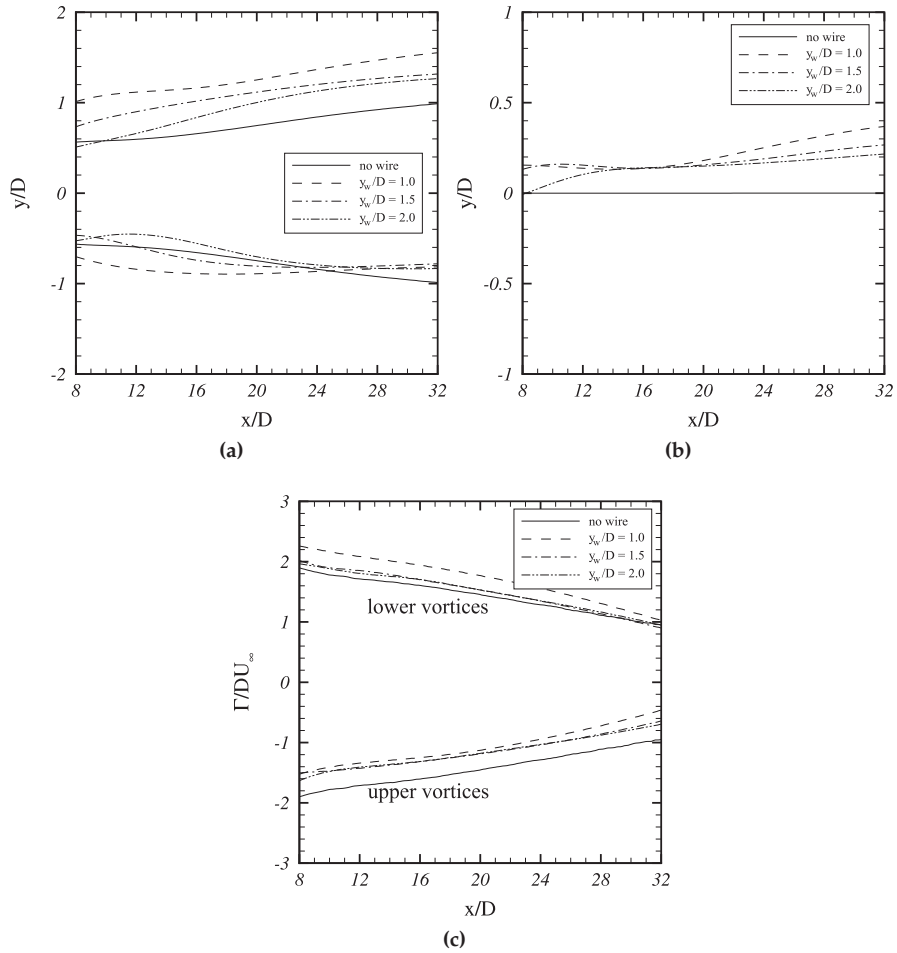
**Figure 3.8:** *Wake properties obtained from SEM simulations at the wire positions of $y_w/D = 1.0$, $y_w/D = 1.5$ and $y_w/D = 2.0$. (a) Vortex trajectories, (b) Wake centerlines, (c) Vortex strengths. [$Re = 100$, $x_w/D = 0.75$].*

red, one can see that both the upper and lower vortices in the $y_w/D = 0.75$ case have almost the same strength as the reference non-wired case, as shown in Figure 3.7c. On the other hand, the upper vortices for $y_w/D = 0.875$ case are weaker and the lower vortices are stronger than their counterparts in the non-wired case. A downward deflection of the vortex street can be caused by a strength difference between the upper and lower vortex rows, as observed for the heated cylinder case in Kieft et al. [41]. This possibly explains the downward deflection for the $y_w/D = 0.875$ case. However, such a strength difference is not found for the $y_w/D = 0.75$ case. This point will be elucidated in more detail using Point Vortex simulations.

The wake behavior for the last three cases $y_w/D = 1.0, 1.5$ and $2.0$ belong to the third group, where the overall tendency is upwards, see Figure 3.8a. The trajectory analysis shows that the highest deviation from the reference case occurs for the wire position of $y_w/D = 1.0$. The upper vortices follow a higher path than for the other cases. Although the position of the wire is out of the upper shear layer of the cylinder, the effect on the trajectories is prominent. Especially in the trajectories of the upper row vortices there is a considerable deviation observed from the reference situation. The vortex centerlines which are shown in Figure 3.8b confirm the upwards deflection of the wakes for the three cases. It can easily be noted that the highest upwards deflection is for the $y_w/D = 1.0$ case, which has much stronger lower vortices than the other cases, see Figure 3.8c. The lower vortices in all three cases have almost the same strength but are weaker compared to the reference case.

In Figure 3.9 a comparison of the numerical and experimental results is shown. Figure 3.9 is obtained by superposition of the numerically calculated vortex trajectories and the flow visualization results as shown in Figure 3.1. The top-figure shows the comparison for the non-wired case. Both the numerical and experimental results show the same trajectory patterns. For the $y_w/D = 0.75$ case, the downwards deflection of the upper vortex row in the experimental results is larger than in the numerical result, see Figure 3.9b. The lower vortex row trajectory matches the flow visualization results quite well. For $y_w/D = 1.0$, the wake-axis moves upwards in both the experiments and the calculations, Figure 3.9c. Also the individual vortex trajectories show the same trend, although the negative deflection in the lower vortex row is somewhat larger in the experiments.

### 3.3.2 Assessment of vortex strengths

The effect of a wire on the strength difference is further analysed by defining two additional parameters; local period averaged vorticity flux and total period averaged vorticity flux. The local period averaged vorticity flux is defined as the flux of vorticity passed through cross-stream line $x/D = 1$ and is formulated as:

$$\overline{\phi_{\omega_z}(y)} = \frac{1}{T_{shed}} \int_{T_{shed}} u(y)\omega_z(y)\mathrm{d}t \tag{3.1}$$

**(a)** *no wire*



**(b)** $y_w/D = 0.75$



**(c)** $y_w/D = 1.0$
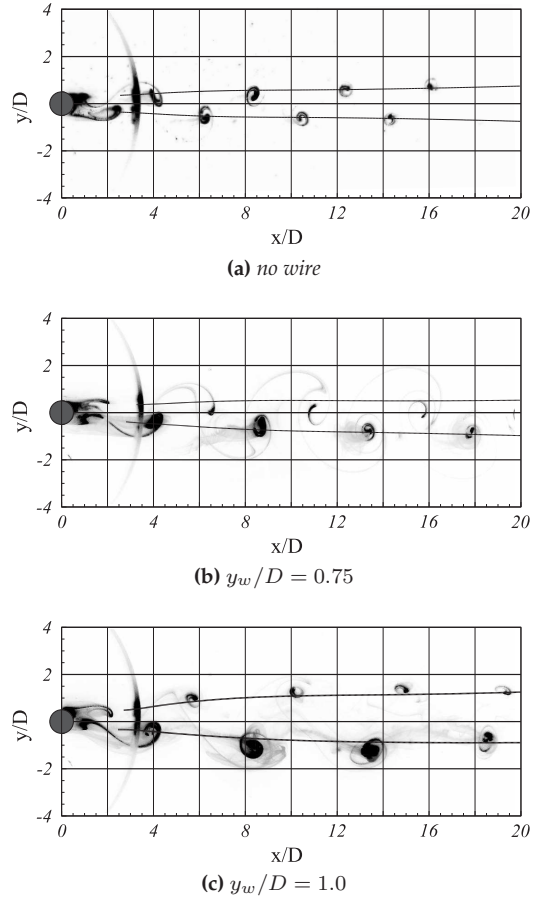
**Figure 3**.**9:** *Snapshots from flow visualization experiments and vortex trajectories obtained from SEM simulations (solid lines). [$Re = 100$, $x_w/D = 0.75$].*

| Wire position | $|\Gamma_U|$ | $\Gamma_L$ |
|---|---|---|
| no wire | 1.633 | 1.633 |
| $y_w/D = 0.5$ | 1.671 | 1.636 |
| $y_w/D = 0.625$ | 1.666 | 1.598 |
| $y_w/D = 0.75$ | 1.596 | 1.648 |
| $y_w/D = 0.875$ | 1.267 | 1.963 |
| $y_w/D = 1.0$ | 1.273 | 1.980 |
| $y_w/D = 1.5$ | 1.347 | 1.745 |
| $y_w/D = 2.0$ | 1.340 | 1.735 |

**Table 3**.**2:** *Circulation values of vortices at downstream position $x/D = 15$.*

where $T_{shed}$ is the shedding period. The integration of $\overline{\phi_{\omega_z}(y)}$ over the cross-section $x/D = 1$ gives the total period averaged vorticity flux $\Phi$, which is a measure of all upstream produced vorticity which possibly ends up in the vortex structures. For the upper half of the wake the integration domain is taken as $y = [0, L]$. The total period averaged vorticity flux $\Phi_U$ then becomes:

$$\Phi_U = \frac{1}{L} \int_0^L \overline{\phi_{\omega_z}(y)} \mathrm{d}y \tag{3.2}$$

Similarly, for the lower half of the wake the total period averaged vorticity flux $\Phi_L$ is based on the integration domain $y = [-L, 0]$.

From Figures 3.7c and 3.8c, it can be seen that the presence of a wire has a relatively large impact on the circulation values for both the upper and lower vortex rows. In Table 3.2 the circulation values are presented for downstream position $x/D = 15$. From this table it can be seen that for wire position values $y_w/D \geq 0.875$ the upper vortices become weaker due to the presence of the wire and the lower vortices become stronger, and the question could rise why that is. To answer this question further assessment of the effect of the wire on the vortex strengths can be done by evaluating the vorticity produced by the main cylinder and the wire. For this purpose the total period averaged vorticity flux defined in Equation 3.2 is used.

In Figure 3.10a, the values of $\Phi_U$ and $\Phi_L$ are shown with respect to the wire position. It is obvious that despite the asymmetry in the wake, the total circulation entering the wake from both sides of the cylinder is constant, i.e. $\Phi \approx |\Phi_U| \approx \Phi_L$, and this constant depends on the position of the wire. Assuming that all the circulation transported into the wake during one shedding period ends up in a vortex, one would expect the quantity $\Phi T_{shed}$ to be directly proportional to the average vortex strength $\Gamma_{ave} = (|\Gamma_U| + \Gamma_L)/2$, i.e. $\Phi T_{shed} \propto \Gamma_{ave}$ or $\Phi \propto \Gamma_{ave} f_{shed}$. From Figure 3.10a and 3.10b it can be seen that there is indeed a high correlation between the two curves of $\Phi$ and $\Gamma_{ave} f_{shed}$. As a measure of the vortex strengths, the circulation values from Figures 3.6c, 3.7c and 3.8c at the downstream position of $x/D = 15$ are taken, as presented in Table 3.2.

As can be seen from the Figures 3.4 and 3.10a, for each wire position $\Phi$ and $f_{shed}$ are highly correlated for both the upper and lower halves of the wake. Thus, when $\Gamma_U$ is reduced by the effect of the wire, then $\Gamma_L$ should increase in order to fulfill the condition $\Phi \propto \Gamma_{ave} f_{shed}$. This explains the increase of the lower vortex strengths for the $y_w/D = 0.875$ and 1.0 cases. On the other hand, as concluded from Table 3.2 for the $y_w/D = 1.5$ and 2.0 cases, the upper vortices are weaker as compared to the non-wired case but now the lower ones remain almost at the same strength. This looks in contradiction with the discussion above. However, examining the instantaneous vorticity fields in Figure 3.11 for these two cases reveals that the vorticity generated by the wire does not directly contribute to the vortex formation. On the other hand, the negative vorticity originating from the wire seems to interact with the upper
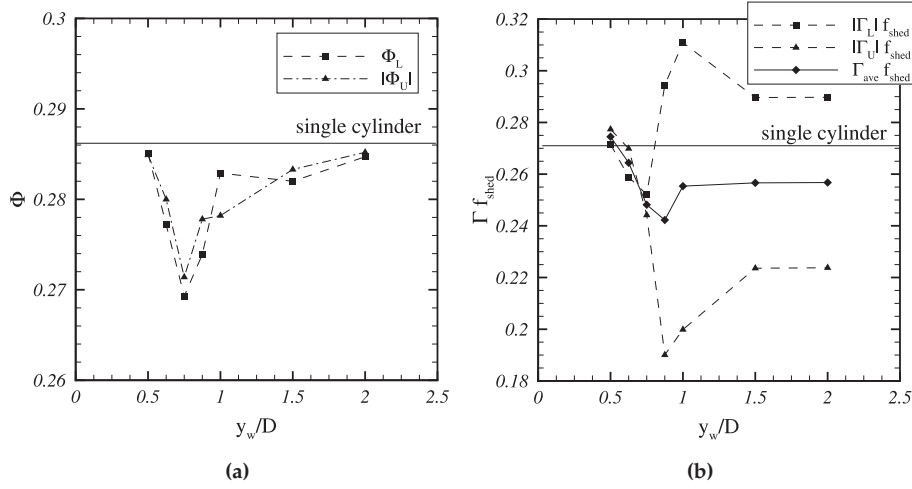
**Figure 3**.**10:** *The effect of wire position on: (a) Total period averaged vorticity flux at cross section $x/D = 1$ [$|\Phi_U|$: upper half of the wake, $\Phi_L$: lower half of the wake.]; (b) Circulation times shedding frequency at $x/D = 15$ [$\Gamma_U$: upper vortices, $\Gamma_L$: lower vortices].*

vortex which is shed from the main cylinder at some distance after its formation. Probably this explains why the Strouhal number for these two cases is almost the same as for the non-wired case. It is likely that this interaction causes the upper vortices to become weaker without affecting the strengths of the lower vortices.

## 3.4   Analysis of vortex arrangement in the wake

The vortex arrangement in the wake can be a factor for the wake deflection. To evaluate the effect of the wire on the vortex arrangement the Point Vortex approach is used. For that purpose, each vortex which is out of the formation region is assumed as a point vortex. In Figure 2.13 the layout of the wake was shown. The vortex arrangement is assessed using the vortex distance ratio $\delta_1/\delta_2$. For the von Kármán vortex street configuration, obviously the ratio of $\delta_1/\delta_2$ is equal to 2 as shown in Figure 3.12a. Other possible vortex arrangements are also shown in Figures 3.12b and 3.12c for different values of the distance ratio.

In Figure 3.13 the distance ratio $\delta_1/\delta_2$ as deduced from SEM calculations is shown for the different cases. The distance ratio is equal to 2 for the single cylinder case where there is no deflection at all. Throughout the domain the $\delta_1/\delta_2$ ratio is slightly above 2 for the $y_w/D = 0.5$ and $0.625$ cases. For the $y_w/D = 0.75$ case the ratio is substantially larger than 2 but slowly decreasing downstream. For the $y_w/D = 0.875$ case, the curve crosses the $\delta_1/\delta_2 = 2$ line around $x/D = 15$. This point corresponds
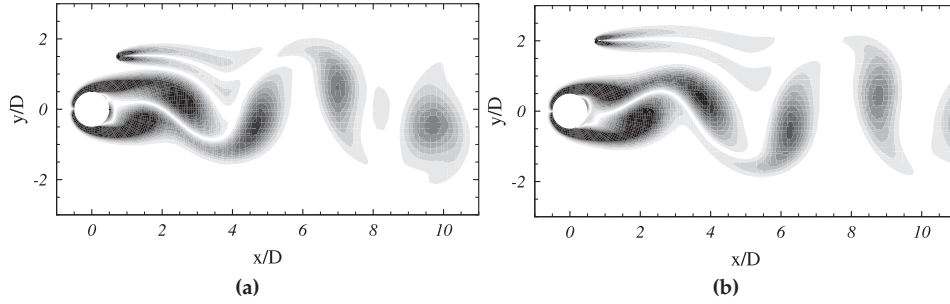
**Figure 3.11:** *Instantaneous vorticity fields of (a) $y_w/D = 1.5$; (b) $y_w/D = 2.0$.*
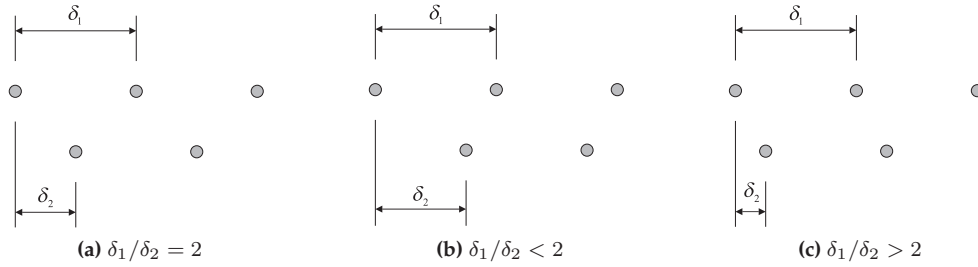


**Figure 3.12:** *Point Vortex layouts for different spacing ratios.*

more or less to the point where the wake deflection changes from downwards to upwards. For the cases $y_w/D \geq 1.0$ the distance ratio curves always remain below 2. The most severe trend is for the $y_w/D = 1.0$ case where the divergence of the $\delta_1/\delta_2$ curve is the highest.

Point Vortex simulations are done for the assessment of the vortex arrangement and strength difference on the wake deflection. The quantitative values used in the model are in the same order of magnitude as the values coming out of the numerical simulations discussed above. Firstly, the behavior of vortices with equal strengths and then the arrangement with stronger upper vortices are evaluated.

### 3.4.1 Equal vortex strengths

First part of the simulations comprises evaluation of the vortex distance ratio. For this purpose, the vortex strengths are taken to be $|\Gamma_U| = |\Gamma_L| = 2$, where $\Gamma_U$ and $\Gamma_L$ are the strengths of upper and lower vortices respectively. The point vortices are initially distributed according the spacing ratio of $a/\delta_1 = 0.281$ for which the von Kármán vortex street is considered to be stable. As shown in Figure 3.14a, the simu-
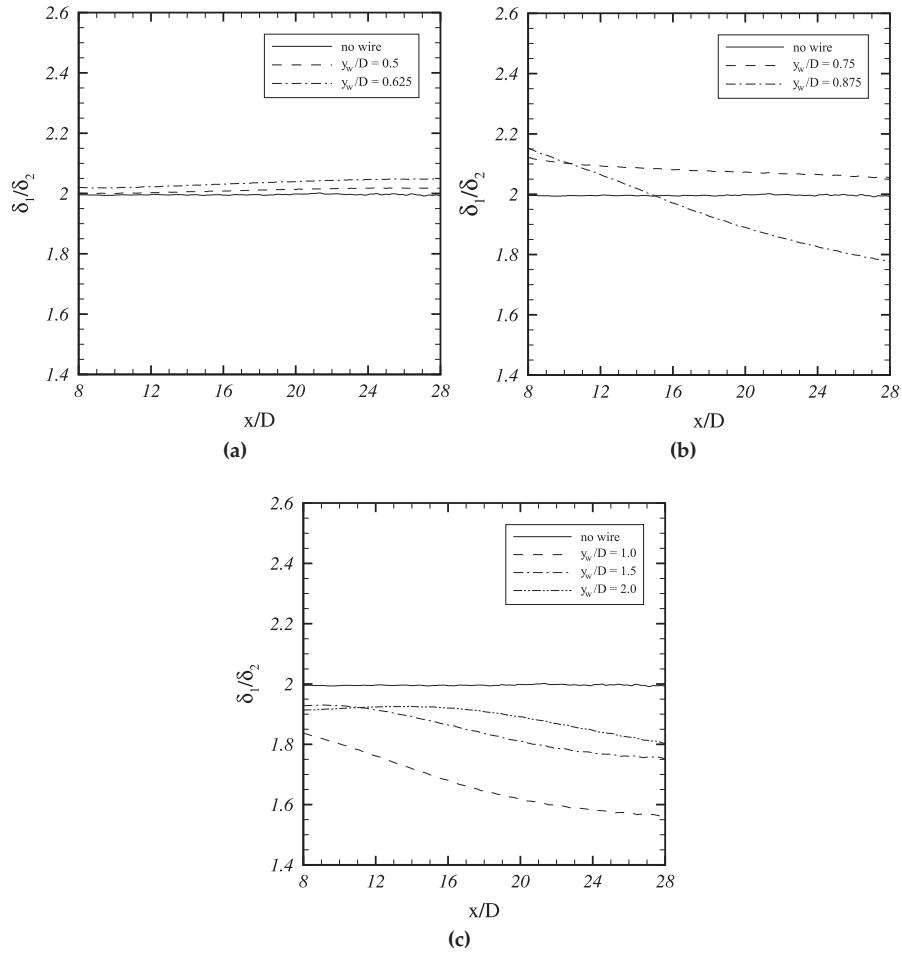
**Figure 3.13:** *Downstream variation horizontal distance ratio $\delta_1/\delta_2$. Note that $\delta_1/\delta_2 = 2$ corresponds to stable von Kármán vortex street. The results are obtained from SEM simulations. [$Re = 100$, $x_w/D = 0.75$].*

lation results for the von Kármán Vortex Street show that there is no deflection in the trajectories. However, when the upper vortices are moved downstream in the initial vortex arrangement, i.e. to the right in Figure 2.13, and the simulation is repeated the trajectory of the vortices show a downwards deflection. It should be noted that in this configuration the spacing ratio is $\delta_1/\delta_2 = 2.4$ and the vortex arrangement is as in Figure 3.12c. Similarly, when they are moved upstream the wake goes upwards and the spacing ratio is $\delta_1/\delta_2 = 1.6$, as shown in Figure 3.12b. The Point Vortex simulation results which are presented here, show that modified vortex arrangement and wake deflection can be achieved without having strength difference between the vortices. In the modified wake vortex arrangement, the induced vertical velocity components $v_j$ of Equation 2.17 are not canceled out anymore. Because of this non-zero vertical velocity component wake deflection is seen.

### 3.4.2 Stronger upper vortices

In the second part of the Point Vortex Simulations the initial vortex configuration is fixed in order to evaluate the effect of the strength difference. The configuration has an initial vortex distribution of $a/\delta_1 = 0.281$ like the von Kármán Vortex Street configuration. The simulations are done for the values $\Gamma_U = -2$ and $\Gamma_L = 1.2$. The resulting vortex trajectories are shown in Figure 3.14b where the tendency of the wake is downwards.

This situation is explained as follows. In the Point Vortex model, the resultant horizontal velocity of the lower vortices, $u_j \mid_{lower}$ in Equation 2.16, is calculated as the free-stream velocity minus the total induced velocity. When the upper vortices are stronger, they will induce a higher negative horizontal velocity on the lower vortices. An increased induced negative horizontal velocity of the lower row makes the lower vortices to move slower than the upper vortices. Thus, the lower vortices become closer to the upstream upper vortices as they move downstream. This results in a point vortex arrangement with a spacing ratio $\delta_1/\delta_2 > 2$ as in Figure 3.12c. In the modified wake vortex arrangement, the induced vertical velocity components $v_j$ are not canceled out anymore. A negative vertical velocity is induced for each vortex in the array, which makes the wake to move downwards. The opposite conclusion is also true. When the lower vortices are stronger, the upper ones move slower and become closer to the upstream lower vortices and the wake moves up. A detailed analysis for the similar situation of heated cylinder wake can be found in Kieft et al. [66] and Kieft et al. [41]. In that case the upper vortices are stronger than the lower vortices and the wake trajectory moves downwards.
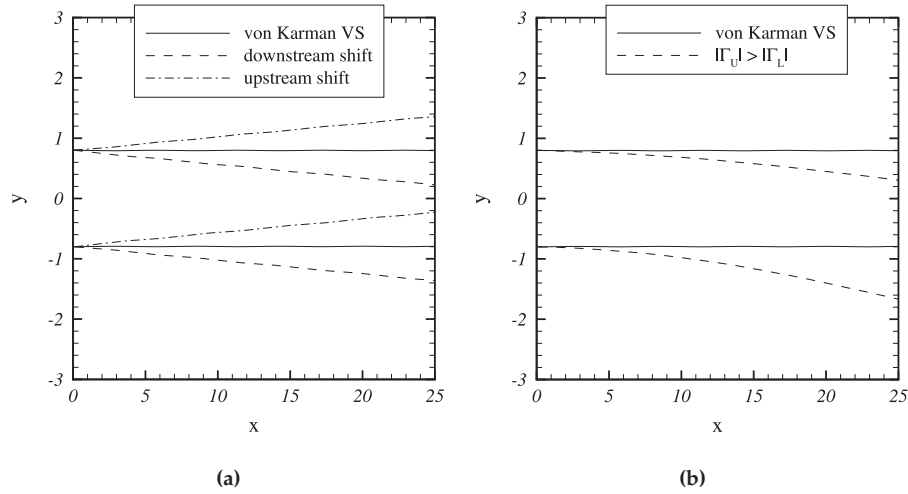
**Figure 3**.**14:** *Point Vortex Simulations for various cases. (a) Effect of position change of upper vortices, $|\Gamma_U| = |\Gamma_L|$. (b) Effect of strength difference, $|\Gamma_U| > |\Gamma_L|$.*

## 3.5   Lift and drag characteristics of main cylinder

In addition to its wake characteristics, lift and drag characteristics of the main cylinder are also evaluated for different positions of the wire for which the results are illustrated in Figure 3.15. The lift and drag of the cylinder are calculated by integrating the stress components on the surface of the cylinder.

The comparison of time averaged drag coefficients in Figure 3.15a shows that a drag reduction is obtained for all wire positions. The highest reduction compared to the single cylinder case is $6.4\%$ and seen at wire position of $x_w/D = 0.75$. This value is much lower than the value reported by Dalton et al. [64] for the same Reynolds number but for a different configuration. They found a drag reduction of $33\%$ when the vortex shedding was suppressed. The variation of the Strouhal number as presented in Figure 3.4 and the mean drag coefficient show a similar behavior as function of the wire position, however with slightly different location for the minimum value. The correlation in the trend is in good agreement with the conclusions of Strykowski and Sreenivasan [59] who stated that mean drag reduction can also be seen in some cases where the vortex shedding frequency is reduced or suppressed. The fluctuating lift coefficient in Figure 3.15b is following the same trend as the mean drag coefficient. Similarly, the highest damping of the fluctuating lift coefficient occurs again at the same location with $46.9\%$ reduction when compared to the single cylinder case.

Breaking the symmetry of the circular cylinder flow with a wire clearly shows its
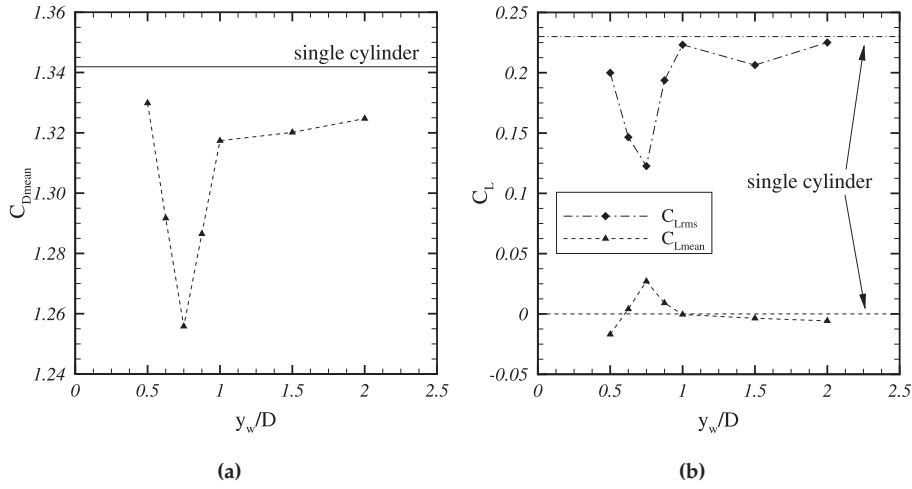
**Figure 3**.**15:** *Comparison of lift and drag characteristics of the main cylinder. (a) Mean drag coefficient* $C_{D_{mean}}$. *(b) Mean lift coefficient* $C_{L_{mean}}$ *and fluctuating lift coefficient* $C_{L_{rms}}$.

effect on mean drag coefficients and fluctuating lift coefficients as well as on mean lift coefficients. It should be recalled from the previous sections that the highest uniform downward deflection occurs at a wire position of $y_w/D = 0.75$, where minimum mean drag and fluctuating lift coefficients are seen. This position also corresponds to the wire location where the highest positive mean lift coefficient is found, Figure 3.15b. It is likely that a downwards deflection is the signature of a mean positive lift acting on the main cylinder.

It is known from basic fluid dynamics theory that a positive lift is related to a negative circulation around the cylinder [57]. This negative circulation on its turn results in downwards deflected streamlines, i.e. a negative deflection of the vortex street. This global picture seems to hold for wire position $y_w/D = 0.75$. For other positions of the wire less clear or even conflicting results are observed.

## 3.6 Concluding remarks

In this chapter, the two-dimensional case of a wire disturbed cylinder wake flow at $Re = 100$ is studied. SEM simulations and flow visualization experiments are used to evaluate the effects of the wire on wake. The primary effect of the wire is reducing the velocity fluctuations in the vortex formation region of the cylinder. Additionally, the shedding frequency is also reduced. The amount of reduction depends on the position of the wire. The results indicate that there is an optimal point for maximi-

| Configuration | St number | | $\|\Gamma_U\| - \|\Gamma_L\|$ | Deflection |
|---|---|---|---|---|
| no wire | 0.1660 | $\delta_1/\delta_2 = 2$ | 0.000 | no deflection |
| $y_w/D = 0.5$ | 0.1658 | $\delta_1/\delta_2 > 2$ | 0.035 | downwards |
| $y_w/D = 0.625$ | 0.1624 | $\delta_1/\delta_2 > 2$ | 0.064 | downwards |
| $y_w/D = 0.75$ | 0.1532 | $\delta_1/\delta_2 > 2$ | -0.063 | downwards |
| $y_w/D = 0.875$ | 0.1503 | $\delta_1/\delta_2 > 2$ | -0.714 | downwards |
| $y_w/D = 1.0$ | 0.1569 | $\delta_1/\delta_2 < 2$ | -0.644 | upwards |
| $y_w/D = 1.5$ | 0.1656 | $\delta_1/\delta_2 < 2$ | -0.341 | upwards |
| $y_w/D = 2.0$ | 0.1671 | $\delta_1/\delta_2 < 2$ | -0.351 | upwards |

**Table 3.3:** *Summary of Strouhal number, the distance ratio, the strength difference $\|\Gamma_U\| - \|\Gamma_L\|$ values at $x/D = 20$ and wake deflection direction for different wire positions. [Re = 100]*

zing the effect of the wire, at $y_w/D = 0.875$, which is slightly over the maximum vorticity line in the shear layer. In agreement with the discussion of Strykowski and Sreenivasan [59], it can be concluded that the effect of the wire is to damp the growth of disturbances which in turn results in a lower shedding frequency.

The secondary effect of the wire is seen in the wake of the cylinder, i.e. the kinematics of the vortices. The major findings on the effect of the wire on the wake vortex arrangement are summarized in Table 3.3. The wire results in a modified vortex arrangement in the wake and a strength difference between the upper and lower vortices. For the $y_w/D = 0.75$ case, both the upper and lower vortices have almost the same strength as compared to the reference single cylinder case. However, the placement of the wire apparently induces a different formation process for the upper and lower row vortices, causing the upper vortices to position themselves closer to the previously shed lower vortices. As shown in the Point Vortex Simulations, the resulting modification of the vortex arrangement causes the downwards deflection of the wake. Similarly, the wake goes upwards for the opposite case where the upper vortices are closer to the subsequently shed lower vortices. .

When the change in vortex arrangement is combined with a strength difference, the effect of the wire becomes even more severe, as in the $y_w/D = 1.0$ case. In this situation, the stronger lower vortices induce a higher negative horizontal velocity for the upper vortex row. This higher induced velocity makes each upper vortex to move slower and become closer to the subsequently shed lower vortex.

Another interesting result is seen in the $y_w/D = 0.875$ case, where the upper vortices are positioned closer to the previously shed lower vortices in the formation region, like in the $y_w/D = 0.75$ case. Because of this, the wake has a downwards tendency like in the $y_w/D = 0.75$ case. On the other hand, the higher strength of the lower vortices makes the upper vortices to move slower and become closer to the subsequently shed lower vortices. Because of this reason the wake in this particular case changes its tendency in the downstream region of the wake and starts to

go upwards. This phenomenon can also be seen in the visualization results for the $y_w/D = 1.0$ case as presented in Figure 3.1.

Based on the observations above a hypothesis about the wake deflection in the two-dimensional case is formulated: *the deflection of the wake is primarily caused by a modification of the vortex arrangement in the wake*. The strength difference between the upper and lower row vortices is only a tool for achieving a modification of the vortex street like in the case of a heated cylinder [41, 66]. A repositioning of the vortices is a necessary and sufficient condition for the wake deflection to occur. The conclusions from the present study state that;

1. $\delta_1/\delta_2 = 2$: undisturbed von Kármán Vortex Street with no deflection.

2. $\delta_1/\delta_2 > 2$: downwards deflection.

3. $\delta_1/\delta_2 < 2$: upwards deflection.

As concluding remarks, it can be said that placing a very thin wire in the near-wake of a cylinder not only changes the vortex shedding frequency by effecting the velocity fluctuations but also changes the formation process of the vortices. The change in the formation process results in a modified vortex arrangement which causes the deflection of the wake.

# Period-doubling in Mode-C transition for $Re \geq 180$

## 4.1 Introduction

In fluid mechanics, several ways are defined for a flow system to go into a turbulent, i.e. chaotic, state. Drazin [67] discussed that the period-doubling transition is one of the transition mechanisms of a such a process. Due to the flow system investigated, the period-doubling transition will be briefly discussed here.

Basically, period-doubling is a transition route to chaos through a subharmonic cascade, as summarized by Kundu and Cohen [68]. In a typical non-linear system, as the nonlinearity parameter R is increased, there exists a limit cycle with a frequency $f$. However, in a system with period-doubling character, the further increase of R generates additional frequencies in the form of subharmonic frequency components of $f/2, f/4, f/8, \ldots$. Each time when a subharmonic is added to the system, the period is doubled without losing the periodicity of the system.

Libchaber et al. [69] reported that some cases of Rayleigh-Bénard convection might be an example of a period-doubling type instability. Their results were based on experiments. They wrote that the rolls of Rayleigh-Bénard convection showed an oscillatory behavior with frequency $f$ for $Ra = 2Ra_{crit}$. Furthermore, they presented a spectrum showing subharmonic oscillations at frequencies $f/2, f/4, f/8, f/16, f/32$ for $Ra > 2Ra_{crit}$.

A second example for period-doubling in fluid flows is the wake behind circular

rings. Sheard et al. [30] provided computational results and first experimental obser-
vations about the existence of the subharmonic mode Mode-C in the wake of a ring
with aspect ratio $AR = 5$ at $Re = 200$. However, their main conclusion was that the
period-doubling bifurcation associated with the development of Mode-C wake does
not initiate a period-doubling cascade in the vortex street.

Another possible example is the wire-disturbed circular cylinder wake in transi-
tion regime. Zhang et al. [13] originally showed that transition of a wired cylinder
wake exhibits a different transition mode and named it as Mode-C. The framework
of this chapter is to analyze the traces of period-doubling behavior in Mode-C tran-
sition in detail.

Firstly, general characteristics of Mode-C transition at $Re \geq 180$ are determined
in several different ways. The wire is fixed at position of $(x_w/D, y_w/D) = (0.75, 0.75)$
throughout all the experiments mentioned in this chapter. The flow visualization ex-
periments illustrate the global picture of the phenomena and provides a global view
of the physics of wake transition. The point velocity analysis provides information
about local flow characteristics and period doubling nature of the wake. Processing
the point velocity data leads to several other characteristic properties of Mode-C
wake such as phase plots, power spectra and Strouhal numbers.

Secondly, to understand the physical mechanism of the period doubling charac-
ter of the wake, the instantaneous vorticity patterns of the primary and secondary
vortices are shown using PIV vector fields of the near-wake. Image sequences from
flow visualization experiments are used to analyze the time evolution of secondary
vortices. The overall analysis of the physics of the wake and feedback mechanism of
vortices gives insight into the origin of the period-doubling character of the Mode-C
transition.

## 4.2  General characteristics of Mode-C transition

### 4.2.1  Overview by flow visualization experiments

As a first step, the influence of a wire on the cylinder wake flow was investigated
by three-dimensional flow visualizations which revealed the general physics of the
Mode-C structures in transition regime. The global effects of a wire on the laminar
wake transition of a circular cylinder are shown in Figure 4.1, which contains snap-
shots taken with the camera placed on top of the setup, see Figure 2.4a. The frees-
tream velocity is in the positive $X$-direction and the camera axis is in the negative
$Y$-direction in the global coordinate system. The original images are recorded by a
digital camera and later on processed by image processing software. Each snapshot
in the figure represents the vortex shedding phase at which the upper von Kármán
vortex starts to form. In the snapshots, von Kármán vortices, i.e. primary vortices,
are aligned along the cylinder axis while the Mode-C vortices, i.e. secondary vortices,

are formed between the primary vortices aligned in the streamwise direction.

The results in Figure 4.1 clearly show the wake transition structure in the case of a wire-disturbed circular cylinder wake. No apparent three-dimensional vortical structures are present for $Re = 165$, despite the existence of two-dimensional von Kármán vortices emerging from the cylinder. However, for $Re \geq 180$ fine-scale three-dimensional vortical structures appear in the wake, indicating a transition process. It is obvious that the critical Reynolds number for the transition, $Re_{crit}$, lies between $Re = 165$ and $Re = 180$. The Reynolds number for the onset of Mode-C instability is given as $Re = 170$ by Zhang et al. [13]. However, the experimental setup and methods used in this study did not allow an accurate determination of $Re_{crit}$.

The snapshots in Figure 4.1 show that the formed three-dimensional structures are actually secondary streamwise vortices around the primary von Kármán vortices. These secondary structures indicate the presence of Mode-C type instability in the wake transition regime, see Zhang et al. [13]. They are uniformly distributed along the span of the cylinder with a spanwise wavelength of $\lambda_z \approx 2D$. They are formed in the near-wake and continue to exist in the far-wake too.

The Reynolds number range of the experiments covers both Mode-A and Mode-B regions of natural vortex shedding. So, the results presented in Figure 4.1 indicate the replacement of natural shedding modes with a forced shedding mode (Mode-C) in the Reynolds number range of $180 - 300$. In this range, Mode-C structures get more disordered with increasing Reynolds number. However, unlike the natural wake transition there is no drastic change in the vortex structure with increasing Reynolds number. When compared to the other shedding modes (Williamson [11], Ren et al. [12]), the differences in the wake structures suggest that the physical mechanism of formation is also altered by the wire.

Figure 4.2 shows the image sequence taken during experiments for $Re = 195$. In the page coordinate system the cylinder is on the top and the flow direction is from top to bottom. The time difference between each consequent snapshot from left to right in the figures is one shedding period which is denoted as $T_{shed}$. Examination of the instantaneous image sequence in Figure 4.2 reveals an interesting feature of the Mode-C transition. In both the left and middle snapshots, the wake behind the cylinder has the same three-dimensional structures but with a shift of approximately 1 cylinder diameter in spanwise position. The structures which appear on the line on the left snapshot appear again on the line after 2 shedding periods. So, effectively, the shedding period has become 2 shedding cycles. This is an indication that Mode-C transition has a period doubling character which shows itself as shift in spanwise position of Mode-C vortices in every cycle. Period doubling behavior is observed in all of the flow visualization experiments in the wired cylinder transition regime. However, this behavior has been observed neither in non-wired cylinder nor in heated cylinder wake transition.
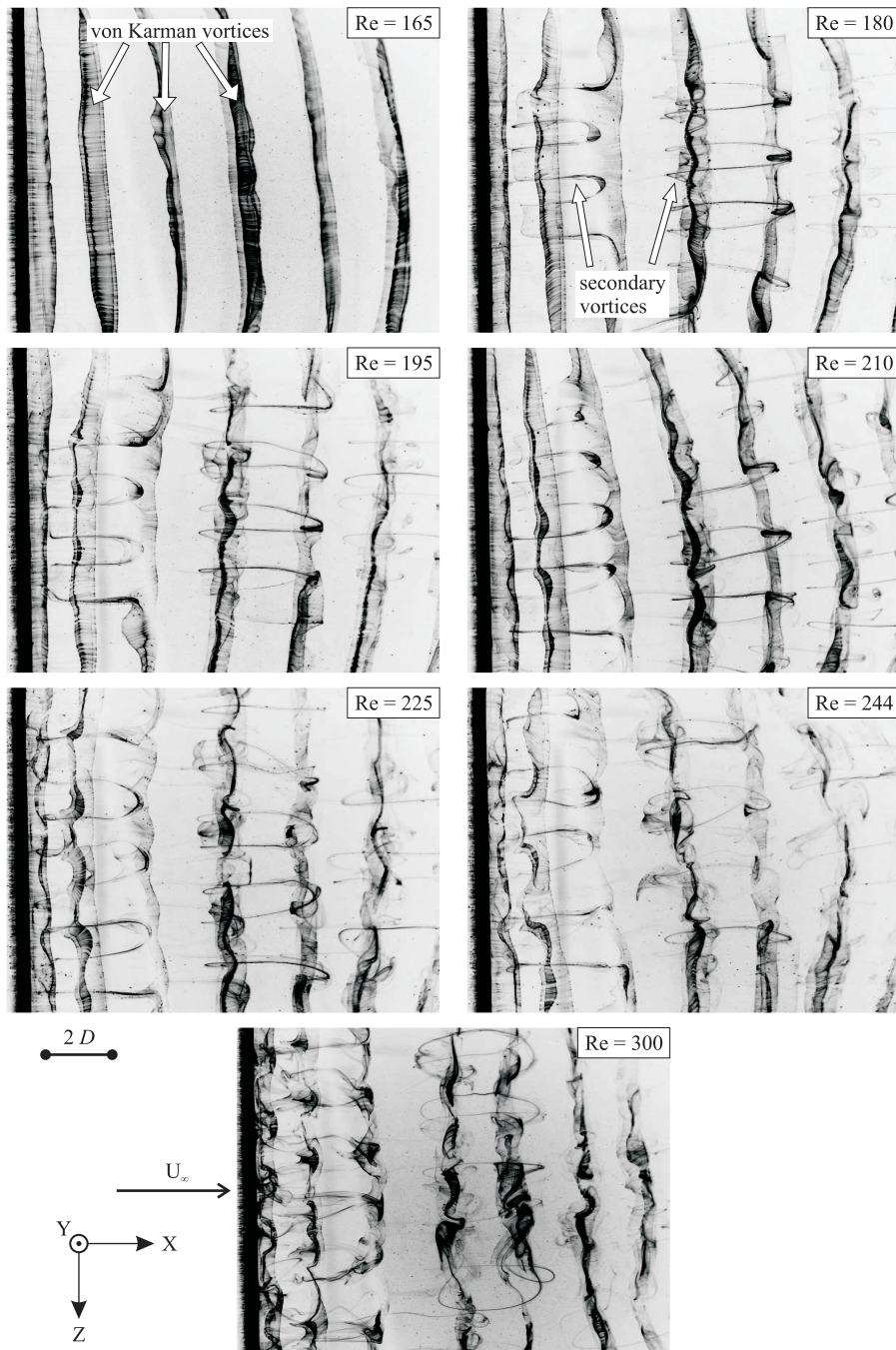
**Figure 4.1:** *Top-view visualizations of circular cylinder wake under the influence of a near-wake wire. Each picture is the instantaneous snapshot of the flow state taken at the corresponding Reynolds number. Flow direction in the pictures is from left to right.*
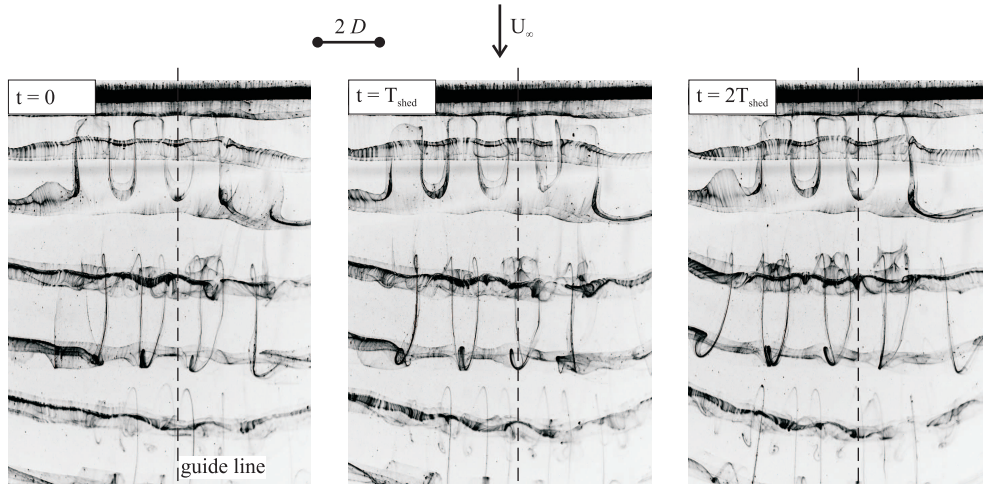
**Figure** 4.2: *Top-view visualization of Mode-C structures at* $Re = 195$. *Flow direction in the pictures is from top to bottom.*

## 4.2.2   Point velocity characteristics

The further analysis of Mode-C wake transition is done by examining point velocity data in the near-wake. The velocity data is obtained from PIV experiments by placing a data probe at specific locations and tracing the data through consecutive vector fields. The velocity fluctuations in the wake identifies the distinct characteristic properties of Mode-C transition.

Figure 4.3 exhibits cross-stream velocity variation that correspond to different Reynolds numbers of wired-cylinder wake flow. The velocity data is extracted at the point $(x/D, y/D) = (4.5, 1.5)$ from $XY-plane$ PIV measurements, see Figure 2.4b. For each graph, the velocity and time data are non-dimensionalized using corresponding free-stream and shedding period values, respectively. The shortest data record in term of shedding periods is at $Re = 100$ where the periodicity of laminar vortex shedding is apparent. In the transition regime the signal preserves its periodic nature with an irregularity whose level is increasing with Reynolds number. The nature of this irregularity can be clearly seen in the velocity-time data for $Re \geq 180$ where a distinct shape of consecutive 'W'-shaped 'high peak-low peak' pattern is displayed.

Figure 4.4 shows two cross-stream velocity signals at $Re = 180$ but obtained from different PIV experiments. Figure 4.4a represents data from $XY-plane$ and Figure 4.4b from $YZ-plane$ measurements. The location of the data probes are shown next to the corresponding graphs.
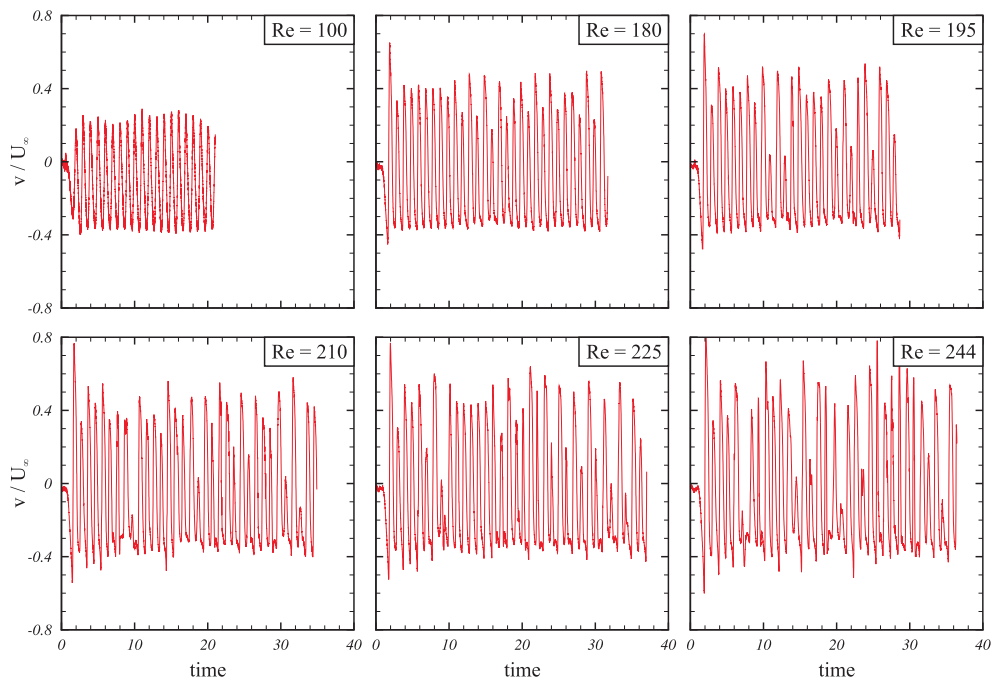
**Figure 4.3:** *Time traces of vertical velocity component $v$ for different Reynolds numbers in the Mode-C transition regime. Velocity data is obtained by using a data probe located at $(x/D, y/D) = (4.5, 1.5)$ in PIV vector fields.*

**(a)**



**(b)**
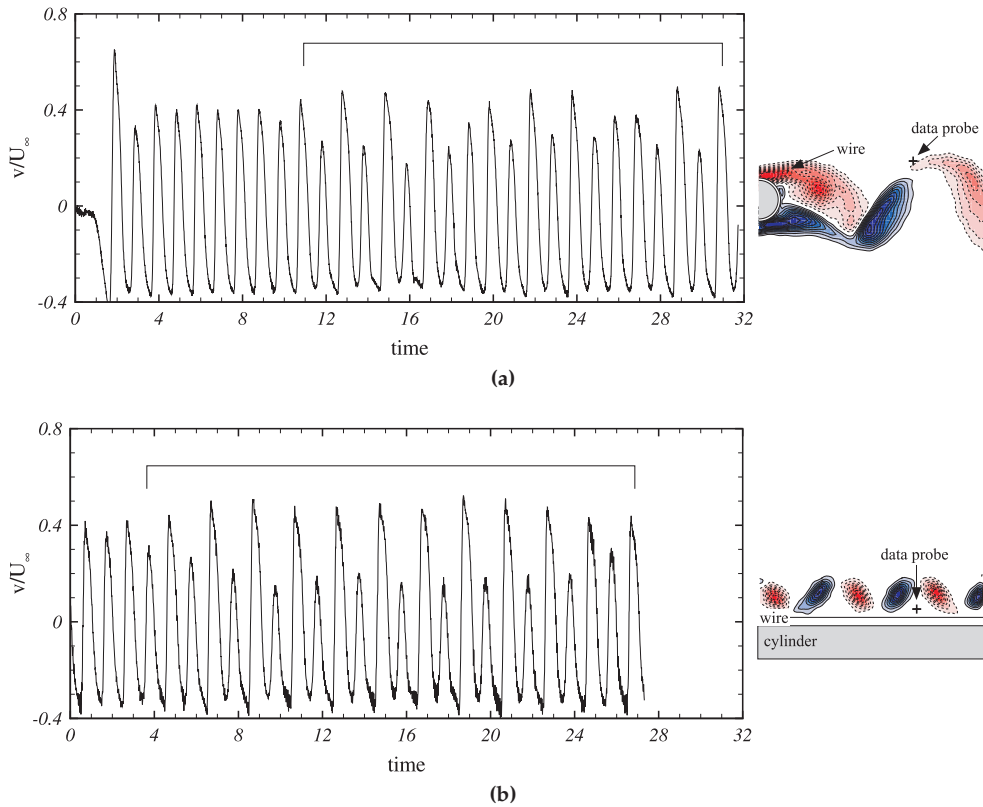
**Figure 4.4:** *Time trace of vertical velocity component $v$ in two different experiments. a) $XY - plane$ PIV experiments, $Re = 180$, data probe point is $(x/D, y/D) = (4.5, 1)$, b) $YZ - plane$ PIV experiments, $Re = 180$, data probe point is $(x_l/D, y/D) = (4.5, 1)$. The $Z - coordinate$ of the data point is selected to be between two secondary vortices. The time axis is non-dimensionalized with corresponding shedding periods of each experiment.*

**'High peak-low peak' velocity signal**

Figure 4.4 presents the typical 'high peak-low peak' velocity-time signal, as indicated by brackets in both of the graphs. This pattern is much more clear in Figure 4.4b than in Figure 4.4a due to the data probe location between the two secondary vortices where their effect on the cross-stream velocity is maximum. In Figure 4.4a, due to the nature of the experiment in $XY - plane$ measurements it was not possible to put the laser plane, hence data probe point, between the secondary vortices. Despite this fact, the signal in Figure 4.4a still contains 'high peak-low peak' pattern. In the velocity signals of other experiments this characteristic shape is also noticeable. Therefore, it can be said that 'high peak-low peak' pattern is actually the characteristic shape of the velocity time signal in Mode-C transition.
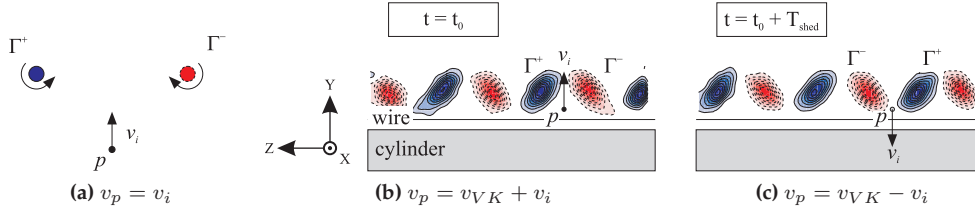
**Figure 4.5:** *Analysis of 'high-peak-low-peak' velocity profile in Mode-C wake. a) Point Vortex Model, b) Upwards induced velocity, $v_i > 0$, due to secondary vortices, c) Downwards induced velocity, $v_i < 0$, due to secondary vortices. $v_{VK}$ is vertical velocity component induced by von Kármán vortices and $v_{VK} > 0$. Blue (solid line) and red (dashed line) denote positive and negative streamwise vorticity, respectively.*
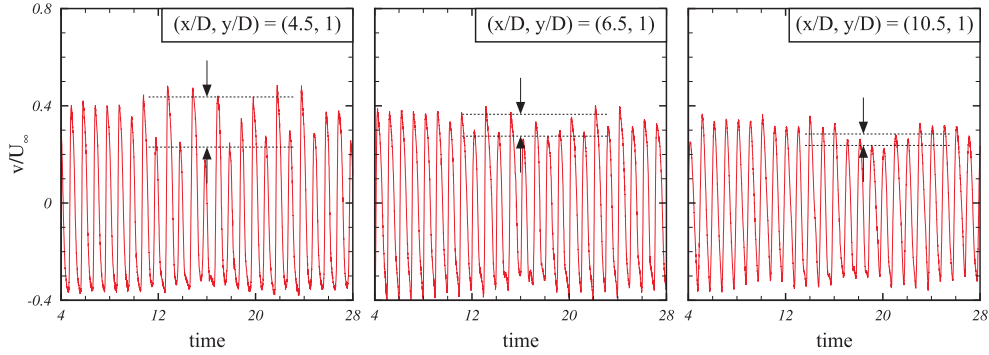


**Figure 4.6:** *Downstream variation of the vertical velocity $v$ in the upper half of the wake. $Re = 180$.*

The physical explanation for this 'high peak-low peak' pattern requires the recapitulation of the Point Vortex Model, as shown in Figure 4.5. If a point *point p* lies on the mid-line of a vortex pair as shown in Figure 4.5a, then the velocity of the *point p* is $v_p = v_i$ with $v_i$ being the total induced velocity by two counter rotating point vortices of equal strength, $\Gamma^-$ and $\Gamma^+$. Assuming that *point p* lies between two secondary vortices in Mode-C wake as shown in Figure 4.5b and Figure 4.5c, $v_p$ will consists of two components; induced velocity of primary von Kármán vortices, $v_{VK}$, and secondary vortices, $v_i$. At the vortex shedding time $t = nT_{shed}$, when the secondary vortices are at their uppermost position, $v_{VK}$ is always positive, $v_{VK} > 0$.

As seen in Figure 4.5b and Figure 4.5c the vorticity of secondary vortices changes sign after every period $T_{shed}$ which also affects the direction of induced velocity $v_i$ at *point p*. Hence, $v_p = v_{VK} + v_i$ at $t_0$ corresponds to the 'high peak' in the velocity signal and $v_p = v_{VK} - v_i$ at $t_0 + T_{shed}$ to the 'low peak'.

The above discussion shows that the difference between the 'high' and 'low'

peaks in the velocity signal is due to the induced velocity of secondary vortices, which changes sign in every shedding cycle. Figure 4.6 shows that this difference is decreasing in streamwise direction. This suggests that the induced velocity $v_i$, hence vortex strengths of secondary vortices, is decreasing and the cross-stream velocity component is converging to the value of $v_{VK}$.

**Phase plots**
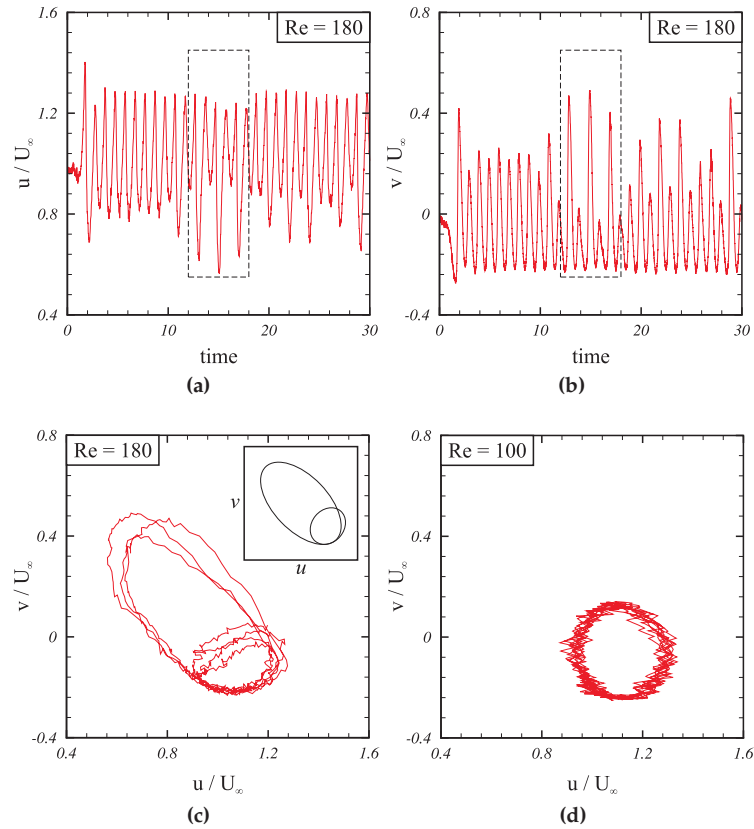


**Figure 4.7:** *Phase plot of velocity data in Mode-C transition. a) Temporal variation of $u$ velocity, b) Temporal variation of $v$ velocity, c) Phase plot of the velocity data which is shown in dashed boxes in the plots (a) and (b). Velocity data is from XY-plane PIV experiments at $Re = 180$. d) Phase plot for laminar two-dimensional flow at $Re = 100$. Data probe point in all experiments is $(u, v)(x/D, y/D) = (4.5, 1.5)$.*

The analysis of point velocity data showed that Mode-C transition regime exhibits a unique repetitive 'high peak-low peak' velocity signal pattern due to the se-
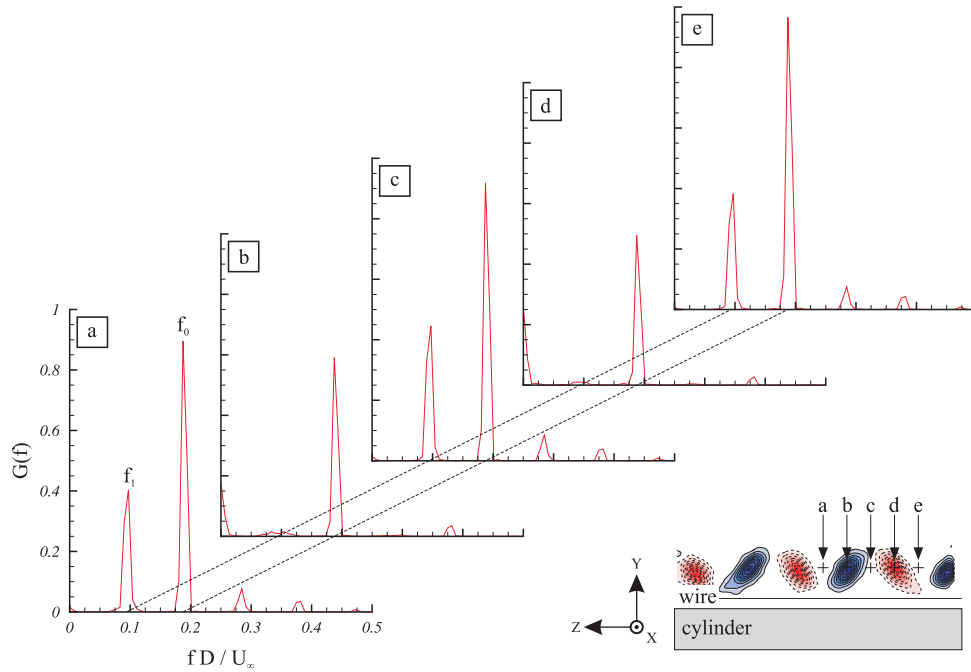
**Figure 4.8:** *Spanwise variation of $v$ velocity spectra at $Re = 180$. The streamwise and transverse coordinates of the data probe points are $(x/D, y/D) = (4.5, 1.5)$.*

condary Mode-C vortices which change sign every vortex shedding cycle. The time difference between the consecutive high peaks (or low peaks) is twice the period of the signal, which indicates that the signal has a period-doubling character. Period-doubling can also be evidenced in the phase plots of the velocity components.

Figure 4.7 presents the time variation of $u$ and $v$ velocities and their plots for Mode-C transition as well as the phase plot for $Re = 100$ for comparison. It can be seen that $u$ velocity signal also demonstrates the typical 'high peak-low peak' velocity pattern. The two velocity components are plotted against each other to obtain the phase plot of 4.7c. There is a clear difference between the phase plots of Mode-C transition flow and laminar two dimensional flow. Laminar flow demonstrates a clear single phase cycle. On the other hand Mode-C flow shows two phase cycles, one within the other.

**Power spectra**

Furthermore, spectrum analysis is used to capture the frequency content and to identify the periodicity in the velocity signal of Mode-C transition. Figure 4.8 shows the power spectra of cross-stream velocity signals obtained from $YZ - plane$ PIV mea-
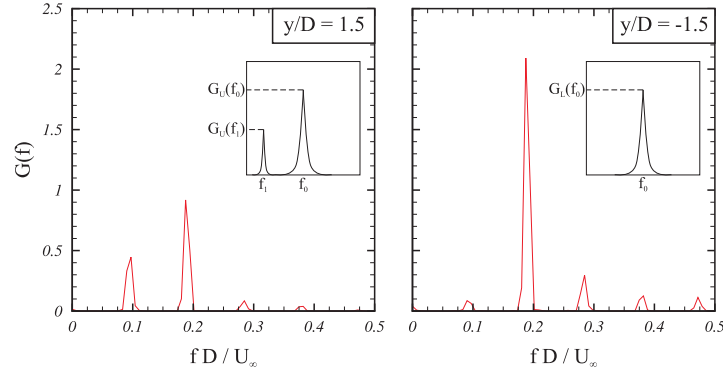
**Figure 4.9:** *Comparison of velocity spectrum of upper ($y/D = 1.5$) and lower ($y/D = -1.5$) halves of the wake. $Re = 180$. The streamwise coordinate of the data point is $x/D = 4.5$.*

surements. Reynolds number is $Re = 180$ and the measurement plane is located at $x_l/D = 4.5$. The transverse coordinate of the data probe is $y/D = 1.5$. The spanwise coordinate changed from *(a)* to *(e)* in Figure 4.8 to evaluate the effect of spanwise location. The horizontal frequency axis is non-dimensionalized so that it represents the Strouhal number $St = fD/U_\infty$.

A clear peak at the von Kármán vortex shedding frequency, $f_0 \approx 0.19$, is seen in all spectra. It is evident from graphs *(a)*, *(c)* and *(e)* that there is a second frequency component, $f_1 \approx 0.09$, at almost half of the shedding frequency. The signals which have sharp peaks at $f_1$ in their spectra belong to the data probe locations that are halfway between the two secondary vortices. In conjunction with the discussion of velocity characteristics, the secondary frequency component $f_1$ can be thought as the reflection of the 'high peak-low peak' velocity profile of Figure 4.4 in the frequency domain. Therefore, it indicates that the period of the secondary vortices in Mode-C transition is twice the shedding period of von Kármán vortices, $T_{secondary} = 2T_{shed}$.

The effect of the vertical location of the data probe point on the spectral characteristics is demonstrated in Figure 4.9, which contains the two spectra from upper and lower halves of the wake. Both spectra show clear peaks at von Kármán shedding frequency but only upper spectra indicate a secondary subharmonic peak. The peak values of the spectrum at designated frequencies $f_0$ and $f_1$ are summarized in Table 4.1. It is evident that the frequency ratio of the primary and secondary frequencies is approximately equal to 2 for the upper half of the wake, see Equation 4.1.

$$\frac{f_0}{f_1} = \frac{0.1894}{0.0945} = 2.004 \tag{4.1}$$

Furthermore, the peaks in the spectrum provides information about the energy content of the signal at corresponding frequencies. It looks like the corresponding

| $y/D = 1.5$ | | | | $y/D = -1.5$ | | | |
|---|---|---|---|---|---|---|---|
| $f_0 D/U_\infty$ | $G_U(f_0)$ | $f_1 D/U_\infty$ | $G_U(f_1)$ | $f_0 D/U_\infty$ | $G_L(f_0)$ | $f_1 D/U_\infty$ | $G_L(f_1)$ |
| 0.1894 | 1.034 | 0.0945 | 0.5439 | 0.1894 | 2.366 | - | - |

**Table 4.1:** *Peak values in velocity spectra shown in Figure 4.9.*

| Non-wired experiments | | Wired experiments | | |
|---|---|---|---|---|
| Re | St | Re | St | Difference |
| 100 | 0.173 | 100 | 0.163 | -5.7 % |
| 185 | 0.190 | 180 | 0.188 | -1.1 % |
| 200 | 0.201 | 195 | 0.189 | -6.3 % |
| 215 | 0.198 | 210 | 0.193 | -2.6 % |
| 230 | 0.205 | 225 | 0.192 | -6.3 % |
| 250 | 0.195 | 244 | 0.195 | 0.0 % |

**Table 4.2:** *Strouhal number values obtained from side-view experiments. Difference shows the percent reduction due to wire.*

energy content of the lower wake signal is approximately twice of the upper wake at this frequency:

$$\frac{G_U(f_0)}{G_L(f_0)} = \frac{1.034}{2.366} \approx 0.437 \qquad (4.2)$$

In flow visualization experiments there are no secondary vortices other than small scale vortex loops originating from the lower part of the cylinder, see Figure 4.1, and there is not a sharp peak at the secondary frequency in the power spectra of the velocity signal too, see Figure 4.9 (right panel). Therefore one can assume that all the contribution to the energy in the lower half of the wake comes from von Kármán vortices. However in the upper half of the wake there is also the contribution of secondary vortices. Therefore, the rough estimation for the ratio of the energy content of the two halves of the wake can be found as:

$$\frac{G_U(f_0) + G_U(f_1)}{G_L(f_0)} = \frac{1.034 + 0.5439}{2.366} \approx 0.667 \qquad (4.3)$$

### 4.2.3  Shedding frequency

The vortex shedding frequency in Mode-C transition is calculated by determining the corresponding peaks in the power spectra of different experiments. Figure 4.10 shows the Strouhal number values at different Reynolds numbers. The results were plotted using the values of Mode-A and Mode-B transition which were reproduced from Williamson [11] for comparison. Figure 4.10a shows the scatter of $St$ values of
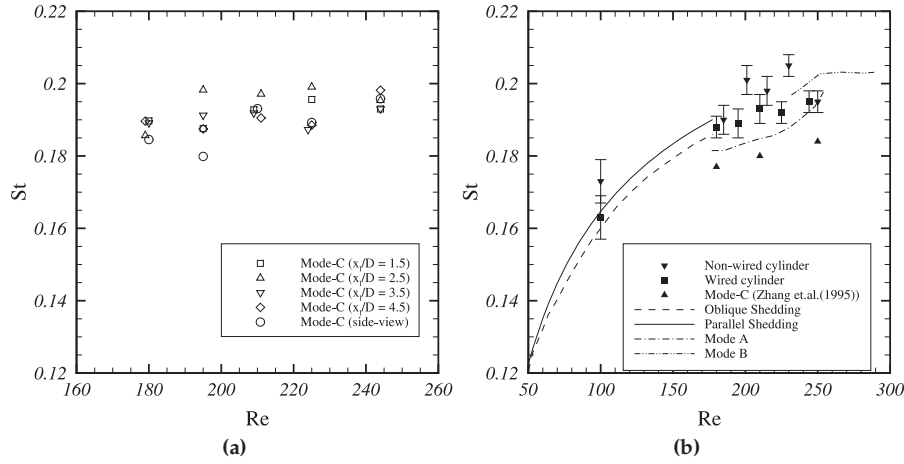
**Figure** 4.10: *Comparison of Re-St relationship for single cylinder and wired cylinder. The data for parallel shedding, oblique shedding, Mode-A and Mode-B are reproduced from Williamson [11]. St number for Mode-C transition is obtained from back-view and side-view PIV measurements. a) Scatter of St numbers of different Mode-C experiments, b) Comparison of non-wired and averaged St numbers of wired experiments with literature values. Error bars indicate frequency resolution of each corresponding spectrum.*

different experiments for Mode-C transition. The Strouhal numbers of the Mode-C transition are calculated by simply averaging the values at the corresponding Reynolds number and the results are shown in Figure 4.10b.

Figure 4.10b shows the comparison of non-wired and wired experiments with literature values. It is obvious that there is a deviation in measured Strouhal numbers for the non-wired case. The order of magnitude of this deviation is also the same for wired cylinder when the literature values of Zhang et al. [13] and measurements are compared. Despite this deviation from literature, the experimental data is consistent within itself and with the trend in literature, showing that there is shedding frequency reduction is Mode-C transition. The reduction in shedding frequency is of the order of a few percent, as summarized in Table 4.2.

Therefore, one may conclude that the trend of Mode-C experiments is in good agreement with values of Zhang et al. [13]. Apparently the wire changes the frequency characteristics of von Kármán vortices and it is likely that it suppresses the instability mechanisms that cause the discontinuities in the $St - Re$ graph for the non-wired cylinder flow.
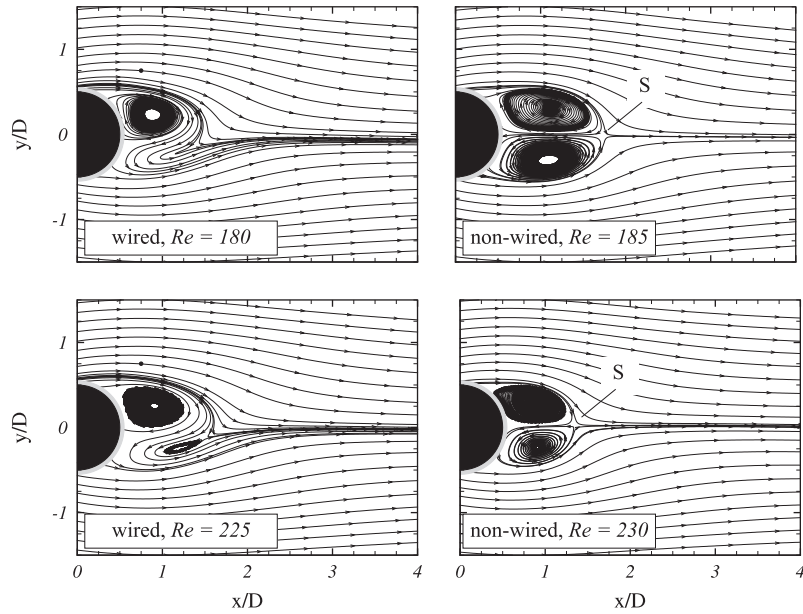
**Figure** 4.11: *Time-averaged streamlines in the near-wake of the cylinder.*

### 4.2.4   Breaking of symmetry

Placing a wire in the near-wake of a cylinder obviously acts as a symmetry breaking mechanism in the wake structure. This is evident in Figure 4.11 where the time-averaged streamline topology $\overline{\Psi}$ for two Reynolds numbers is given. The streamline are calculated using the time-averaged velocity components $\overline{u}$ and $\overline{v}$.

The $\overline{\Psi}$ patterns for the non-wired case indicate two symmetric swirl patterns in the near-wake for both Reynolds numbers. In figure it is clear that the size of these swirl patterns is decreasing with increasing Reynolds number. There is also a saddle point $S$ which is located at the wake centerline at the downstream edge of the swirl patterns. The location of the saddle point actually corresponds to the most downstream point of the recirculation region.

In the wired cases, the two-symmetric-swirl-pattern topology is not seen any more. For both $Re = 180$, the upper swirl region appears with a smaller size than its non-wired ($Re = 185$) counterpart. The same topology is seen for $Re = 225$ but with a swirl region slightly larger size than non-wired ($Re = 230$) case. Another difference is that for the wired cases there is no apparent saddle point to identify. However, the major difference is in the lower part of the wake where there is not a clear time-averaged swirl pattern. It appears for the wired case that the upper swirl region is related to the diverted vorticity which extends beyond wake centerline and smears the vorticity concentration of the lower shear layer. This mechanism seem

**(a)** *Mode-A*        **(b)** *Mode-B*

**Figure 4.12:** *Time variation of the streamwise vorticity on the line $x/D = 4.5$ from back-view PIV experiments of the non-wired cylinder wake at $Re = 185$ and $Re = 215$ for Mode-A and Mode-B, respectively. The time axis is non-dimensionalized with the corresponding shedding periods.*

to prevent the formation of lower time-averaged swirl pattern during the Mode-C transition.

The effect of the symmetry breaking effect of the wire can also be seen by comparing Figures 4.12 and 4.13, which represent the symmetry characteristics of non-wired and wired cylinder wake, respectively. Both figures shows the streamwise vorticity which is evaluated in time along a vertical cross-stream line placed at downstream location of $x/D = 4.5$ in the corresponding experiments. The vertical line is placed at the position of secondary vortices so that $\omega_x$ is tracked easily. The data is obtained from back-view PIV experiments using the configuration shown in Figure 2.4c.

Figure 4.12 shows the symmetry characteristics of the non-wired cylinder wake in transition regime associated with Mode-A and Mode-B at $Re = 185$ and $Re = 215$, respectively. The symmetry nature of the Mode-A wake is clearly seen in Figure 4.12a. The positive and negative vorticity appear in a symmetric manner with a period of $T_{shed}$. From the color contrast of the figure one can also conclude that both the upper and lower streamwise vortices have almost equal vorticity content. Hence, Mode-A can be characterized by

$$\omega_x(x, y, z, t) = -\omega_x(x, -y, z, t + T/2) \tag{4.4}$$

The symmetry of Mode-B can be observed in Figure 4.12b. The spanwise vorticity in Mode-B has the same sign on both sides of the wake during the vortex shedding cycle. The Mode-B is also T-periodic. Hence, Mode-B is characterized by

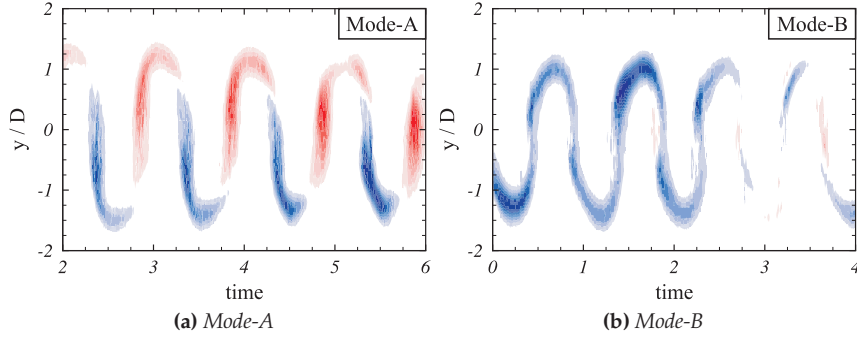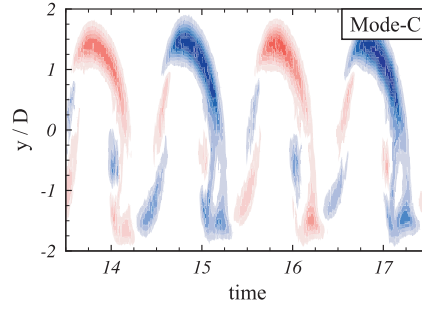$$\omega_x(x, y, z, t) = \omega_x(x, -y, z, t + T/2) \tag{4.5}$$

**Figure 4.13:** *Time variation of the streamwise vorticity on the line $x/D = 4.5$ from back-view PIV experiments of the Mode-C wake at $Re = 180$. Time axis is non-dimensionalized with the corresponding shedding period.*

However, Figure 4.13 clearly demonstrates that the wake undergoing a Mode-C transition is not symmetric with respect to the wake centerline and the vorticity field is 2T-periodic, unlike Mode-A and Mode-B. Actually the streamwise vorticity patterns change sign at every shedding period. In Mode-C transition the temporal symmetry of streamwise vorticity can be therefore described by

$$\omega_x(x, y, z, t) = -\omega_x(x, y, z, t + T) \tag{4.6}$$

## 4.3   Vorticity patterns in the near-wake

### 4.3.1   Spanwise vorticity

Figure 4.14 shows spanwise vorticity evolution in the near-wake of the cylinder through two shedding periods for the Reynolds number $Re = 180$. It demonstrates the period-doubling nature of Mode-C using the instantaneous spanwise vorticity $\omega_z$ snapshots. The phase information of the vortex shedding is obtained from the time signal of the vertical velocity component at point $(x/D, y/D) = (4.5, 1.5)$.

The image sequence starts with Figure 4.14a which corresponds to the phase at which upper vortex $UV_1$ is shedding. $UV_1$ is stretched and has two long vorticity braids. Meanwhile, the lower vortex $LV_1$ has a rather circular shape and is rolling-up across the wake to cut the vorticity supply of $UV_1$. At this stage, the negative vorticity from the upper shear layer is directed into the base region. This accumulated vorticity later forms the subsequent upper vortex $UV_2$, indicated by an arrow in Figure 4.14b.

Figure 4.14c shows the vorticity patterns one shedding cycle after Figure 4.14a. Despite the similarities of major vortical structures, some differences are still noticeable. Firstly, the upper vortex $UV_2$ does not have long vorticity braids and is more compact than preceding vortex $UV_1$. Secondly, the lower vortex $LV_2$ has a rather

elliptic shape compared to $LV_1$. Finally, after the comparison of the snapshots (a) and (c), it looks like the vorticity accumulation of the following upper vortex $UV_3$ uses wider space in the base region than the preceding $UV_2$. At phase $t = 3T_{shed}/2$, the upper vortex $UV_3$ shows a clear vorticity concentration at around $x/D \approx 1.75$ with stretched vorticity braids around it. In this sense $UV_3$ differs from its predecessor $UV_2$ which shows a vorticity spreading during the development stage, Figure 4.14b. These observations show that formation of primary von Kármán vortices in the Mode-C wake is not T-periodic but 2T-periodic, as evidenced in Figure 4.14a, Figure 4.14c and Figure 4.14e for upper vortices $UV_1$, $UV_2$ and $UV_3$, respectively.

### 4.3.2 Streamwise vorticity

To understand the temporal characteristics of the secondary vortices instantaneous patterns of streamwise vorticity $\omega_x$ at cross-stream planes $x_l/D = 1.5$ and $x_l/D = 2.5$ are shown in Figure 4.15 along with the corresponding von Kármán vortex shedding states for three independent experiments. The link between them is the phase relationship obtained from the vertical velocity signals at the intersection line of the two perpendicular planes, namely $XY - plane$ and $YZ - plane$.

It is evident from the vorticity concentrations in the cross-stream planes that the secondary vortices are present in the wake and that they originate from the very near-wake of the cylinder. During the formation of the upper vortex at the phase $t = 0$, there are two arrays of concentrated $\omega_x$ in the $x_l/D = 1.5$ plane. These vorticity arrays are aligned with the upper and lower shoulders of the cylinder and are out-of-phase with each other. Due to the stretching in the braid shear region where the vorticity content of the secondary is amplified, Mode-C vortices are more clear in the $x_l/D = 2.5$ plane. The same vorticity structure is seen after $2T_{shed}$ in Figure 4.15e. At the phase $t = T_{shed}$, similar vorticity arrays are seen but negative and positive vorticity structures interchange place. The 2T-periodic nature of the secondary vortices is apparent in the comparison of the vortex arrays at the phases $t = 0, T_{shed}$ and $2T_{shed}$. The wake state at $t = 0$ is out-of-phase with the $t = T_{shed}$ state and in-phase with the $t = 2T_{shed}$ state.

## 4.4 Development of period-doubling in Mode-C transition

### 4.4.1 Time evolution of Mode-C vortices

The formation process of Mode-C structures for a Reynolds number of $Re = 195$ throughout two shedding periods is illustrated in Figures 4.17 and 4.18, showing top-view and side-view flow visualization sequences, respectively. The snapshots are synchronized qualitatively so that they represent the same vortex shedding phase
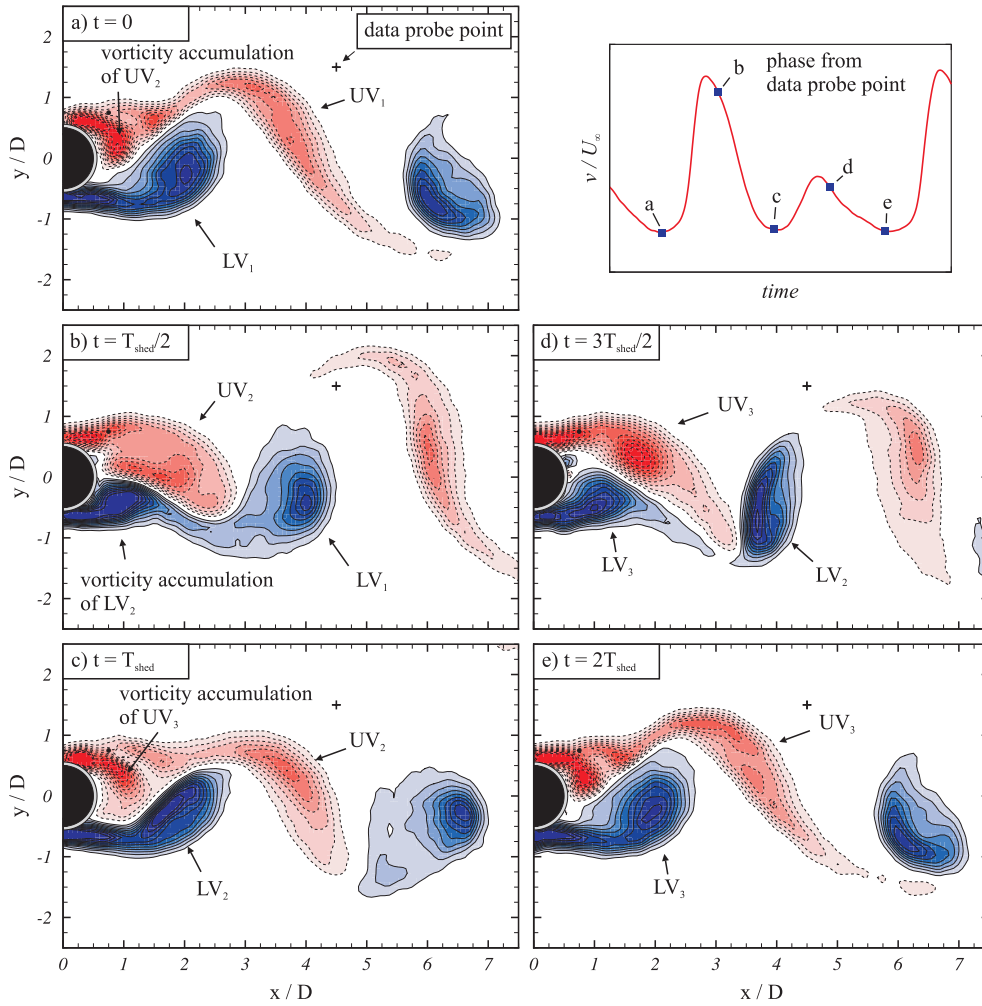
**Figure** 4.14: *Instantaneous non-dimensional spanwise vorticity patterns $\omega_z D/U_\infty$ in the near-wake of the cylinder. Contour levels are $|\omega_z|D/U_\infty = 0.4, 0.8, ..., 4$. Solid line and dashed line contours indicate positive and negative vorticity, respectively. Top-right figure shows the phases of vorticity fields with respect to the cross-stream velocity from the data probe point $(x/D, y/D) = (4.5, 1)$ at Reynolds number $Re = 180$.*
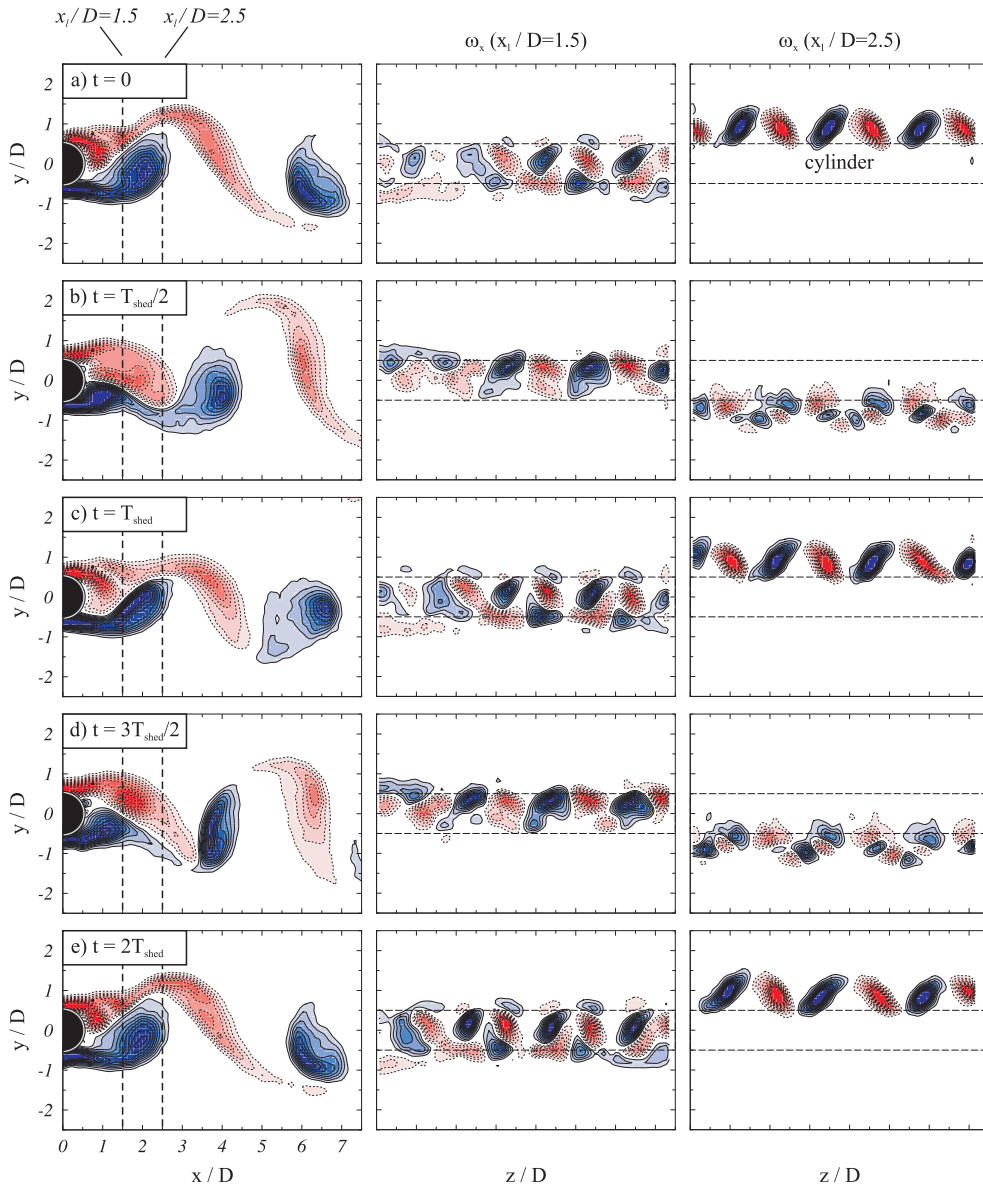
**Figure 4.15:** *Instantaneous patterns of non-dimensional streamwise vorticity $\omega_x D/U_\infty$ in the near-wake of the cylinder measured at cross-stream planes $x_l/D = 1.5$ (middle column) and $x_l/D = 2.5$ (right column) at corresponding von Kármán vortex shedding phases (left column). Contour levels are $|\omega_z|D/U_\infty = 0.4, 0.8, ..., 4$ and $|\omega_x|D/U_\infty = 0.2, 0.4, ..., 2$. Blue (solid line) and red (dashed line) contours indicate positive and negative vorticity, respectively, at $Re = 180$.*
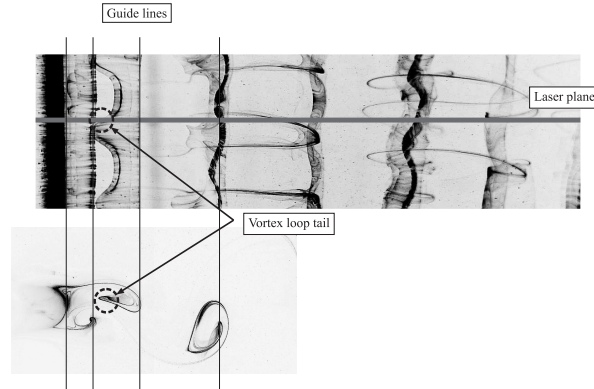
**Figure 4.16:** *Synchronization of two independent flow visualization experiments. In the top figure the probable location of the laser plane is shown. Guide lines are used to scale and synchronize the images.*

and lead to the reconstruction of the feedback mechanism of Mode-C shedding. The illustration of the synchronization procedure is presented in Figure 4.16. The main cylinder diameter $D$ is used as the reference length scale in the process. Firstly, the images from the side-view experiments are scaled down in order to make the cylinder diameter equal in both experiments. Secondly, guidelines are drawn from the vortex locations in the top-view images. Thirdly, the corresponding side-view image is determined using those guidelines for each top-view image. Finally, based on the location of the vortex loop tails, the probable location of the laser plane of side-view experiments is estimated in the top-view images.

The period-doubling nature of the process is illustrated in the phase diagram that is shown at the top-right corner of Figure 4.17. In this phase diagram, the letters correspond to the image numbers and indicate the vortex shedding phase. The initial image of the process, Figure 4.17a, is chosen such that it represents the approximate formation moment of the lower side von Kármán vortex, denoted as $L_1$. Likewise, the previously shed upper side von Kármán vortex is marked as $U_1$. This vortex $U_1$ shows spanwise waviness which is the signature of the vortex loops originating from the upper vortex. Figure 4.18a-d reveals that the vortex loops are parts of the upper vortex, which are torn from it and stay in the base region. Figures 4.18a-d also show that these vortex loops originating from the upper vortex stay between the upper and lower vortices effecting the near-wake dynamics. Moreover, these vortex loops are further stretched in the braid region, as seen in Figure 4.18c-d, and roll-up to form streamwise vortex pairs from the sides of the loops, as shown in Figures 4.17a-d. During this half shedding period, the vortex loop tails of $U_1$ stay at position of approximately $\sim 0.5-0.7D$ behind the cylinder, while the rest of the vortex move downstream.

The vortex loop tails of $U_1$, see Figure 4.18d, are apparently affecting the newly

forming upper von Kármán vortex $U_2$ by initiating a spanwise waviness at the initial formation stage, see Figure 4.17d. This wavy deformation in $U_2$ is amplified further in the recirculating region, see Figure 4.17d-g, and forms vortex loops that are seen in Figure 4.17g. These vortex loop tails of $U_2$ appear at the spanwise position of vortex loop heads of $U_1$ in the previous cycle. Therefore, Figure 4.18g does not show any sign of an emerging vortex loop, as the laser plane is located at the vortex loop head instead of a vortex loop tail.

In the first shedding period, the lower vortex $L_1$ has formed in a parallel way to the cylinder, see Figures 4.17a and b, and preserves its shape until its encounter with the vortex loop tails of $U_1$, as shown in Figure 4.17c. Afterwards, $L_1$ continues to shed in a slightly wavy pattern. However, despite this waviness, the lower vortex $L_1$ does not develop any vortex loops and hence streamwise vortex pairs. Its waviness is initiated after approximately $1/3$ periods, unlike for example the upper vortices $U_2$ and $U_3$ in which the waviness has started during the initial stages of formation.

The same physical process discussed above is also seen for the second part of the vortex shedding process in Figure 4.17g-m. The vortex loops of $U_2$ grow and form spanwise vortex structures which in turn initiate the formation of vortex loops in $U_3$. The vortex loop tails of $U_3$ appear at the spanwise position of vortex loop heads of $U_2$. Hence, the vortex loop tails of $U_1$ and $U_3$ occur at the same spanwise location, see Figures 4.17a and 4.17m, respectively. This type of occurrence effectively doubles the shedding period. Hence, the overall examination of the process suggests that the Mode-C instability is a self-sustaining process with a period of $T = 2T_{shed}$.

### 4.4.2   Feedback mechanism between von Kármán vortices

After the above discussion about the physical process of shedding, one may conclude that the period doubling is due to the feedback mechanism of streamwise vortices between two consequent upper vortices. In this section, this feedback process is discussed further using Figure 4.19. The figure shows three instants from Figure 4.17, each half shedding period apart from each other and each zoomed in to the near-wake.

The growth of the spanwise waviness and formation of vortex loops can be illustrated as if a vortex line is torn from the primary von Kármán vortex and left to deform and stretch. The left sketch of Figure 4.19 exhibits the *vortex loop 1* originating from previously shed upper vortex $U_1$ extending up to the cylinder. As shown in Figure 4.18d, *vortex loop 1* lies in between the upper and lower vortices. The upstream convection of the vortex line, i.e. *vortex loop 1*, has different effects on the primary vortices $L_1$ and $U_2$.

Firstly, the tails of *vortex loop 1* induce negative horizontal velocity on the lower vortex $L_1$ via Biot-Savart induction, as illustrated in Figure 4.19. This perturbation makes the segments of $L_1$, which face the tails of *vortex loop 1*, move slower than the neighboring segments causing a wavy pattern along the lower vortex $L_1$. The slow
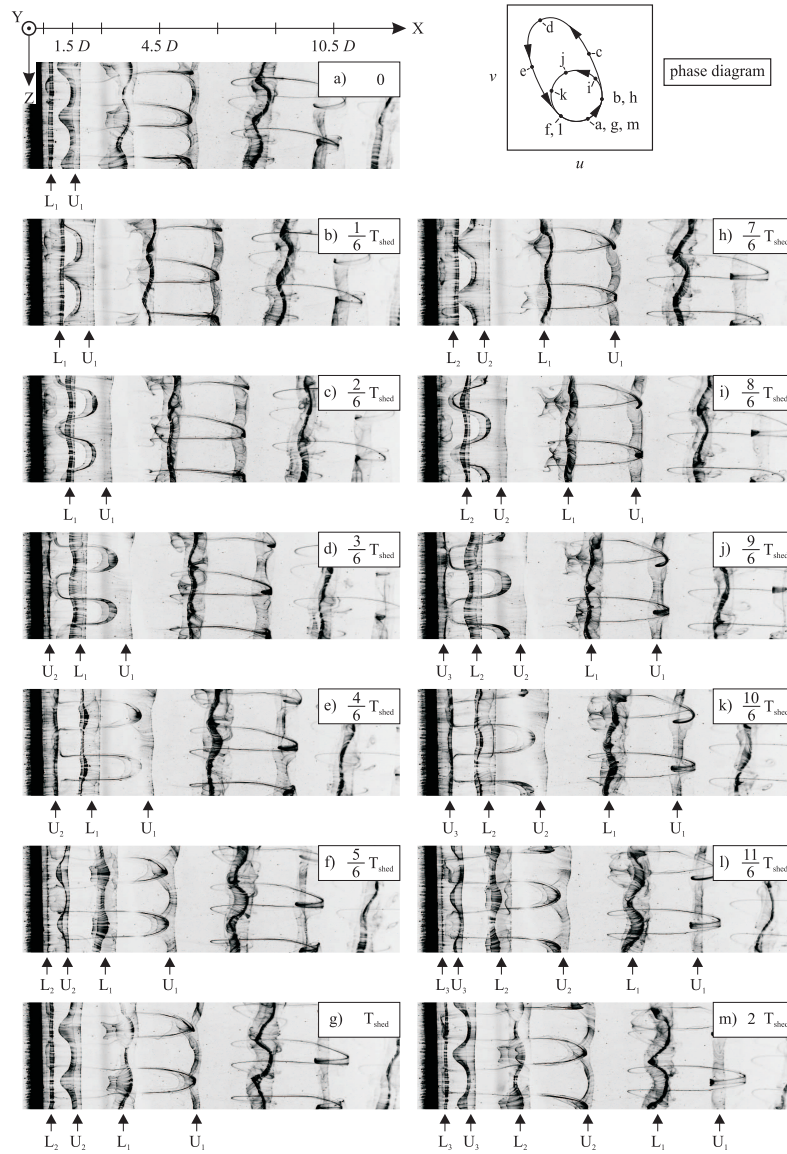
**Figure 4.17:** *Formation and evolution of Mode-C structures in the wake of a wire disturbed circular cylinder wake at Reynolds number of $Re = 195$. Letters U and L indicate the upper side and lower side primary von Kármán vortices, respectively, and subscripts show the indices of the corresponding vortices. Upper right diagram represents the vortex shedding cycles to which the representing images belong.*
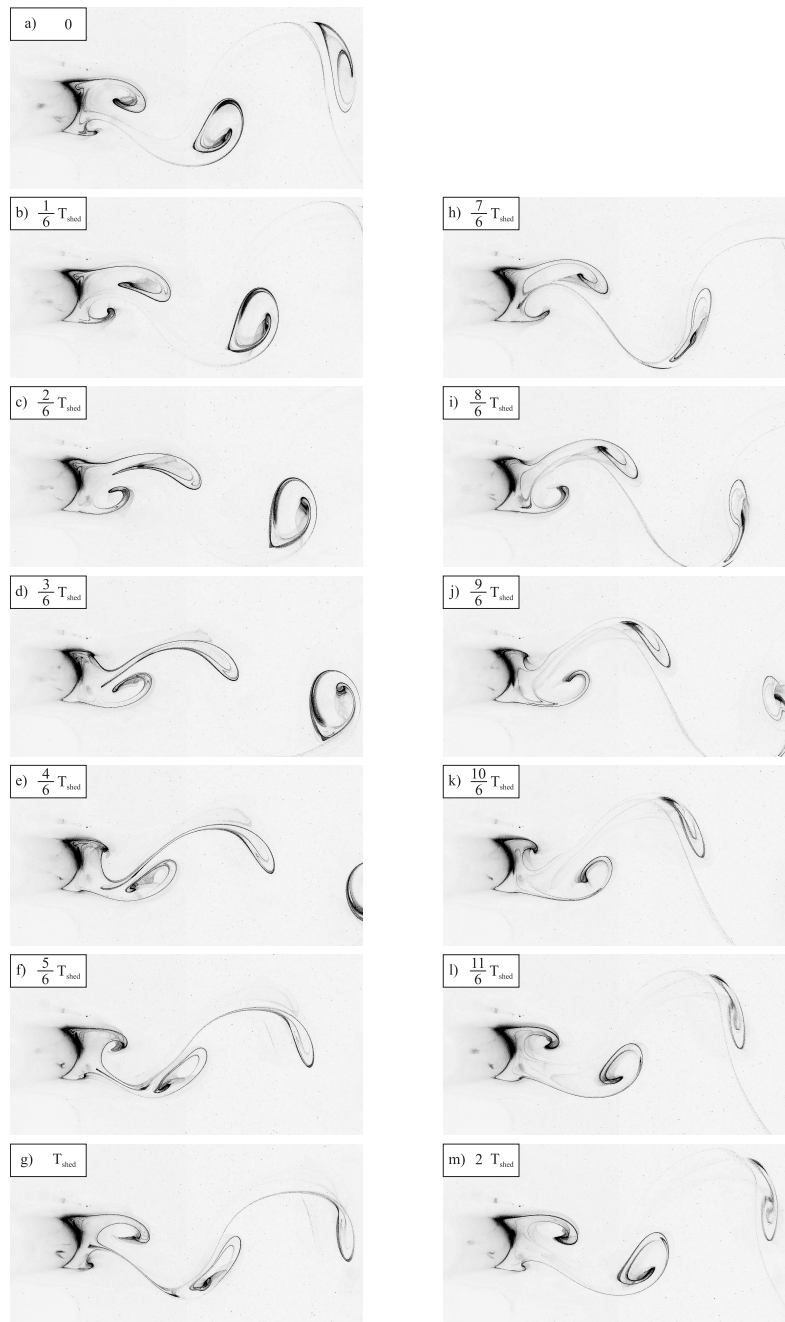
**Figure 4.18:** *Side-view visualization snapshots showing the evolution of Mode-C structures at Reynolds number of $Re = 195$. The snapshots represent approximately the same vortex shedding phase as in Figure 4.17*
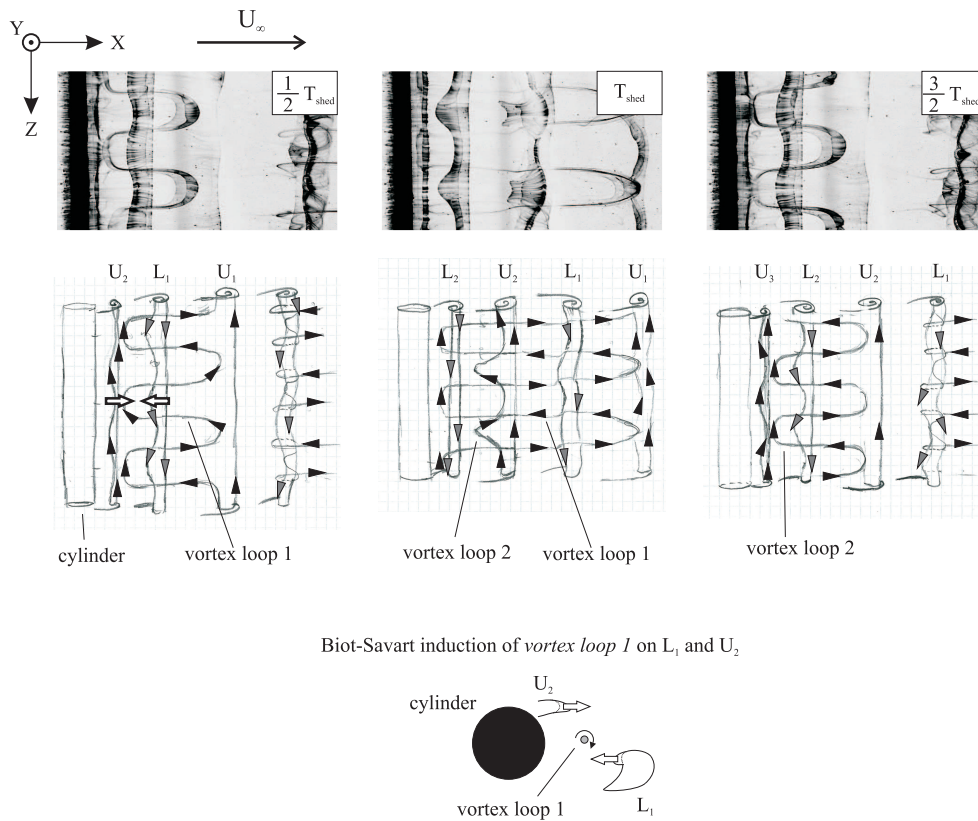
**Figure 4.19:** *Sketches of the feedback mechanism of Mode-C vortex formation. The vortex line sketches are presented with the corresponding flow visualization snapshots at Reynolds number of $Re = 195$. The flow visualization snapshots are zoomed into the formation region to make the near-wake vortex structures clear.*

moving segments are at the same spanwise position with the perturbation source, i.e. tails of *vortex loop 1*.

The second effect is on the newly forming upper vortex $U_2$. The tails of *vortex loop 1* has already extended up to the cylinder where it apparently effects the formation of $U_2$ at the initial formation stage by inducing a positive horizontal velocity perturbation, see the illustration in Figure 4.19. Due to this perturbation, the segments of $U_2$ move slightly faster at the position of the vortex loop tails of $U_1$. The segments which are between the vortex loop tails move slowly and at the later stage form the new tails of *vortex loop 2*, as shown in the middle sketch of Figure 4.19. At the later stage of the vortex shedding, the sides of the vortex loops will roll-up and form a streamwise vortex array of Mode-C instability.

The middle sketch of Figure 4.19 also represents the effects of the vortex loops on the formation of lower vortex $L_2$. Although the vortex loops of $U_1$ are still present in the near-wake, they don't affect the $L_2$ at its initial formation stage. Considering that approximately 1.5 shedding periods has passed since the formation of *vortex loop 1*, it is likely that they are not strong enough to do so. The waviness of $L_2$ is initiated when it meets the tails of the following *vortex loop 2*, as presented in the right sketch of Figure 4.19.

As discussed by Williamson [11], during the natural transition regime Mode-A, the feedback mechanism is set between the consecutive primary vortices and this mechanism is the reason of self-sustaining Mode-A vortex loops at the same spanwise position. On the other hand, for the Mode-C case, it is shown that the vortex loops of $U_2$ are not close enough to induce a perturbation on $L_2$ at the initial stage of the formation process. $L_2$ sheds parallel to the cylinder and does not show any spanwise waviness until it encounters the vortex loops of $U_2$. This encounter takes place when it is too late for the lower vortex to generate strong enough vortex loops within the next half-cycle. So, $L_2$ can not override the effect of *vortex loop 2* on $U_3$. This process breaks the natural feedback mechanism of two consecutive primary vortices (lower and upper) in Mode-C transition and establishes a new feedback mechanism which is apparently between the consecutive upper vortices only.

## 4.5   Concluding remarks

The major consequence of placing a wire in the near-wake of a cylinder is the replacement of Mode-A and Mode-B transitions with Mode-C transition. After careful examination of flow visualization images at $Re > 180$, Mode-C structures are found to have a spanwise wavelength of $\lambda_z \approx 2D$ and to appear at the same spanwise location at every two shedding periods instead of one. Hence, the Mode-C transition has a period-doubling character which shows itself as a shift in spanwise position of Mode-C vortices in every cycle.

The investigation of velocity-time signals which are obtained from PIV experi-

ments revealed that they contain a W-shaped 'high-peak-low-peak' velocity profile. The reason of having this velocity profile is that secondary vortices change sign every shedding period. Due to this type of velocity profile the $u - v$ phase plot shows two phase cycles instead of one, indicating a period-doubling nature of the velocity signal.

Spectrum analysis showed that the 'high-peak-low-peak' velocity profile is reflected as a subharmonic frequency component in the frequency domain. Naturally, this subharmonic component is associated with the secondary Mode-C vortices, while the primary frequency peak is associated with von Kármán vortices. A rough estimate of the wake energy from the spectrum indicates that there could be an energy transfer from the primary vortices to the secondary vortices in the upper shear layer (the topic of the next chapter). Primary frequency peaks in the spectrum denote the corresponding Strouhal numbers of Mode-C transition. In the experiments, when compared with Mode-A and Mode-B transition, the Strouhal numbers for Mode-C are slightly lower than Mode-A and Mode-B. Unlike the non-wired case, wired cylinder transition does not show any discontinuities in the $Re - St$ graph.

Investigation of both symmetry characteristics and instantaneous vorticity patterns showed that the Mode-C transition is 2T-periodic rather than T-periodic. An analysis of the time evolution of the streamwise vorticity field revealed that the period of formation of von Kármán vortices do not change. However, due to the interaction with secondary vortices their formation cycle show a 2T-periodic nature. That is, two shedding periods have to pass to have the same von Kármán vortex at the same location. Despite their T-periodic nature, the interaction mechanism of upper and lower vortices during formation changes every period. The 2T-periodic nature of the Mode-C wake is clearer when the time evolution of secondary vortices is analyzed. The streamwise vorticity and rotation direction of the secondary vortices change sign every shedding period causing the whole unsteady wake to become 2T-periodic.

The secondary vortices in Mode-C transition are actually the vortex loops that originate from the upper vortex. These vortex loops are further stretched in the braid region and roll-up to form streamwise vortex pairs from the sides of the loops. They are located between the upper and lower vortices and affect the near-wake vortex shedding process.

A detailed investigation of flow visualization images showed that Mode-C instability exhibits feedback of streamwise vortices between the upper primary vortices only. This works in such a way that vortex loops are generated at the same spanwise position in every two cycles. Therefore, it is concluded that the period doubling appears in this type of flow due to the feedback mechanism that appears between two upper vortices.

# Energy contents and vortex dynamics in Mode-C for $Re \geq 180$

## 5.1 Introduction

Several experimental studies have been performed to characterize the secondary vortices in the circular cylinder wake [11, 70–73]. Williamson [11] reported results obtained from hot-wire measurements in the transition regime $Re > 180$, while Lin et al. [70] and Chyu and Rockwell [71] measured the secondary vortices in a cross-stream plane using PIV at a Reynolds number of $Re = 10000$ (in the turbulent flow regime). Huang et al. [72] also performed PIV experiments to measure secondary vortices in all three perpendicular cartesian planes. In recent work, Scarano and Poelma [73] performed time-resolved tomographic PIV experiments in the Reynolds number range of $Re = 180 - 5540$. All these experiments focused on non-wired cylinders.

Regarding the wired cylinder case, it is previously shown in Chapter 4 that Mode-C transition in a wired cylinder wake at $Re = 180 - 244$ can be characterized by the formation of secondary vortices with a period-doubling nature. It is also shown that the shedding frequency in Mode-C transition is lower than the Mode-A and Mode-B frequencies for the non-wired cylinder in the same Reynolds number range. This chapter mainly focuses on further experimental characterization of Mode-C transition regarding the fluctuating flow features, energy characteristics and vortex dynamics using the set-up and experimental techniques discussed earlier.

The experimental data is obtained from side-view and back-view PIV measurements in the Reynolds number range of $Re = 180 - 244$ for the wired case. The wire is again fixed at position $(x_w/D, y_w/D) = (0.75, 0.75)$. Additional side-view experiments in the Reynolds number range of $Re = 185 - 250$ are done for the non-wired case. The results of the non-wired experiments are used to asses the effect of the wire on various flow features.

First, the fluctuating velocity characteristics are examined to characterize the effect of the wire on the temporal behavior of the wake. The energy spectrum analysis in Chapter 4 showed that there might be an energy transfer from the primary vortices to the secondary vortices in the upper half of the wired cylinder wake. Secondly, this observation is further evaluated by calculating discrete energy components at different frequency components of the energy spectrum. Thirdly, the vortex dynamics in Mode-C transition is investigated. An assessment of the vortex strengths and trajectories of primary vortices is performed. Also, the strengths and spanwise wavelength of Mode-C vortices are calculated. Finally, the change in the Strouhal number, due to Mode-C, is discussed.

For completeness, it is mentioned here that all the results presented are determined from experiments. Due to the three-dimensional character of the flow, no numerical results are shown in this chapter.

## 5.2 Fluctuating velocity characteristics

The shedding frequency of a circular cylinder is closely related to its fluctuating velocity characteristics, such that, if these fluctuation are reduced below some level, even a vortex shedding suppression can be achieved. The importance of velocity fluctuations comes from the fact that the vortex shedding frequency depends on the enhancement or damping of velocity fluctuations in the wake [59]. The fluctuating wake flow is characterized by its velocity components' standard deviation from the mean value ($u_{rms}$). For the analysis only the streamwise component $u$ of the velocity field is used, since the dominating flow is in that direction.

$$u_{rms} = \sqrt{\frac{1}{N_f} \sum_{i=1}^{N_f} (u_i')^2} = \sqrt{\overline{(u')^2}} \tag{5.1}$$

with $u_i' = u_i - \overline{u}$ being the fluctuating velocity and $N_f$ number of data files. Here, $u_i$ is the instantaneous velocity and $\overline{u}$ is the mean velocity component which is calculated from:

$$\overline{u} = \frac{1}{N_f} \sum_{i=1}^{N_f} u_i \tag{5.2}$$

Figure 5.1 shows the non-dimensional rms-velocity profiles for the wired case at

**(a)** *wire:* $Re = 180$, *no wire:* $Re = 185$



**(b)** *wire:* $Re = 225$, *no wire:* $Re = 230$
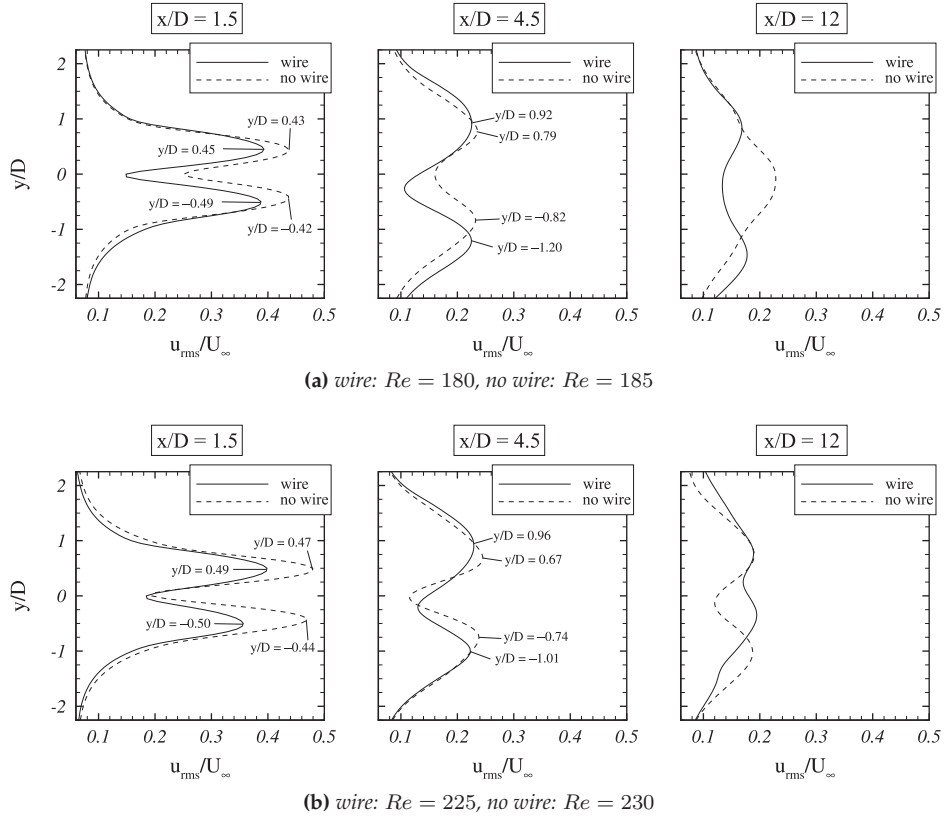
**Figure 5.1:** $u_{rms}/U_\infty$ *profiles in the near-wake at two different Reynolds numbers* ($Re = 185, 230$) *and three downstream positions* ($x/D = 1.5, 4.5, 12$).

| Non-wired experiments | | Wired experiments | | |
| --- | --- | --- | --- | --- |
| Re | $u_{rms}\|max/U_\infty$ | Re | $u_{rms}\|max/U_\infty$ | Difference |
| 185 | 0.446 | 180 | 0.400 | -10.3 % |
| 200 | 0.462 | 195 | 0.394 | -14.8 % |
| 215 | 0.472 | 210 | 0.408 | -13.6 % |
| 230 | 0.490 | 225 | 0.407 | -16.9 % |

**Table 5**.1: *Maximum $u_{rms}/U_\infty$ values of the upper shear layer at different Reynolds numbers and percentage difference between wired and non-wired experiments.*

two different Reynolds numbers and at three different downstream positions. The non-wired case is also plotted for comparison. The rms-velocity at $Re = 180$ for the wired case is presented in Figure 5.1a. For $x/D = 1.5$, both wired and non-wired cases exhibit similar curves with two peaks which are almost symmetric with respect to the wake centerline ($y/D = 0$). These two peaks are associated with the upper and lower vortex rows of the von Kármán vortex street. The locations of maximum $u_{rms}$ values are aligned with the upper and lower shoulder of the cylinder, indicating that the highest fluctuation values are achieved in the separating shear layer. At this downstream position, the effect of the wire is evident in reducing the rms-velocity levels.

On the other hand, at $x/D = 4.5$ the symmetry breaking effect of the wire is more apparent (see also Figure 4.11 in Chapter 4). The $u_{rms}/U_\infty$ profile in the upper half of the wake is broadened and its peak is slightly at a higher position when compared to the non-wired case. The $u_{rms}/U_\infty$ peak of the wired case in the lower half of the wake is at lower position than its non-wired counterpart. The damping effect of the wire is not seen anymore at this downstream position. This is evident from the comparison of the rms-velocity values of wired and non-wired cases.

At a higher Reynolds number $Re = 225$, the near-wake velocity fluctuation characteristics of Mode-C transition does not change much from the $Re = 180$ case. The shape of the $u_{rms}/U_\infty$ profile of the wired case has the same curve pattern as the non-wired cylinder case's profile. However, at $x/D = 1.5$, the reduction in the velocity fluctuation level is higher than in the $Re = 180$ case. The broadening of the upper wake $u_{rms}/U_\infty$ profile is also evident.

As seen in Figure 5.1 one of the major effects of the wire on the fluctuating velocity characteristics is reducing the rms-velocity levels in the shear layers in the vortex formation region. Another major effect is the introduction of an asymmetry to the $u_{rms}/U_\infty$ profiles. This effect is more pronounced at more downstream position, i.e. outside of formation region. This asymmetry exhibits itself as a broadening of the $u_{rms}/U_\infty$ profile in the upper half of the wake. This broadening of the profile might be an indication of a spread in the fluctuating velocity, possibly due to the vorticity braids originating from the upper vortices.
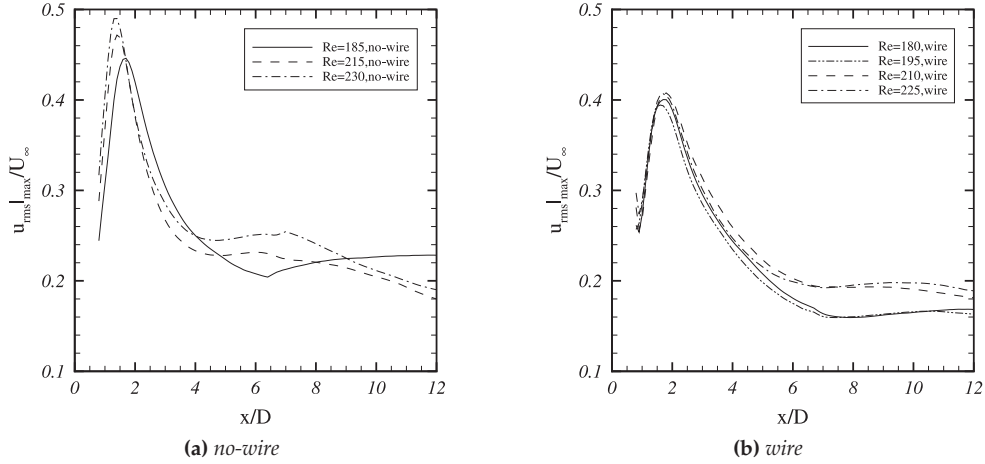
**(a)** *no-wire*  **(b)** *wire*

**Figure 5.2:** *Downstream variation of maximum levels of* $u_{rms}|_{max}/U_\infty$ *in the upper half of the wake.*

The damping effect of the wire on $u_{rms}/U_\infty$ values can be quantified by comparing the maximum values for the wired and non-wired cylinder wake at different Reynolds numbers. Figure 5.2 shows the downstream variation of maximum rms-velocity values $u_{rms}|_{max}/U_\infty$ in the upper separating shear layer of wired and non-wired cylinder wakes in the transition regime.

Figure 5.2 mainly demonstrates that $u_{rms}|_{max}/U_\infty$ levels do not change significantly in the wired cases. They stay almost constant throughout the Reynolds number range $Re = 180 - 225$. This indicates that in the near-wake the rms-velocity characteristics of Mode-C transition do not change. As summarized in Table 5.1, the wire reduces the $u_{rms}|_{max}/U_\infty$ levels by more than $10\%$ and this amount of reduction is increasing with Reynolds number, providing an almost constant fluctuation level in the upper shear layer during the Mode-C transition.

## 5.3 Energy content of the Mode-C wake

It is previously discussed in Chapter 4 that the energy spectrum in the Mode-C transition has predominant peaks at von Kármán vortex shedding frequency $f_0$ and at a subharmonic frequency $f_1$. The subharmonic frequency $f_1$ is associated with the formation of secondary vortices and points to the period-doubling character of the Mode-C transition. It is possible to calculate the energy content of Mode-C wake at particular frequencies by integrating the energy spectrum curve [4, 17, 68]. For that

purpose the energy intensity $e$ at a point in the flow field is defined as [4];

$$e = \frac{\int_{-\infty}^{+\infty} G(f)\mathrm{d}f}{U_\infty^2} = \frac{u_{rms}^2}{U_\infty^2} \tag{5.3}$$

with $G(f)$ defining the energy spectrum curve. This shows that $G(f)\mathrm{d}f$ is the energy in a frequency interval $\mathrm{d}f$ centered at $f$ [68]. If the boundaries of the integral cover a specific frequency interval in the spectrum then the integration is the discrete energy intensity in that frequency interval. Furthermore, the integration of the energy intensity across the wake gives the total integrated wake energy [17]:

$$E = \int_{-\infty}^{+\infty} e\,\mathrm{d}\left(\frac{y}{D}\right) = \int_{-\infty}^{+\infty} \left(\frac{u_{rms}}{U_\infty}\right)^2 \mathrm{d}\left(\frac{y}{D}\right) \tag{5.4}$$

There are two ways of calculating the energy intensity and integrated energy. The first way is to use the rms-velocity calculations and the second way is to use the spectrum calculations. Figure 5.4 shows the comparison of the wake energy intensity $e$ and the integrated energy $E$ obtained from rms-velocity and spectrum calculations of side-view PIV experiments. The energy intensity plots represent cross-stream data profiles for wired and non-wired cases at $x/D = 4.5$ for $Re = 180$ and $Re = 185$, respectively, while the integrated energy plot is for the wired case only. It is evident from Figure 5.4b that both approaches of calculating wake energy produce very close results. Therefore, it is concluded that spectrum analysis of PIV velocity data can be used for further characterization of the wake energy at discrete frequency components.

As demonstrated in Figure 5.3, the total energy intensity $e$ can be written as the sum of energy intensities at discrete frequencies [4].

$$e = e_0 + e_1 + e_h + e_n \tag{5.5}$$

where $e_0$ and $e_1$ are the energy intensities at vortex shedding frequency $f_0$ and subharmonic secondary frequency $f_1$, respectively. $e_h$ represents the contributions of harmonics of $f_0$ and $f_1$. $e_n$ includes the high frequency noise and the rest of fluctuation energies in the wake.

Figure 5.5a shows each discrete component that contributes to the energy of the wired cylinder wake during Mode-C transition. It demonstrates the cross-stream variation of $e_0$, $e_1$, $e_h$ and $e_n$ at downstream position of $x/D = 4.5$ for the wired case of $Re = 180$. The wake is dominated by the von Kármán vortex street which is reflected as two almost symmetrical peaks in the $e_0$ plot. The upper half of the $e_0$ curve has a wider shape with a lower peak value than the lower half of the curve. The effect of the wire is clearly evident in the plot of $e_1$ which shows a clear peak in the upper wake at position of $y/D = 1.25$. The position of this peak corresponds
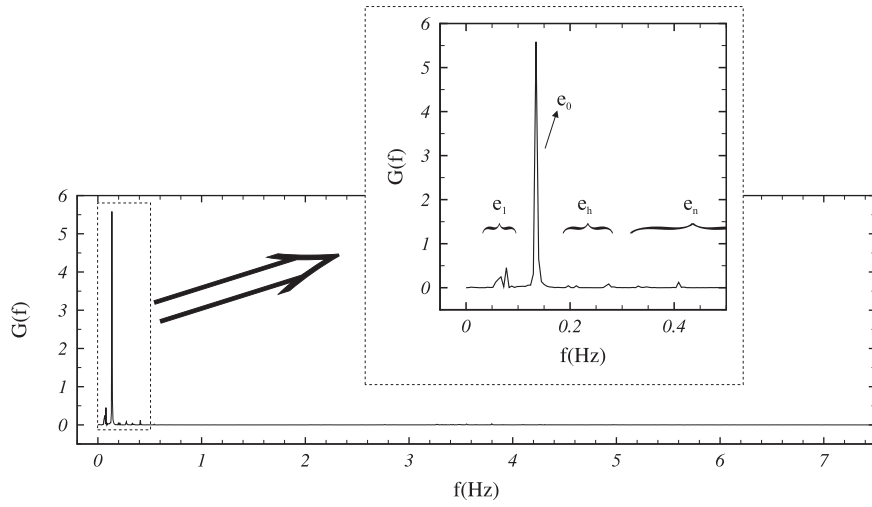
**Figure 5.3:** *Example of an energy spectrum and corresponding discrete energy intensities. Energy spectrum is obtained from side-view PIV experiment for $Re = 180$ at data point $(x/D, y/D) = (4.5, 1.0)$.*



**(a)** *energy intensity, e*

**(b)** *integrated energy, E*
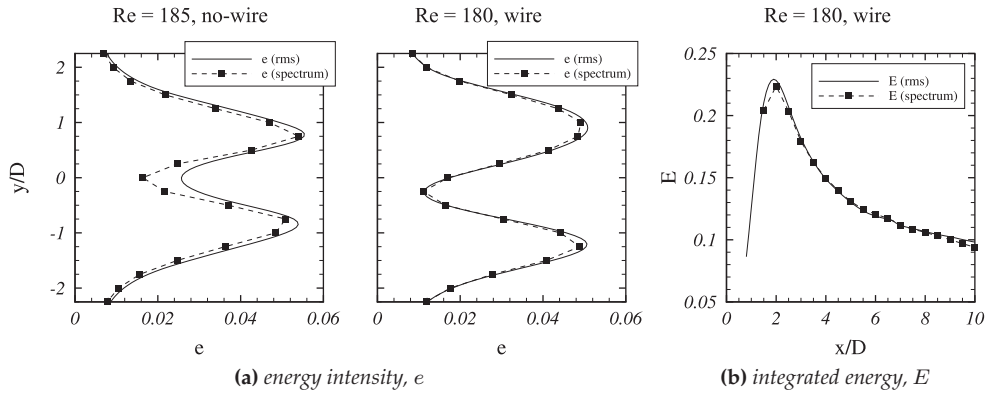
**Figure 5.4:** *Comparison of wake energy intensity and integrated energy obtained from rms and spectrum calculation of side-view PIV experiments. The energy intensity plots show cross-stream data profiles at $x/D = 4.5$.*

**Figure 5.5:** *Discrete energy components in Mode-C wake which are calculated at specific frequencies of the energy spectrum on the cross-stream line at $x/D = 4.5$.*

to the vortex centers of the secondary vortices as shown in Figure 5.6. $e_h$ contains the harmonics of the frequencies $f_0$ and $f_1$. It has a maximum value on the wake centerline since the wake centerline faces the influence of the von Kármán vortices from both sides of the wake causing a harmonic frequency of $2f_0$. On the other hand, as seen from the plot of $e_n$ the hi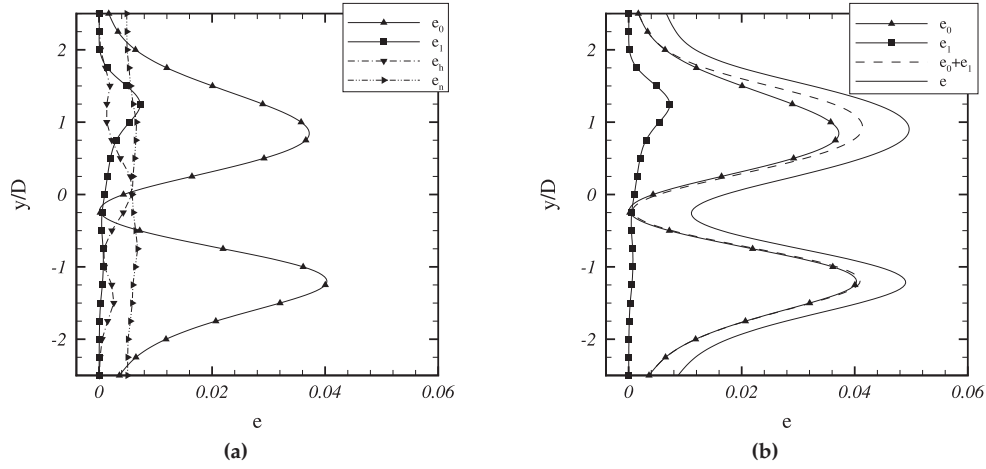gh frequency noise is constant across the wake. $e_n$ is calculated by taking the integral of Equation 5.3 for the frequencies $f > 2f_0$.

Having determined the energy intensities at specific frequencies, it is worth to further discuss the energy contents of the primary and secondary vortices, namely $e_0$ and $e_1$, and compare them with the total energy intensity for better understanding.

Figure 5.5b shows the comparison of the total energy intensity $e$ and the sum of energies at the primary and secondary frequencies $e_0 + e_1$. It is clear that the $e_0 + e_1$ follows the $e$ curve with an almost constant deviation which is due to the noise and higher harmonic contributions. The energy intensity $e_0$ at the von Kármán vortex shedding frequency in the upper half of the wake is less than the energy intensity in the lower half. It is obvious that the excess energy is stored in $e_1$ in the upper half of the wake. Thus, some portion of the energy at the von Kármán vortex shedding frequency $f_0$ is transferred to the subharmonic frequency $f_1$ in the upper half of the wake. This is due to the fact that the secondary vortices are originating from the upper von Kármán vortices only. Hence, there is no energy content at secondary frequency $f_1$, i.e. $e_1 \approx 0$, for $y/D < 0$.

Figure 5.7 demonstrates the variation of the integrated wake energy $E$ in the wake of a wired cylinder for Reynolds numbers $Re = 180$ and $Re = 225$ and for a non-wired cylinder for $Re = 185$. The downstream decay of the wake energy of
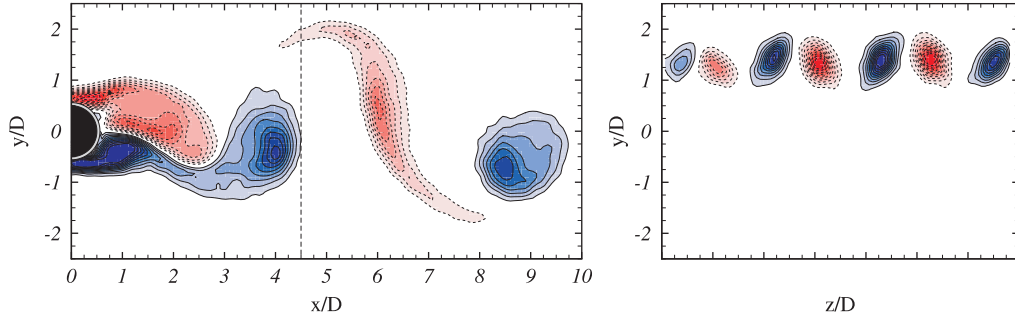
**Figure 5.6:** *Instantaneous pattern of non-dimensional spanwise $\omega_z D/U_\infty$ (left figure) and streamwise $\omega_x D/U_\infty$ (right figure) vorticity. Streamwise vorticity is measured at cross-stream plane $x/D = 4.5$ at the corresponding von Kármán vortex shedding phase in the left figure. Contour levels are $|\omega_z|D/U_\infty = 0.4, 0.8, ..., 4$ and $|\omega_x|D/U_\infty = 0.2, 0.4, ..., 2$. Blue (solid line) and red (dashed line) contours indicate positive and negative vorticity, respectively, at $Re = 180$.*
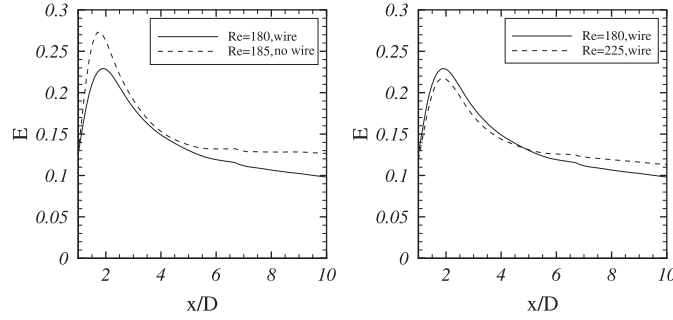


**Figure 5.7:** *Downstream variation of total wake energy $E$ for wired and non-wired cylinders.*
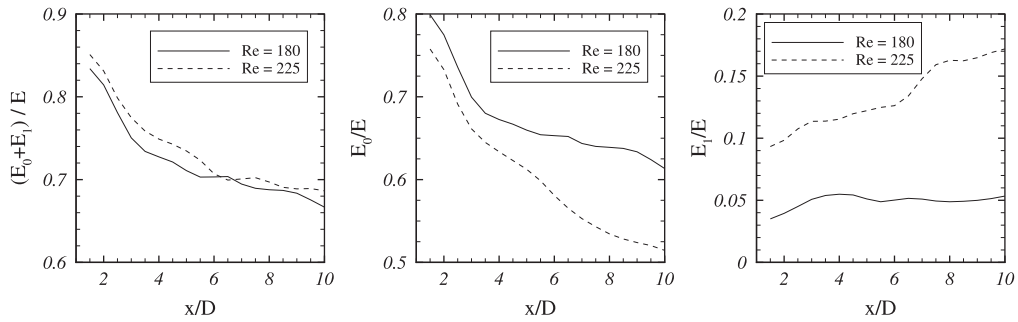


**Figure 5.8:** *Downstream variation of total $(E_0 + E_1)/E$ and discrete energy ratios $E_0/E$ and $E_1/E$ in the wake of a wired cylinder at $Re = 180$ and $Re = 225$.*

Mode-C shows an exponential behavior for $Re = 180$ while the non-wired cylinder wake exhibits a slower decay than Mode-C with a plateau for $x/D > 6$. The downstream decay of the wake energy of Mode-C also shows an exponential behavior for $Re = 225$. However, the decay rate seems to be slightly lower for $Re = 180$.

However, the discrete energy components show different behaviors, as shown in Figure 5.8. The downstream variation of the ratio of the sum of discrete energies to the total wake energy, $(E_0 + E_1)/E$, does not seem to change with the Reynolds number in the Mode-C transition regime. $E_0/E$ and $E_1/E$ are measures of the contribution of von Kármán vortices and secondary vortices to the total integrated energy. More than $50 - 60\%$ of the wake energy is coming from the von Kármán vortices but the percentage in the total energy is decreasing with increasing Reynolds number and downstream position. On the other hand, the percentage of the contribution of secondary vortices in the total energy is increasing both with Reynolds number and with downstream position. Thus, one may conclude that the von Kármán vortices die faster than the secondary Mode-C vortices.

## 5.4  Vortex strengths and trajectories

### 5.4.1  Spanwise vortices

The instantaneous spanwise vorticity $\omega_z D/U_\infty$ iso-contours obtained from side-view PIV experiments at different Reynolds numbers are shown in Figure 5.9. It demonstrates the vorticity structure at different stages of Mode-C transition. The images are chosen such that they more or less represent the same phase in the shedding cycle. The figure shows that the overall layout of the flow structure in Mode-C transition does not change with increasing Reynolds number in the range $180 \leq Re \leq 244$. The vorticity field for $Re = 244$ is not shown, however it shows the same flow features in a slightly more disordered manner.

The effect of the wire on the trajectories and strengths of von Kármán vortices in the transition regime $Re \geq 180$ is shown in Figure 5.10. The vortices are defined using the $\lambda_2$ method. The details of the method are summarized in Chapter 2. The boundary of a vortex is represented by a closed contour line of $\lambda_2 = -0.1$. The strengths and trajectories are calculated using Equations 2.13 and 2.14. The vortices are tracked in time for $6 - 10$ shedding periods. The tracking time is different for each experiment and is determined by the length of the 'high-peak-low-peak' characteristic of the reference velocity signal, see Chapter 4. The incomplete vortex trajectories in Figure 5.10 correspond either to the beginning or to the end of the tracking procedure.

The effect of the wire on the vortex trajectories is evident in Figure 5.10. There are two different trajectories for both upper and lower vortices. They are denoted in the uppermost left plot of Figure 5.10. $UT_1$ and $UT_2$ point out the trajectories of
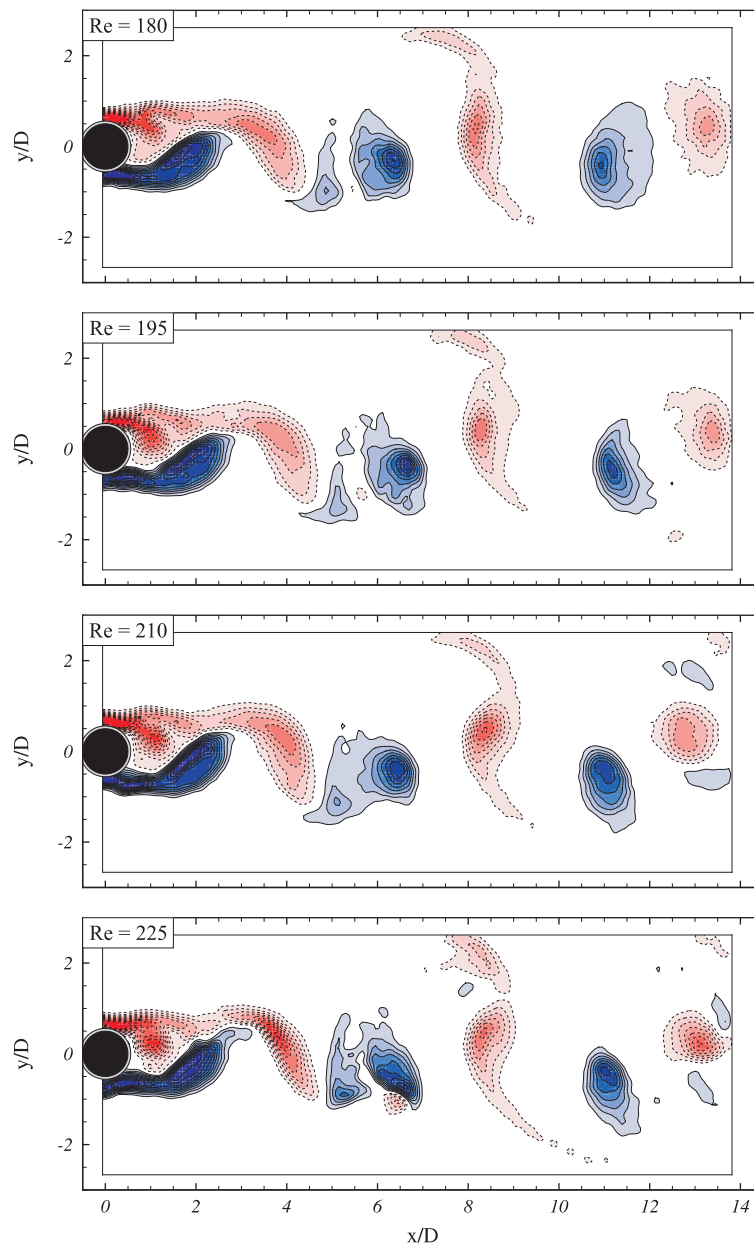
**Figure 5.9:** *Instantaneous non-dimensional spanwise vorticity patterns $\omega_z D/U_\infty$ in the wake of the wired cylinder. Contour levels are $|\omega_z|D/U_\infty = 0.4, 0.8, ..., 4$. Solid line and dashed line contours indicate positive and negative vorticity respectively.*
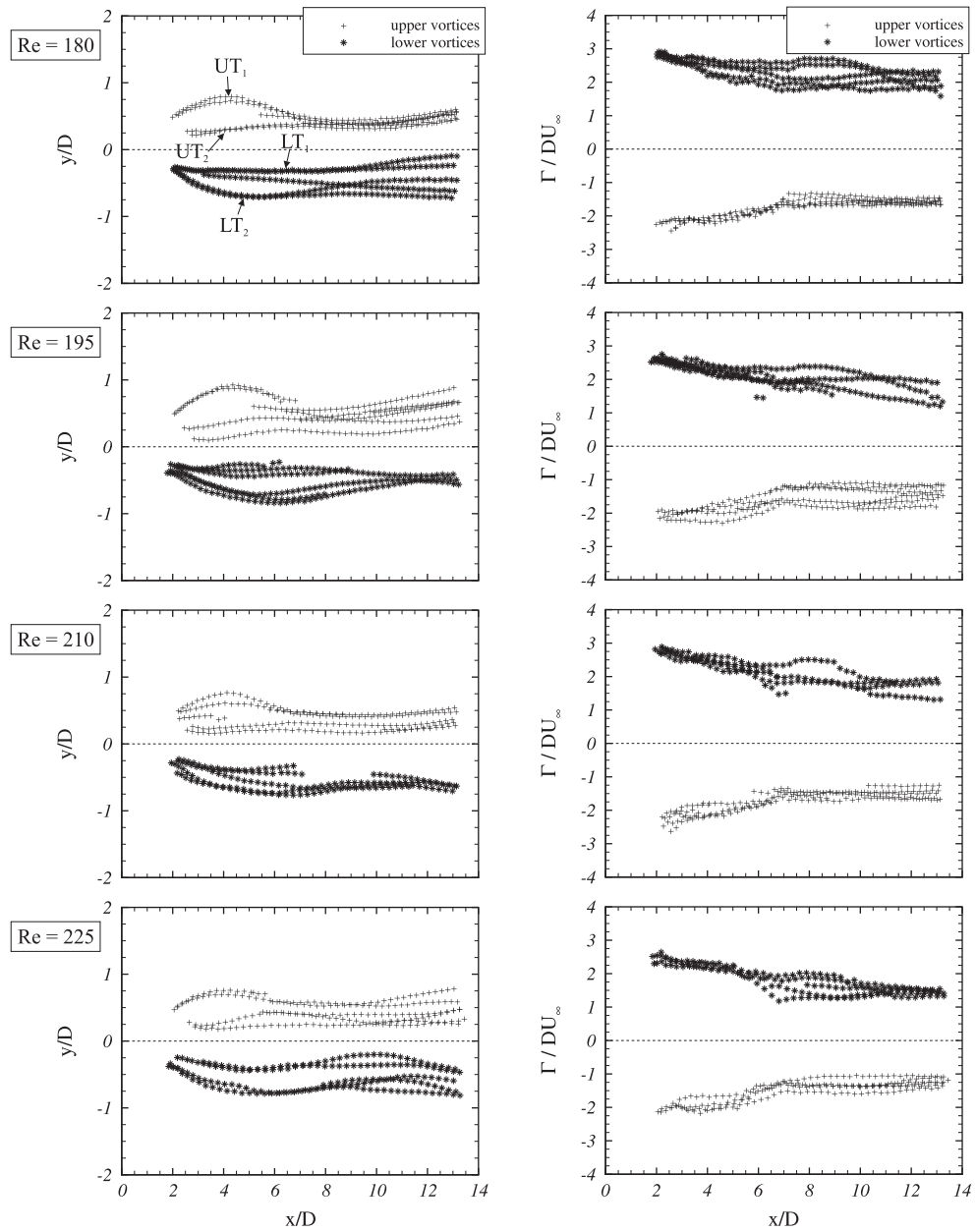
**Figure 5.10:** *Vortex trajectories and strengths of von Kármán vortices in the wake of a wired cylinder as a function of Reynolds number. ($UT_1, UT_2$: trajectories of upper vortices, $LT_1, LT_2$: trajectories of lower vortices).*

upper vortices and $LT_1$ and $LT_2$ the trajectories of the lower vortices. Despite some deviations, the same trajectory patterns appear for all Reynolds numbers considered and $UT_1$, $UT_2$, $LT_1$ and $LT_2$ almost preserve their shapes.

It is noted that all vortices except the ones that follow $UT_2$ are formed almost at the same downstream position $x/D \approx 2$. The vortices of $UT_1$ are formed at a position approximately $0.6D$ more upstream and $0.25D$ higher as compared to the ones of $UT_2$. They go upwards until $x/D \approx 4$ and then downwards until they reach the trajectory $UT_2$. So, the vortex trajectory $UT_1$ has a curved shape with a high peak in the near-wake region. On the other hand, the trajectory $UT_2$ has a rather linear shape. The vortices following the $UT_2$ trajectory have a steady upward motion for $Re = 180$ and for $x/D > 7$ the $UT_2$ trajectory almost coincides with the $UT_1$ trajectory. For the other Reynolds numbers presented in Figure 5.10, $UT_2$ has a slightly curved shape but not as pronounced as $UT_1$.

In the lower half of the wake, $LT_1$ has a similar tendency as $UT_2$ but in opposite direction. It has a quasi-linear shape with a steady downwards deflection. $LT_2$ has the same curved shape like $UT_1$ but for the lower half of the wake. Vortices of $LT_2$ follow a downwards trajectory until $x/D \approx 5.5 - 6.0$ and a slightly upwards trajectory further downstream.

The discussion about the vortex trajectories is further extended in Figure 5.11 which demonstrates how the shapes of the different trajectories are associated with the von Kármán vortices at $Re = 180$ in the wake of a wired cylinder. The vortex trajectories are superposed on the instantaneous spanwise vorticity fields at two instants which are $T_{shed}$ apart from each other. The corresponding trajectories of each von Kármán vortex is marked with an arrow. The snapshots are chosen such that they show the wake just after the formation of an upper von Kármán vortex. Trajectory $UT_1$ is associated with the upper vortex which has a compact center region and two elongated braids, as shown in Figure 5.11a. The concentrated vorticity in the vortex center can be noted from the color contrast in the vorticity contours. The preceding lower vortex follows the trajectory $LT_1$. At the phase $t = t_0 + T_{shed}$, the upper vortex which follows the trajectory $UT_2$ is formed. This vortex has a different shape than the former one. It does not have long braids and has a more diffused vorticity concentration in the center. It should be noted that this upper vortex is the one from which the secondary Mode-C vortices are originating, see Chapter 4. This upper vortex is succeeded by a lower vortex which follows the curved trajectory of $LT_2$.

Unlike in the vortex trajectories, the downstream variation of the vortex strength $\Gamma_z$ of the von Kármán vortices does not show a significant difference between the upper and lower wakes. Comparison of results from different Reynolds numbers indicate that the tendency of the circulation values as a function of downstream position $x/D$ is almost the same. However, there is a clear difference between the strengths of upper and lower von Kármán vortices. The circulation values and the difference bet-

**(a)** $t = t_0$



**(b)** $t = t_0 + T_{shed}$
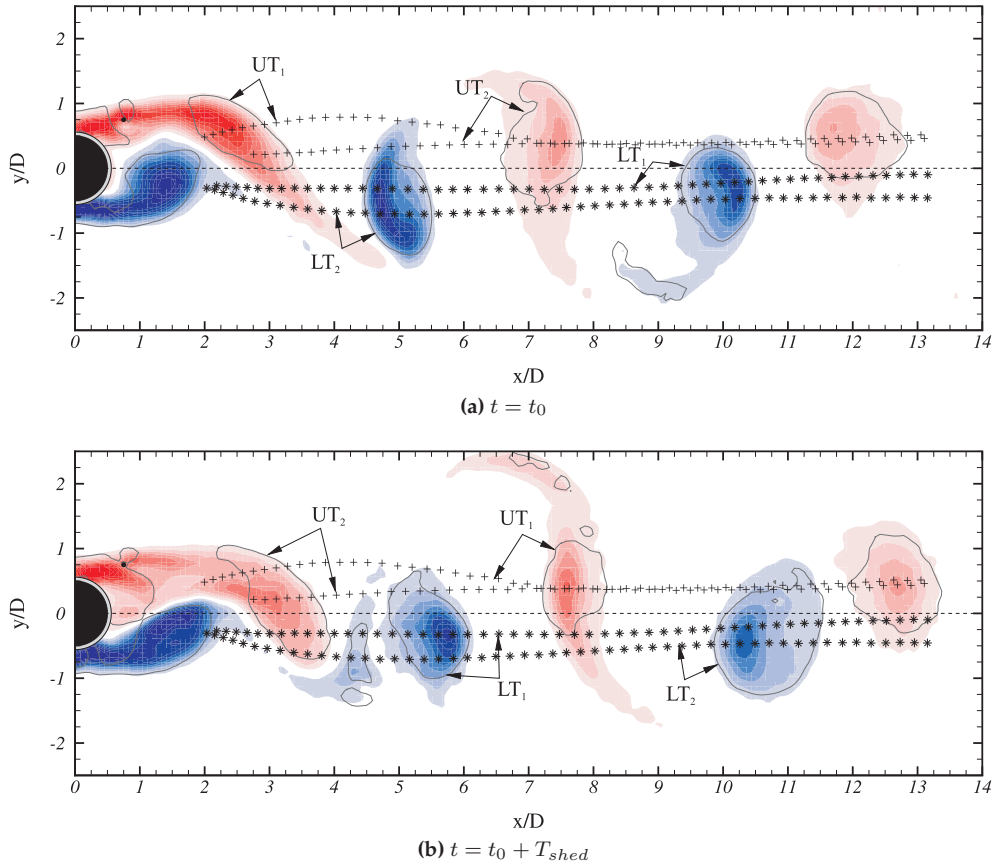
**Figure 5.11:** *Vortex trajectories of von Kármán vortices at $Re = 180$ in the wake of a wired cylinder. Vortex trajectories are superposed on the instantaneous spanwise vorticity field at two instants which are $T_{shed}$ apart from each other. The corresponding trajectory of each vortex is shown with an arrow. Contour levels are $|\omega_z|D/U_\infty = 0.4, 0.8, ..., 4$. Blue and red contours indicate positive and negative vorticity, respectively. Solid lines represent the contour line of $\lambda_2 = -0.1$.*

| Re | $|\Gamma_U|$ | $\Gamma_L$ | $|\Gamma_U| - \Gamma_L$ | Difference |
|-----|-------|-------|---------|-----------|
| 180 | 1.521 | 2.284 | $-0.763$ | $-33.4\%$ |
| 195 | 1.270 | 1.938 | $-0.668$ | $-34.5\%$ |
| 210 | 1.512 | 1.773 | $-0.261$ | $-14.7\%$ |
| 225 | 1.337 | 1.518 | $-0.181$ | $-11.9\%$ |
| 244 | 1.372 | 1.624 | $-0.252$ | $-15.5\%$ |

**Table 5.2:** *Circulation values of von Kármán vortices at downstream position $x/D = 10$. Circulation values in the table are non-dimensionalized with $1/DU_\infty$.*



**Figure 5.12:** *Velocity vectors and streamwise vorticity patterns at the cross-stream plane of $x/D = 4.5$ at $Re = 180$. Contour levels of vorticity are $|\omega_x|D/U_\infty = 0.2, 0.4, ..., 2$. $\Gamma_x^+$ and $\Gamma_x^-$ indicate secondary vortices with positive and negative circulation, respectively. $\lambda_z$ denotes the spanwise wavelength of the secondary vortices and is measured between the centers of vortices of the same sign.*

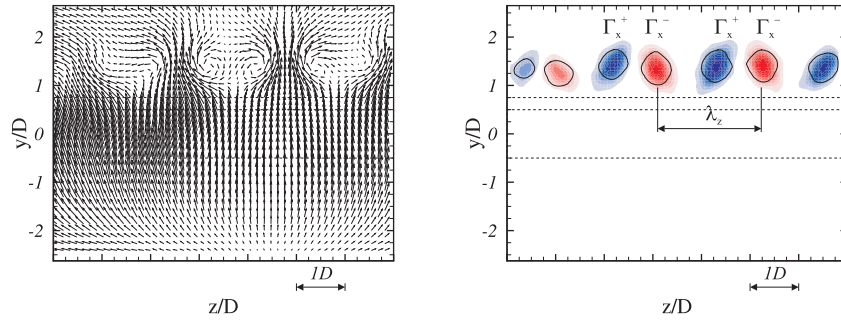ween upper and lower vortices at downstream position $x/D = 10$ are given in Table 5.2 for different Reynolds numbers. As quantified in the table, the strength difference between the upper and lower von Kármán vortices is in the order of $\mathcal{O}(10\%)$. This suggests that during Mode-C transition the upper vortices become weaker than the lower vortices, since some part of the vorticity in the upper shear layer is transferred into secondary vortices.

## 5.4.2   Streamwise vortices

The strengths of the secondary vortices of Mode-C transition are calculated from back-view PIV experiments. Figure 5.12 shows the resulting velocity vectors and streamwise vorticity distribution at the cross-stream plane of $x/D = 4.5$ for a Reynolds number of $Re = 180$. Each vortex is defined with a $\lambda_2 = -0.1$ contour. The circulation $\Gamma_x$ of the corresponding streamwise vortical structures are calculated in the same manner as for the spanwise vortices. In Figure 5.12, $\Gamma_x^+$ and $\Gamma_x^-$ indicate secondary vortices with positive and negative circulation, respectively. $\Gamma_x^+$ implies
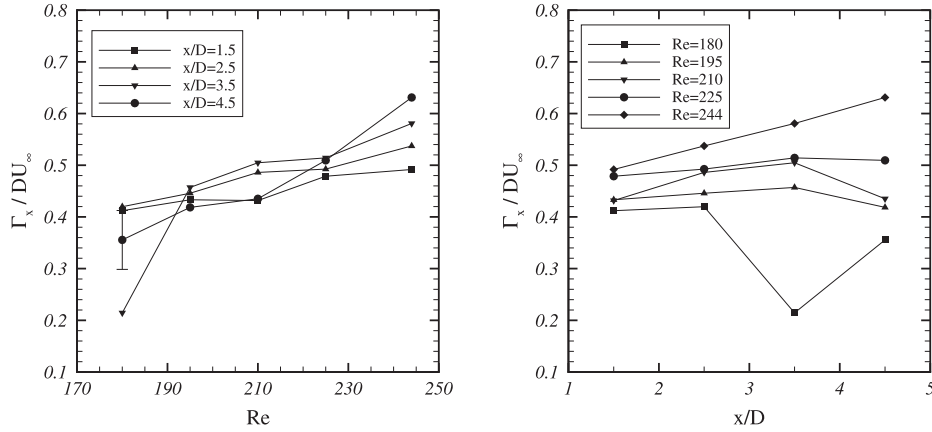
**Figure 5.13:** *Variation of strengths of secondary vortices $\Gamma_x/DU_\infty$ with Reynolds number $Re$ and downstream position $x/D$ in the near-wake.*

counter-clock-wise and $\Gamma_x^-$ implies clock-wise rotation. The strength of the vortices is calculated at the instant at which they are at their highest position with respect to the wake centerline $y/D = 0$. This instant corresponds to the vortex shedding phase where the measurement plane is between the upper and lower primary vortices, see Figure 5.6 for an example. In Figure 5.12, the spanwise distance between the vortices of the same sign determines the spanwise wavelength $\lambda_z$ of Mode-C transition.

Figure 5.13 shows the variation of the strengths of the secondary vortices with Reynolds number and downstream position. The overall strength $\Gamma_x$ is calculated by taking the average of $\Gamma_x^+$ and $|\Gamma_x^-|$ in several snapshots for each back-view PIV experiment. The standard deviation of the circulation calculation ($\sigma/DU_\infty = 0.057$) is shown as an error bar for a representative case. The data show a clear outlier for the case $Re = 180$ and $x/D = 3.5$. Nevertheless, it might be concluded that $\Gamma_x$ is increasing almost linearly with the Reynolds number for $1.5 < x/D < 4.5$ in the near-wake. The average strengths of the Mode-C vortices are $\Gamma_x/DU_\infty = 0.40$ for $Re = 180$ and $\Gamma_x/DU_\infty = 0.56$ for $Re = 244$.

The results of the spanwise wavelength calculation of Mode-C transition are shown in Figure 5.14. Although the data shows a scatter of $\lambda_z$ values, it looks like $\lambda_z$ is decreasing slightly with increasing Reynolds number. The standard deviation of the calculation of the spanwise wavelength is $\sigma/D = 0.15$ and is shown as an error bar for a representative case in Figure 5.14. The average spanwise wavelength values for each corresponding Reynolds number are calculated as $\lambda_z/D = 2.28, 2.20, 2.17, 2.06, 2.10$ for $Re = 180, 195, 210, 225, 244$, respectively. On the other hand, $\lambda_z$ seems to increase with downstream position $x/D$. For example, the average $\lambda_z$ values at each downstream location is $\lambda_z/D = 2.02, 2.13, 2.21, 2.27$ for $x/D = 1.5, 2.5, 3.5, 4.5$, respectively. Most likely, this increase is caused by the end condi-
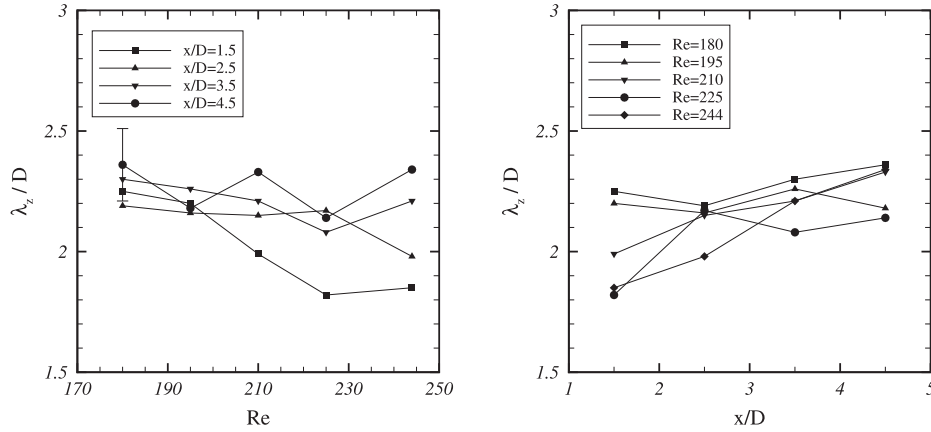
**Figure 5**.14: *Variation of spanwise wavelength of secondary vortices* $\lambda_z/D$ *with Reynolds number* $Re$ *and downstream position* $x/D$ *in the near-wake.*

tions imposed by the end plates. The spanwise wavelength of Mode-C transition for the wired cylinder case is calculated by averaging all the values given in Figure 5.14 and is found to be

$$\frac{\lambda_z}{D} = 2.16 \qquad (5.6)$$

The quantification of the relationship between secondary and primary vortices is done by comparing their strengths. In Figure 5.15, the variation of the strength ratio $\Gamma_x/\Gamma_z$ with Reynolds number is shown for the downstream positions $x/D = 2.5, 3.5, 4.5$. The strength of the upper von Kármán vortex is used in the calculations, since the Mode-C vortices originate from the upper vortices. It can be seen that the circulation of the secondary vortices is significantly smaller than the circulation of the primary von Kármán vortices. The strength of the Mode-C vortices is $\approx 20\%$ of the strength of the von Kármán vortices for $Re = 180$ and is $\approx 30\%$ for $Re = 244$. Discarding the outlier data point at $Re = 180$ and $x/D = 3.5$, one may conclude that $\Gamma_x/\Gamma_z$ varies linearly with the Reynolds number. This result indicates that the growth rate of secondary vortices is higher than the growth rate of primary vortices during Mode-C transition.

## 5.5   Vortex shedding frequency in Mode-C

The existence of von Kármán vortices during Mode-C transition shows that placing a wire in the near-wake does not suppress the vortex shedding. However, it is shown in Chapter 4 that the wire causes approximately $5\%$ reduction in the shedding frequency. These results put Mode-C transition in the framework of the discussion of
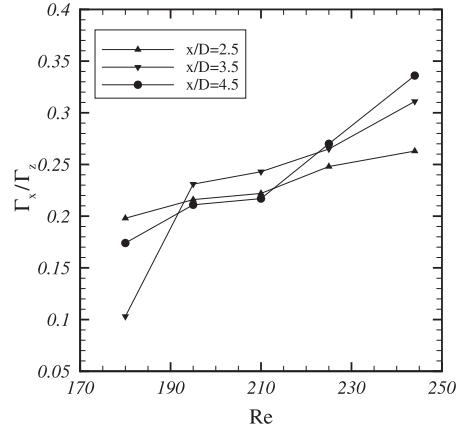
**Figure 5.15:** *Variation of strength ratio $\Gamma_x/\Gamma_z$ of secondary and primary vortices with Reynolds number $Re$ and downstream position $x/D$ in the near-wake.*

Gerrard [6] and Strykowski and Sreenivasan [59] about the physical interpretation of the vortex shedding frequency.

According to the classical model of Gerrard [6], the vortex street formation is related to the interaction of opposite shear layers which has to happen within a certain distance, the so-called formation length. This interaction basically occurs by drawing each other across the wake centerline. Each shear layer must have sufficient strength before it draws the opposite shear layer across the wake. Thus, diffusion of shear layer vorticity over a critical diffusion length or prevention of their interaction over a critical formation length can result in suppression of vortex street formation [59]. If the shear layer vorticity distribution is diffused then the shear layers will not pull each other rapidly, resulting in a reduced shedding frequency, as discussed by Strykowski and Sreenivasan [59]. They observed that the weakened shear layers result in a reduced shedding frequency even if vortex shedding is not suppressed.

To investigate the consistency of the above discussion and the current experimental investigation of Mode-C transition, the time-averaged vorticity contours for the wired and non-wired cylinder wakes at two different Reynolds numbers in the transition regime are shown in Figure 5.16. In this figure, $Re = 180 - 185$ represents an early stage in the transition regime, while $Re = 225 - 230$ represents a later stage. The same contour levels are applied in all figures to ease the comparison. Negative and positive vorticity values are represented with dashed and solid contour lines, respectively.

The effect of the wire is clearly visible in the PIV experiments. Although the spatial resolution of PIV is not high enough to resolve all the small scale flow structures around the wire, it is evidently sufficient to resolve the global effect of the wire on the upper shear layer.
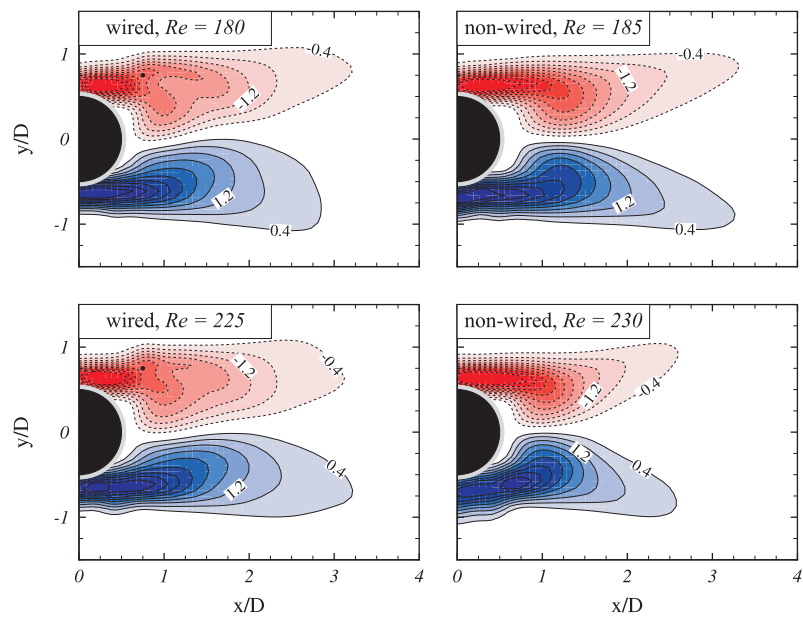
**Figure 5.16:** *Time-averaged spanwise vorticity contours* $\overline{\omega_z}D/U_\infty$ *in the near-wake of the cylinder. Contour levels are* $|\overline{\omega_z}|D/U_\infty = 0.4, 0.8, ..., 4$. *Solid line and dashed line contours indicate positive and negative vorticity, respectively.*

Firstly, the wire breaks the symmetry of the time-averaged vorticity field by diverting some portion of the vorticity in the separated upper shear layer into the near-wake region. Diverted negative vorticity goes slightly below the wake centerline ($y/D = 0$) and dissipates positive vorticity of the lower shear layer. This is seen in the contour lines of positive vorticity close to the wake centerline. They are slightly flat when compared to the non-wired case.

Secondly, the wire generated vorticity spreads the negative vorticity of the separated upper shear layer of the main cylinder. For the wired case at $Re = 180$, it can be seen that a direct effect of the wire on the time-averaged vorticity patterns is confined to the region of $x/D = 0.75 - 1.5$ in the upper shear layer. Increasing the Reynolds number does not much change the effect of the wire on the time-averaged vorticity. The same vorticity patterns are seen both for $Re = 180$ and $Re = 225$ in the wired cases. For $Re = 225$, the effect of the wire is also confined to the region of $x/D = 0.75 - 1.5$. A quantification of vorticity diffusion can be made by considering the circulation values of the von Kármán vortices, which originate from the separating shear layers. As given in Table 5.2, for Reynolds number $Re = 180$ of the wired cylinder case, the circulation of the upper vortices is $\mathcal{O}(10\%)$ lower than of the lower vortices.

The diffusion in the upper shear layer is accompanied by thickening of the shear layer [6, 59]. It is discussed by Strykowski and Sreenivasan [59] that the shedding frequency is inversely proportional to the thickness of the separating shear layer. As a measure of the shear layer thickness, the momentum thickness is used [68]:

$$\frac{\theta_u}{D} = \int_0^\infty \frac{\overline{u}}{U_\infty}\left(1 - \frac{\overline{u}}{U_\infty}\right) \mathrm{d}\left(\frac{y}{D}\right) \tag{5.7}$$

where $\theta_u$ is the upper shear layer thickness and $\overline{u}$ the time-averaged horizontal velocity.

The results are presented in Figure 5.17 for two Reynolds numbers. From the figure it is clear that the momentum thickness, i.e. the shear layer thickness, of the wired cylinder is larger than of the non-wired cylinder, indicating a lower shedding frequency. For example at $x/D = 1$, the difference in the shear layer thickness is $0.028D$ for $Re = 180$ and $0.016D$ for $Re = 225$, which corresponds to an approximately $26\%$ and $16\%$ increase with respect to the reference non-wired cases.

One may conclude that the wire thickens the shear layer by spreading its vorticity content. Following the discussion of Strykowski and Sreenivasan [59], the reduction of the shedding frequency in Mode-C transition can be linked to their conclusion about weak shear layers which are not strong enough to pull each other across the wake.
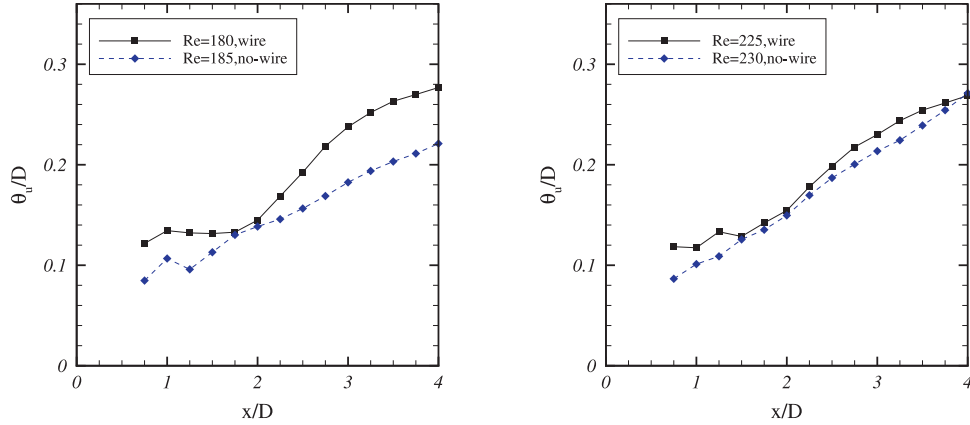
**Figure 5.17:** *Downstream variation of the upper shear layer momentum thickness for wired and non-wired cases at different Reynolds numbers.*

## 5.6 Concluding remarks

In this chapter, the discussion of Mode-C transition is extended by investigating and quantifying some of the observations such as the shedding frequency reduction, the energy content of the wake, the vortex trajectories of von Kármán vortices and the spanwise wavelength of Mode-C transition. The analyzes are done mainly by focusing on fluctuating flow features, energy characteristics and vortex dynamics. The data used in the analyses is obtained from several side-view and back-view PIV measurements.

First of all, the effect of the wire on temporal characteristics is investigated by evaluating the variation of rms-velocity characteristics of the wake. It is shown that the $u_{rms}/U_\infty$ profile in the upper half of the wake is broadened. Peak $u_{rms}$ values do not change significantly in the wired cases but they are reduced by approximately $10 - 15\%$ compared to the non-wired cases. Moreover, they stay almost constant throughout the Reynolds number range $Re = 180 - 225$.

Secondly, discrete energy components are calculated at different frequencies of the energy spectrum. The effect of the wire is clearly evident in the cross-stream plot of energy intensity at subharmonic frequency $f_1 \approx f_0/2$. There is a clear peak in the energy intensity of $f_1$ in the upper half of the wake around $y/D = 1.25$. The energy intensity at the von Kármán vortex shedding frequency in the upper half of the wake is less than the energy intensity in the lower half, meaning that the excess energy is stored at subharmonic frequency $f_1 \approx f_0/2$. Furthermore, from the downstream variation of the discrete integrated energies, one may conclude that von Kármán vortices die faster than secondary Mode-C vortices.

Thirdly, the vortex dynamics in Mode-C transition is investigated. It is shown

that the period-doubling nature of the transition also exhibits itself in the vortex trajectories. In non-wired cylinder flows there is one single trajectory describing the path of the von Kármán vortices for each half of the wake. However, for the wired cylinder case (Mode-C transition), there are two different trajectories for both upper and lower vortices. The strength difference between the upper and lower von Kármán vortices is in the order of $\mathcal{O}(10\%)$, which suggests that during Mode-C transition the upper vortices become weaker than the lower vortices, since some part of the vorticity in the upper shear layer is transferred into the secondary vortices.

The vortex strength calculations of secondary vortices indicate that the strength of the secondary vortices, $\Gamma_x$, is increasing almost linearly with Reynolds number $Re$. The strength of secondary Mode-C vortices is $\approx 20\%$ of the strength of von Kármán vortices for $Re = 180$ and is $\approx 30\%$ for $Re = 244$. This result suggests that the growth rate of secondary vortices is higher than the growth rate of primary vortices during Mode-C transition. Also a quantification of the spanwise wavelength of Mode-C instability is done. The spanwise wavelength of Mode-C transition for wired cylinder case is calculated as $\lambda_z/D = 2.16$.

Finally, a physical interpretation of the effect of the wire on the shedding frequency in Mode-C transition is given. The discussion is based on the classical vortex shedding theory of Gerrard [6] and its discussion by Strykowski and Sreenivasan [59]. It is concluded that indeed the wire thickens the shear layer by spreading its vorticity content in Mode-C transition, which results in a reduction of the circulation of the upper vortices and consequently the shedding frequency.

# Shedding Mode-II in the wake of a rotating circular cylinder

## 6.1 Introduction

In this chapter the transition of the flow behind a circular rotating cylinder is investigated experimentally. The wake of a rotating cylinder is determined by a stability diagram showing the flow state with respect to rotation rate $\alpha$ and Reynolds number, see Figure 6.1. The rotation rate is defined as $\alpha = (D\Omega)/(2U_\infty)$, where $D$ is the cylinder diameter, $\Omega$ the constant angular velocity of the rotating cylinder, $U_\infty$ the free-stream velocity. The flow is divided into different stages. Shedding Mode I is seen at low rotation rates and is associated with a deflected von Kármán vortex street [35, 37]. El Akoury et al. [37] also showed, using three-dimensional numerical simulations, that at very low rotation rates secondary streamwise vortical structures appear in the wake. Their results also indicate that the cylinder rotation has a stabilizing effect on three-dimensional perturbations acting on shedding vortices in Shedding Mode I.

When the rotation rate is increased beyond the critical value for Shedding Mode I the flow goes into a stable region. Using numerical simulations it is shown by Kang et al. [33] that the rotation of a cylinder can suppress vortex shedding effectively when the rotation rate exceeds a value of $2$. The same results are also reported by [14, 34–37].

As seen in Figure 6.1a, in a very narrow range of high rotation rates Shedding
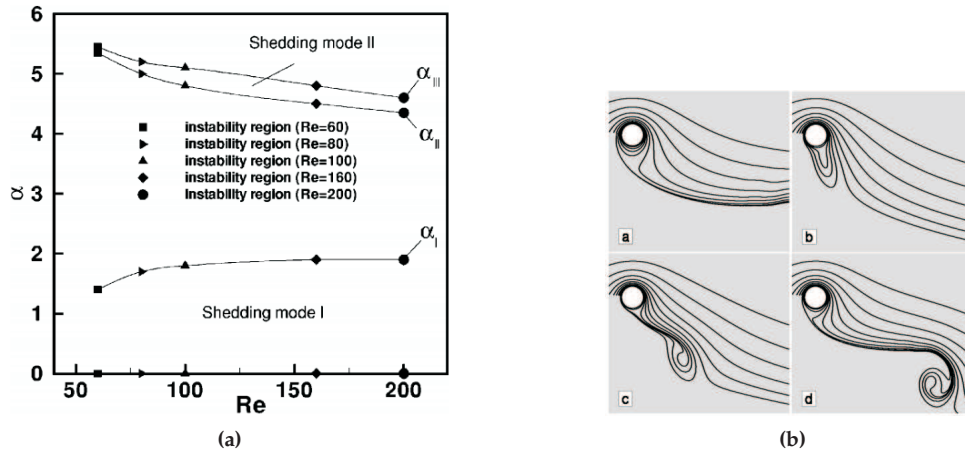
**Figure 6.1:** *Rotating cylinder flow (a) Stability diagram for different Reynolds numbers and rotation rates, (b) Development of the vortex street in the second vortex shedding mode behind the rotating cylinder for $Re = 160$ and $\alpha = 4.7$. (Figure is reproduced from Stojkovic et al. [14]).*

Mode II takes place. This phenomenon was investigated by Stojkovic et al. [34]. They examined the flow at higher rotation rates for a Reynolds number of $Re = 100$. They showed the existence of this second shedding mode in a narrow range of rotation rate $4.85 - 5.15$ for the first time. This mode has a shedding frequency of $St \approx \mathcal{O}(10^{-2})$, which is one order of magnitude lower than that of Shedding Mode I. Furthermore, the shedding period is slightly dependent on the value of the rotation rate. Their work was extended further in Stojkovic et al. [14]. They constructed a complete stability diagram in the Reynolds number-rotation rate plane which is sketched in Figure 6.1. Mittal and Kumar [35] performed simulations and a stability analysis for the flow at $Re = 200$. They also identified a second instability mode at $\alpha = 4.5$. Moreover, numerical studies of several authors indicate that Shedding Mode II is associated with a single shed vortex, as shown in Figure 6.1b, [14, 35–37]. In addition, the numerical simulations of Mittal [36] show the existence of three-dimensional centrifugal instabilities in the wake at $\alpha = 5$ and $Re = 200$.

In a recent study of rotating cylinder flow, Pralits et al. [38] investigated different aspects of Shedding Mode II. They studied the linear instability of the flow around a rotating circular cylinder at $Re = 100$. They examined the physical mechanisms using structural sensitivity and a perturbation kinetic energy budget analysis. They have also identified Shedding Mode II in the rotation rate range of $4.85 - 5.17$, which is characterized by the shedding of one counterclockwise vortex from the upper part of the cylinder. In their study, the origin of the instability is identified as the advection of positive vorticity of the base flow from the low-rear part of the cylinder to the stagnation point where it accumulates and sheds.

The objective of the present work is to experimentally verify the existence of Shedding Mode II and to compare its main features with those obtained in the numerical studies of Stojkovic et al. [14]. To the best of our knowledge Shedding Mode II has never been identified experimentally. The chapter starts with a brief description of the experimental method and the set-up. Following this brief introduction, the results from the experiments are summarized. Firstly, the validation of the experimental method is discussed and secondly, the results about Shedding Mode II are presented. The final section consists of some concluding remarks about the experimental results.

## 6.2   Flow configuration and experimental techniques

The rotating cylinder experiments are performed in the towing tank with a counter-clock-wise rotating cylinder. The details of the towing tank and experimental model are already given in Chapter 2. The qualitative and quantitative information about the flow physics is obtained from flow visualization experiments using the tin-precipitation method and PIV experiments. The rotating cylinder experiments are performed at a fixed Reynolds number of $Re = 100$ for various rotation rates which are presented in Figure 6.2a. Since Shedding Mode II appears in a very narrow range of the rotation rate $\alpha$, the experiments were carried out in a very controlled manner. Several experiments are repeated at different rotation rates until Shedding Mode II vortices are seen. Here only the results of experiments in the range $\alpha = 4.96 - 5.12$ are presented, as Shedding Mode II vortices are only found in those experiments.

The cylinder model used for the rotating cylinder experiments has a diameter of $D = 10$ mm. The end plates have a square shape with a width of $200$ mm and are placed parallel to each other due to the imposed restrictions of the rotating bearings and optical accessibility of the cameras. The length of the cylinder is $L = 480$ mm and the length of the section that faces the inflow directly is $L = 380$ mm. This corresponds to a cylinder aspect ratio of $L/D = 38$ for the rotating case. The cylinder is placed in the middle of the water level, resulting in a distance of the cylinder center to the free surface and bottom wall of $30D$. The cylinder is connected to a DC electrical motor via a belt system and rotates in counter-clockwise direction from the camera point of view.

For the flow visualization experiments the electrolytic tin-precipitation method is used. The details of the method are summarized in Chapter 2. In the rotating cylinder set-up, the tin particles are introduced from a vertically placed tin-sheet, as shown in Figure 6.2b. The tin-sheet is placed in front of the cylinder and its thickness is approximately $0.6$ mm. The tin particles are illuminated using a laser plane and their images are recorded using a CCD camera with wide-angle lens.

The quantitative evaluation of the flow is made by using Particle Image Velocimetry measurements. For this purpose, the water in the towing tank was seeded
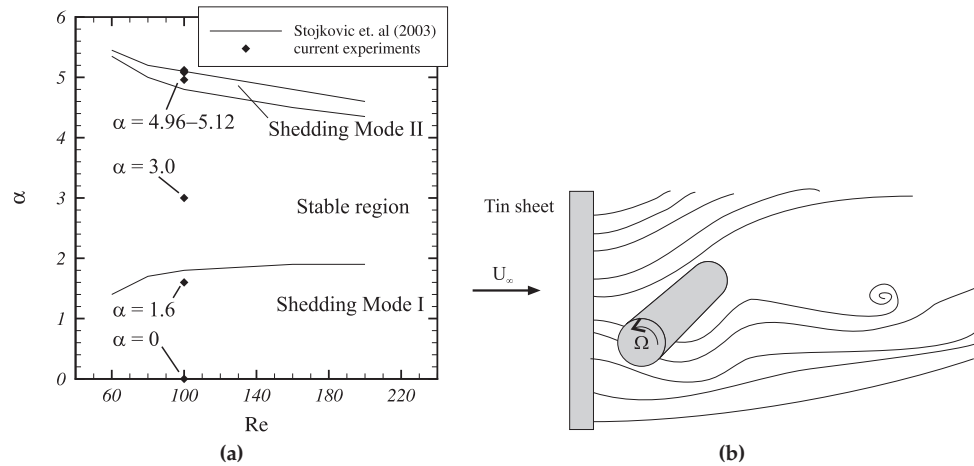
**Figure 6.2:** *Brief information on rotating cylinder experiments; (a) Reynolds number-rotation rate values of the performed experiments at $Re = 100$. The boundaries of the instability modes are reproduced from Stojkovic et al. [14], (b) Sketch of the tin-precipitation set-up in the rotating cylinder experiments.*

with PSP particles having a diameter of $20\mu m$. The same configuration and set-up, as used in the side-view experiments for the wired cylinder, is also used for the rotating cylinder experiments. The details of the side-view experiments for the wired cylinder configuration is given in Chapter 2. However, due to the upwards deflection of the wake, the positions of the cameras are arranged accordingly to cover a larger field of view. The images obtained from different cameras are denoted as 'frame 1' and 'frame 2' in the relevant figures throughout the text.

## 6.3   Results

As first step of the rotating cylinder experiments, the reliability of the experimental system is assessed. For that purpose both flow visualization and PIV experiments are performed at low rotation rates. These rotation rates correspond to three different flow regimes in the stability diagram shown in 6.2a, i.e. von Kármán vortex street, Shedding Mode I and stable region.

The flow visualization and PIV results of the validation experiments are shown in Figure 6.3 and Figure 6.4, respectively. The flow direction is from left to right in both figures and the cylinder is rotating in counter-clockwise direction. Both figures exhibit representative instantaneous snapshots of the flow field. In Figure 6.4, the solid line and dashed line contours indicate positive and negative vorticity, respectively. The data values in the overlapping region of two frames are averaged using the

merging method discussed in Chapter 2. The strengths of the vortices are calculated using the $\lambda_2$-criterion with $\lambda_2 = -0.1$ defining the vortex boundary.

### 6.3.1 von Kármán Vortex Street ($\alpha = 0$)

For $\alpha = 0$ and $Re = 100$, the flow is expected to exhibit two-dimensional von Kármán vortex shedding patterns. The results from the experiments can be seen in Figure 6.3 and Figure 6.4, which clearly show a von Kármán vortex street. The PIV measurements indicate that the vortices are symmetric with respect to the wake centerline $y/D = 0$. The Strouhal number calculated from PIV is $St = 0.165$ which is in good agreement with the values from the literature [47].

### 6.3.2 Shedding Mode I ($\alpha = 1.6$)

Shedding Mode I can be seen at $\alpha = 1.6$ and $Re = 100$. From Figure 6.3 it can be noted that the vortex shedding is not suppressed completely but changed due to the rotation. The rotation rate is relatively slow and an upward deflected von Kármán vortex street can be seen, as shown in Figure 6.4. In comparison with the non-rotating case, the strength of the vortices is reduced, as can be noted from the calculated circulation values in Figure 6.4. The Strouhal number calculated from the PIV image sequence is $St = 0.164$. El Akoury et al. [37] showed that in Shedding Mode I region the Strouhal number does not change significantly from the non-rotating case.

### 6.3.3 Stable region ($\alpha = 3.0$)

In the stability diagram shown in Figure 6.2a, $\alpha = 3.0$ is between the two shedding modes. In this rotation rate the vortex shedding is completely suppressed and there is no vortex shedding from the cylinder. This can be clearly seen from the visualization and PIV experiment results in Figure 6.3 and Figure 6.4.

Based on the above results, one may conclude that the results of the experiments are consistent with the results of the literature and the set-up produces reliable results for both non-rotating and rotating cylinder experiments.

### 6.3.4 Shedding Mode II

Further increase of the rotation rate of the cylinder puts the flow regime into another instability region which is known as Shedding Mode II [14]. In this mode, shedding of a single vortex takes place at a much lower frequency, as shown in Figure 6.5.

Figure 6.5 represents an instantaneous spanwise vorticity snapshot from PIV measurement at rotation rate $\alpha = 5.08$ for $Re = 100$. Increasing the rotation rate results in a more upward deflected wake. Therefore, to capture the vortical structures, frame 2 is placed in an upward position compared to frame 1. The existence of
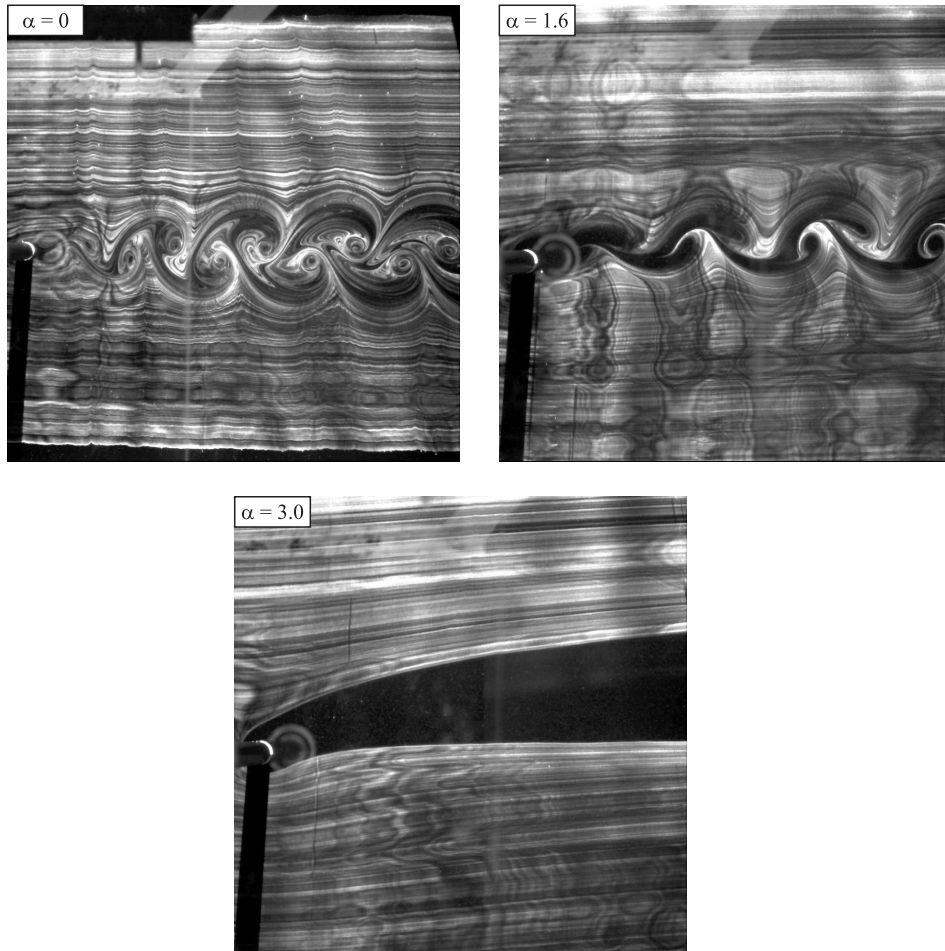
**Figure 6.3:** *Instantaneous flow visualization images at rotation rates* $\alpha = 0, 1.6$ *and* $3.0$ *for* $Re = 100$.
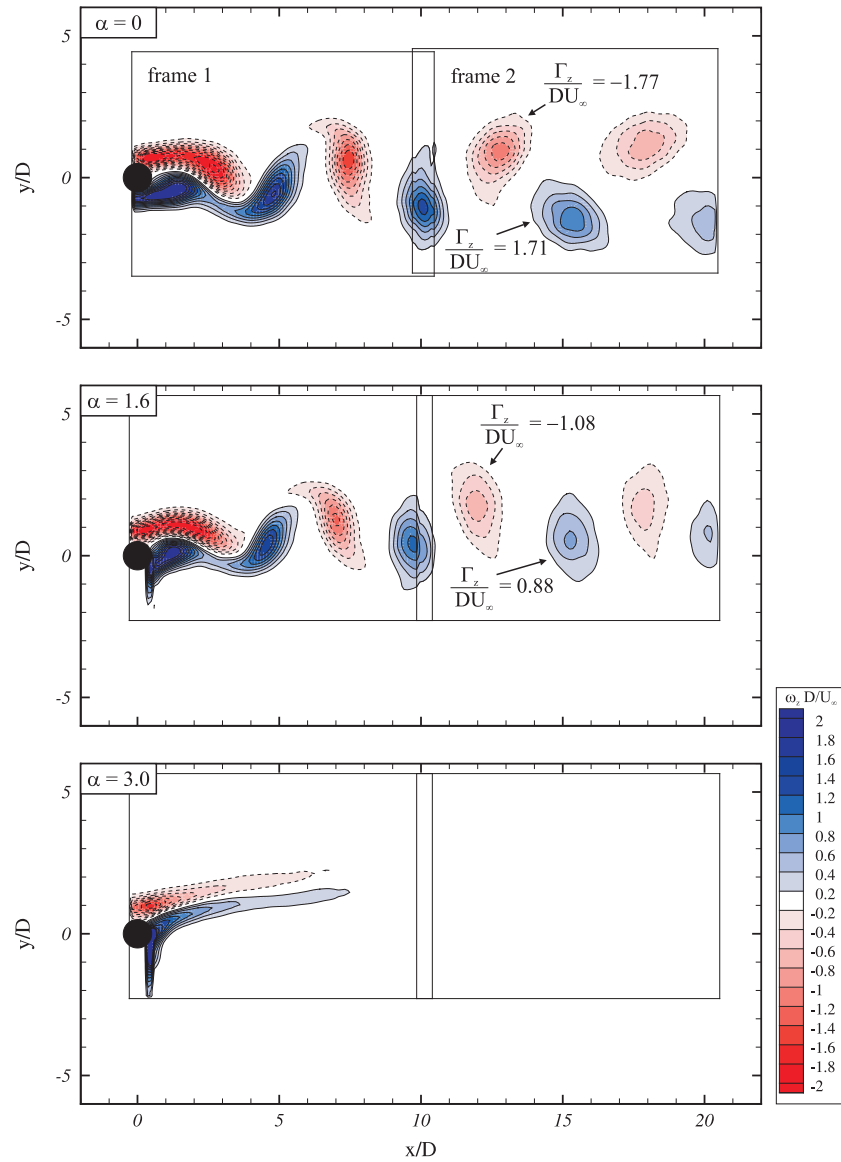
**Figure 6.4:** *Instantaneous spanwise vorticity $\omega_z D/U_\infty$ snapshots calculated from PIV results at rotation rates $\alpha = 0, 1.6$ and $3.0$ for $Re = 100$.*
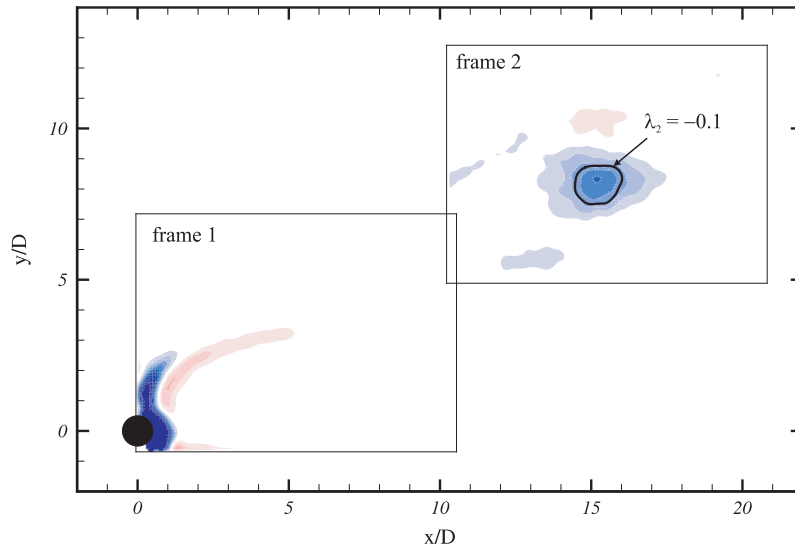
**Figure 6.5:** *Instantaneous spanwise vorticity snapshot calculated from PIV results at rotation rate $\alpha = 5.08$ for $Re = 100$. Contour levels are $|\omega_z|D/U_\infty = 0.1, 0.1, ..., 1$. Blue and red colors of vorticity indicate positive and negative values, respectively. The vortex of Shedding Mode II is shown in frame 2. The solid line represents a $\lambda_2 = -0.1$ contour line.*
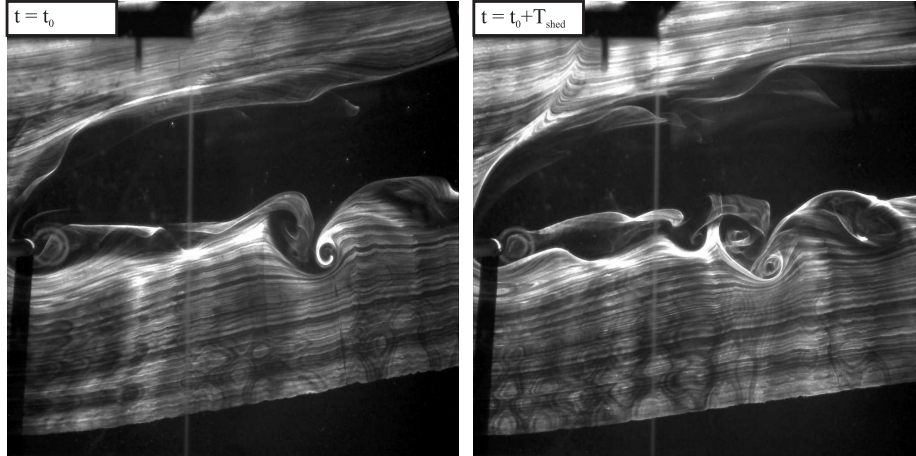


**Figure 6.6:** *Two out of four captured vortices of Shedding Mode II in flow visualization experiments at $\alpha = 4.96$ for $Re = 100$. The shedding period $T_{shed} \approx 57.4s$ in this particular experiment.*

**Figure 6**.**7:** *Four captured vortices of Shedding Mode II in PIV experiments at $\alpha = 5.08$ for $Re = 100$. Each snapshot shows instantaneous spanwise vorticity $\omega_z D/U_\infty$ contours. Contour levels are $|\omega_z| D/U_\infty = 0.1, 0.1, ..., 1$. Blue and red colors of vorticity indicate positive and negative values, respectively. The shedding period $T_{shed} \approx 52.5s$ in this particular experiment.*

the vortical structure is determined by applying the $\lambda_2$-criterion. It is clear that the area bounded by $\lambda_2 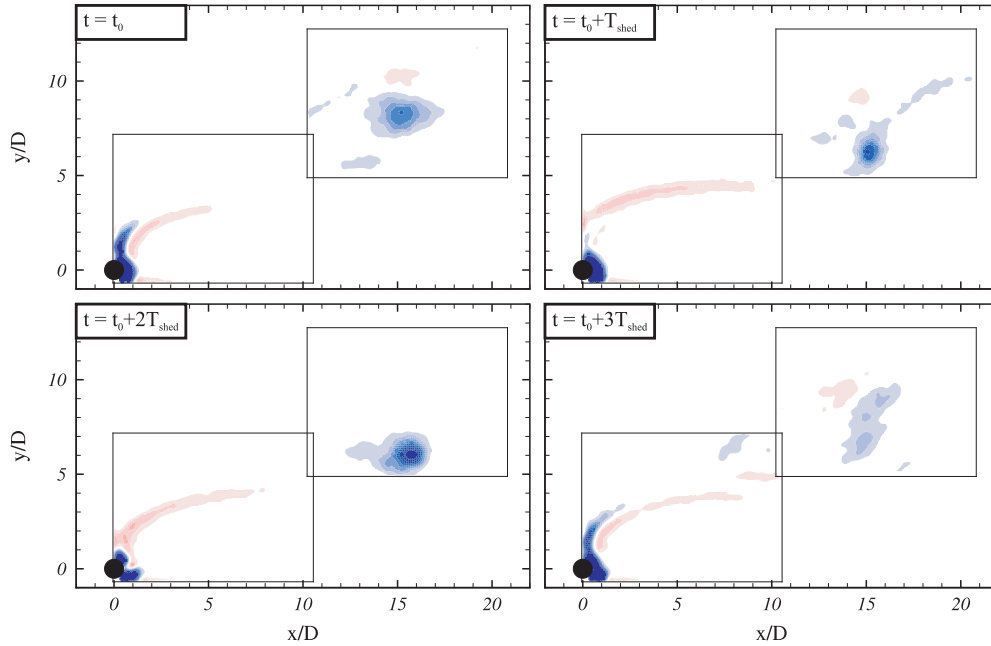= -0.1$ reflects a vortex. The single vortex of Shedding Mode II contains positive vorticity which indicates a counter-clock-wise rotation.

At two different rotation rates ($\alpha = 4.96, 5.1$) single vortices with large shedding periods are observed in the flow visualization experiments. Sample snapshots from the results of flow visualization experiments at $\alpha = 4.96$ and $Re = 100$ are presented in Figure 6.6. The experiments at this parameter value of $\alpha$ made it possible to identify four single vortices of Shedding Mode II; as example only two of them are shown in Figure 6.6. At this stage the wake behind the rotating cylinder is not as stable as it is at $\alpha = 3.0$. This feature can be seen from the behavior of the tin sheet. In the lower part of the wake a distinct and counter-clock-wise rotating vortex is observed in both of the images. The period between the vortices is calculated using the image sequence and is denoted as $T_{shed}$. The resulting Strouhal number of the vortex shedding is $St \approx 0.017$. This value of the non-dimensional shedding frequency is of the same order-of-magnitude as found from numerical simulations of Stojkovic et al. [14].

Furthermore, Figure 6.7 shows the results of PIV measurements in the Shedding

Mode II region at $\alpha = 5.08$ and $Re = 100$. The figure shows four snapshots of instantaneous spanwise vorticity contours $\omega_z D/U_\infty$. There are clear positive $\omega_z$ concentrations in frame 2 of the snapshots in Figure 6.7. These vorticity concentrations actually denote the vortical structures of Shedding Mode II. The snapshots in Figure 6.7 are chosen such that they represent the vortex shedding phase where the single vortex is at a downstream position $x/D = 15$. The time difference between each frame is approximately one shedding period. During the experiment only four vortices were captured. This indicates that the flow may not be fully developed, which means that the period between the consecutively shed vortices is not constant. Nevertheless, the shedding period is calculated by averaging the time passed between consequent detected vortices. From this average shedding period the Strouhal number is found to be $St \approx 0.0262$.

The formation and shedding process of a single vortex at $\alpha = 5.08$ and $Re = 100$ is presented in Figure 6.8. Each plot of instantaneous spanwise vorticity $\omega_z D/U_\infty$ is $0.05T_{shed}$ apart from each other. As depicted in the figure, the vortex shedding is completely different from the non-rotating cylinder case and the rotating cylinder case in Shedding Mode I. A single vortex is developing and shed from the upper part of the rotating cylinder. At phase $t = 0$ there is a clear concentration of positive vorticity in the upper part of the cylinder. Apparently, when this vorticity concentration reaches sufficient strength, it detaches from the cylinder and sheds downstream forming a single vortex. This vortex has a positive vorticity content and rotates counter-clockwise, i.e. with the same rotation direction as the cylinder.

Further assessment of Shedding Mode II experiments is done by comparing the Strouhal numbers calculated from experiments and obtained from literature. The results are presented in Figure 6.9. The error bars in the figure represent the standard deviation in the calculation of Strouhal numbers. It is clear that the order of magnitude of the measured shedding frequencies is the same as compared to the numerical results in literature [14]. However, there is a scatter in the experimental results, since in the present experiments it was not possible to realize a fully developed flow for Shedding Mode II.

## 6.4   Concluding remarks

In this chapter, the flow past a rotating circular cylinder at Reynolds number $Re = 100$ has been analyzed for various rotation rates. Since the main objective is to provide experimental evidence about Shedding Mode II region ($4.8 \lessapprox \alpha \lessapprox 5.2$), the Reynolds number is fixed at $Re = 100$ in order to reduce the number of experiments. For that purpose a rotating cylinder set-up is designed and placed in the towing tank.

Firstly, experiments are performed to test the configuration and to assess the experimental results before conducting experiments in the Shedding Mode II region.
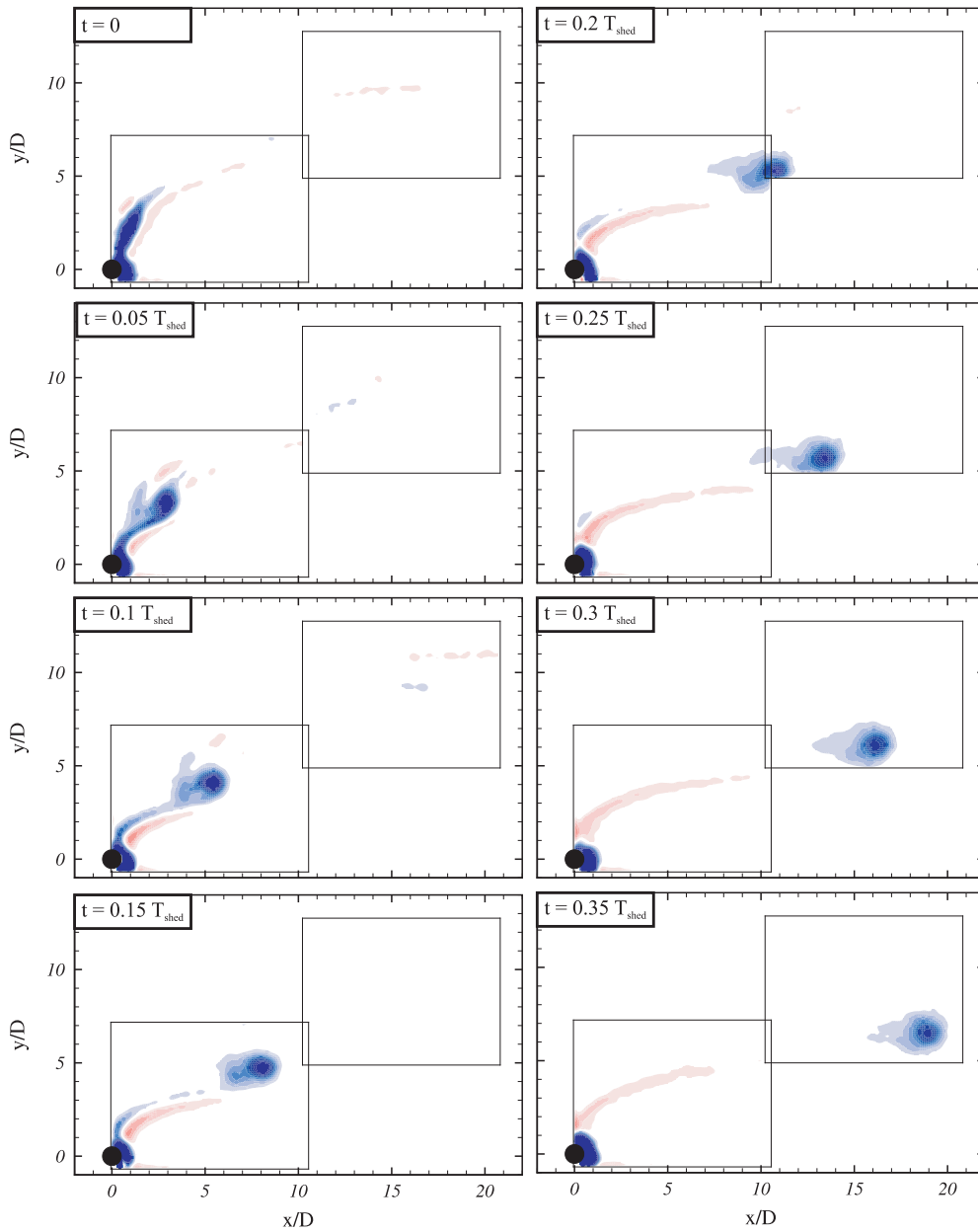
**Figure 6.8:** *Formation and shedding of a single vortex during Shedding Mode II at $\alpha = 5.08$ for $Re = 100$. Each snapshot is $0.05 T_{shed}$ apart from each other shows instantaneous spanwise vorticity $\omega_z D/U_\infty$ contours. Contour levels are $|\omega_z|D/U_\infty = 0.1, 0.1, ..., 1$. Blue and red colors of vorticity indicate positive and negative values, respectively.*
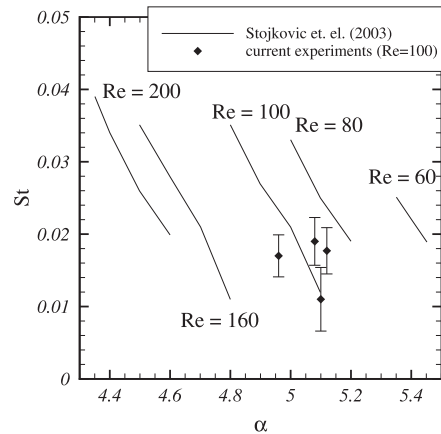
**Figure 6**.9: *Comparison of rotation rate-Strouhal number results of current PIV experiments with literature values. The literature values are reproduced from Stojkovic et al. [14].*

The measurements at lower rotation rates showed that the rotating cylinder set-up provides results in agreement with the literature values.

Secondly, the existence of Shedding Mode II is proved experimentally. At $\alpha = 4.96, 5.1$ for flow visualization experiments and at $\alpha = 5.08, 5.12$ for PIV measurements single vortices with large shedding periods are observed. These vortices are shown to be Shedding Mode II vortices which contain positive spanwise vorticity and rotate in counter-clockwise direction.

The period of Shedding Mode II is quite large when compared to the shedding period of von Kármán vortices and it requires a large time of experiment in order to see the phenomenon. Therefore, the experimental results show only three or four distinct vortices shed from the rotating cylinder depending on the rotation rate. Practically it was not possible to extend the experimental time so the Strouhal numbers are calculated based on the averaged shedding period. Nevertheless, based on the qualitative patterns and the order of magnitude of the shedding frequency, it is concluded that the vortices observed in the experiments are indeed vortices of Shedding Mode II.

# Conclusions and recommendations

## 7.1 Concluding remarks

This thesis presents a detailed experimental characterization of Mode-C transition in the wake of a wire-disturbed cylinder and experimental evidence of the existence of Shedding Mode II instability in the wake of a rotating cylinder.

Several methods are used and upgraded to reach the objectives of the research:

- The Spectral Element Method is used for an accurate numerical analysis of the two-dimensional flow. Special attention is given to the grid resolution to accurately reflect the effect of the very thin wire on the main cylinder wake.

- Qualitative information of the flow physics is obtained from electrolytic tin precipitation experiments. The use of a tin foil covering the cylinder provided a significant improvement of the flow visualization results. It improved the quality of the images by introducing the tracer particles directly into the boundary layer of the cylinder.

- Quantitative information about the flow structures is obtained using Particle Image Velocimetry. Placing the cameras side-by-side provided a larger field-of-view without losing resolution. The characterization of the secondary stream-wise vortices is achieved by using a simple mirror set-up which allowed to perform PIV measurements in the cross-stream plane.

The main conclusions of this thesis are:

- Based on a detailed numerical analysis a hypothesis about the wake deflection in the two-dimensional case is formulated. The hypothesis states that the deflection of the wake is primarily caused by a modification of the vortex arrangement in the wake. A repositioning of the vortices is a necessary and sufficient condition for the wake deflection to occur. This repositioning can be achieved either by slightly delaying the formation of a vortex or by employing a strength difference between the upper and lower row vortices.

- A clear and informative observation of the period-doubling phenomenon in the Mode-C transition regime in the wake of a wire disturbed cylinder is documented. It is shown that in Mode-C instability the streamwise vortices establish a feedback mechanism between the upper primary vortices only. This acts in such a way that vortex loops are generated at the same spanwise position in every two cycles. This mechanism is self-sustaining.

- The origin of the secondary streamwise vortices in Mode-C transition is analyzed. It is shown that the secondary vortices in Mode-C transition are actually the vortex loops that originate from the upper vortex. These vortex loops are further stretched in the braid region and roll-up to form streamwise counter rotating vortex pairs. Therefore, some part of the streamwise vorticity content of the upper von Kármán vortex is transferred to the secondary vortices. This vorticity transfer results in upper von Kármán vortices which are weaker than the lower ones. The analysis of the discrete energy content of the wake supports this justification by showing that the energy intensity at von Kármán vortex shedding frequency $f_0$ in the upper half of the wake is less than the energy intensity in the lower half, meaning that the excess energy is transferred to the subharmonic frequency $f_1 \approx f_0/2$.

- Experimental evidence for the existence of Shedding Mode II in the rotating cylinder wake is presented. Based on the qualitative and quantitative vortex patterns and the order of magnitude of the shedding frequency, it is concluded that the vortices that are observed in the experiments are indeed vortices of Shedding Mode II.

## 7.2 Recommendations for further research

Regarding the research performed in this study, several recommendations for future research are provided:

- Mainly two-dimensional measurements are used here to investigate a three-dimensional phenomena. The application of two-dimensional measurement

techniques provided profound information about Mode-C transition. Applications of advanced three-dimensional measurement techniques such as tomographic PIV and three-dimensional Particle Tracking Velocimetry can provide additional information about three-dimensional dynamics and correlations in the wake.

- The lacking of three-dimensional simulations in this research is due to the fact that these simulations require large computational power. The increased number of computational points around the wire made a Spectral Element simulation using the SEPRAN software on a single node unfeasible. Performing an accurate and feasible three-dimensional numerical study of Mode-C transition in a wired cylinder wake requires parallelization of the code.

- A thorough analysis of Mode-C transition in the wake of a wired cylinder has been performed. However, there are still some points that are not addressed in this thesis. One of them is the stability analysis of the transition. Several numerical studies addressed this issue by performing a stability analysis of the wake flow around non-wired cylinders and circular rings. Performing a stability analysis using PIV data still remains a challenge. Another point is the effect of the wire location on Mode-C transition. This point has not been addressed in this thesis since the main objective is the characterization and physical explanation of the Mode-C wake. Hence, the wire is placed at a fixed position where Mode-C transition is shown to exist.

- Dynamic Mode Decomposition can also be a useful tool for the analysis of experimental data. Dynamic Mode Decomposition is a data decomposition method which allows the extraction of dynamically relevant flow features from time resolved experimental data [74].

- Regarding the rotating cylinder experiments, longer experimental times are needed. This is only feasible in a water channel configuration. The quality of PIV measurements can be improved by using multiple lasers with variable pulse lengths which are synchronized with multiple cameras to resolve the flow structures both in the near-wake and far-wake of the rotating cylinder at the same time.

# Bibliography

[1] T. P. DeFelice, D. J. Meyer, G. Xian, J. Christopherson, and R. Cahalan. Landsat-7 reveals more than just surface features in remote areas of the globe. *Bulletin of the American Meteorological Society*, 81(5):1047–1049, 2000.

[2] F. Durst. *Fluid Mechanics: An introduction to the theory of fluid flows*. Springer, 2008.

[3] H. Lamb. *Hydrodynamics*. Cambridge University Press, 2006.

[4] A. Roshko. On the development of turbulent wakes from vortex streets. Technical Report 1191, NACA, 1954.

[5] A. Roshko. On the wake and drag of bluff bodies. *Journal of Aeronautical Sciences*, 22(2):124–132, 1955.

[6] J. H. Gerrard. The mechanics of the formation region of vortices behind bluff bodies. *Journal of Fluid Mechanics*, 25:401–413, 1966.

[7] J. H. Gerrard. The wakes of cylindrical bluff bodies at low Reynolds number. *Philosophical Transactions of the Royal Society of London. Series A, Mathematical and Physical Sciences*, 288(1354):351–382, 1978.

[8] R. Green and J. Gerrard. Vorticity measurements in the near wake of a circular cylinder at low Reynolds numbers. *Journal of Fluid Mechanics*, 246:675–691, 1993.

[9] M. F. Unal and D. Rockwell. On vortex formation from a cylinder. Part 1. The initial instability. *Journal of Fluid Mechanics*, 190:491–512, 1988.

[10] C. H. K. Williamson. Vortex dynamics in the cylinder wake. *Annual Review of Fluid Mechanics*, 28:477–539, 1996.

[11] C. H. K. Williamson. Three-dimensional wake transition. *Journal of Fluid Mechanics*, 328:345–407, 1996.

[12] M. Ren, C. C. M. Rindt, and A. A. van Steenhoven. Three-dimensional transition of a water flow around a heated cylinder at $Re = 85$ and $Ri = 1.0$. *Journal of Fluid Mechanics*, 566:195–224, 2006.

[13] H.-Q. Zhang, U. Fey, B. R. Noack, M. Konig, and H. Eckelmann. On the transition of the cylinder wake. *Physics of Fluids*, 7(4):779–794, 1995.

[14] D. Stojkovic, P. Schon, M. Breuer, and F. Durst. On the new vortex shedding mode past a rotating circular cylinder. *Physics of Fluids*, 15(5):1257–1260, 2003.

[15] F. R. Hama. Three-dimensional vortex pattern behind a circular cylinder. *Journal of Aeronautical Sciences*, 24(2):156–158, 1957.

[16] C. H. K. Williamson. The existence of two stages in the transition to three-dimensionality of a cylinder wake. *Physics of Fluids*, 31(11):3165–3168, 1988.

[17] C. H. K. Williamson. The natural and forced formation of spot-like 'vortex dislocations' in the transition wake. *Journal of Fluid Mechanics*, 243:393–441, 1992.

[18] T. Leweke and C. H. K. Williamson. Three-dimensional instabilities in wake transition. *European Journal of Mechanics - B/Fluids*, 17(4):571–586, 1998.

[19] M. C. Thompson, T. Leweke, and C. H. K. Williamson. The physical mechanism of transition in bluff body wakes. *Journal of Fluids and Structures*, 15:607–616, 2001.

[20] M. Brede, H. Eckelmann, and D. Rockwell. On the secondary vortices in the cylinder wake. *Physics of Fluids*, 8:2117–2124, 1996.

[21] D. Barkley and R. Henderson. Three-dimensional Floquet stability analysis of the wake of a circular cylinder. *Journal of Fluid Mechanics*, 322:215–241, 1996.

[22] R. D. Henderson. Secondary instability in the wake of a circular cylinder. *Physics of Fluids*, 8(6):1683–1685, 1996.

[23] R. D. Henderson. Nonlinear dynamics and pattern formation in turbulent wake transition. *Journal of Fluid Mechanics*, 352:65–112, 1997.

[24] D. Barkley, L. S. Tuckerman, and M. Golubitsky. Bifurcation theory for three-dimensional flow in the wake of a circular cylinder. *Physical Review E*, 61(5): 5247–5252, 2000.

[25] H. M. Blackburn, F. Marques, and J. M. Lopez. Symmetry breaking of two-dimensional time-periodic wakes. *Journal of Fluid Mechanics*, 522:395–411, 2005.

[26] W. J. P. M. Maas, C. C. M. Rindt, and A. A. van Steenhoven. The influence of heat on the 3D-transition of the von Kármán vortex street. *International Journal of Heat and Mass Transfer*, 46(16):3069–3081, 2003.

[27] M. Ren, C. C. M. Rindt, and A. A. van Steenhoven. Experimental and numerical investigation of the vortex formation process behind a heated cylinder. *Physics of Fluids*, 16:3103–3114, 2004.

[28] G. J. Sheard, M. C. Thompson, and K. Hourigan. From spheres to circular cylinders: non-axisymmetric transitions in the flow past rings. *Journal of Fluid Mechanics*, 506:45–78, 2004.

[29] G. J. Sheard, M. C. Thompson, and K. Hourigan. From spheres to circular cylinders: the stability and flow structures of bluff ring wakes. *Journal of Fluid Mechanics*, 492:147–180, 2003.

[30] G. J. Sheard, M. C. Thompson, K. Hourigan, and T. Leweke. The evolution of a subharmonic mode in a vortex street. *Journal of Fluid Mechanics*, 534:23–38, 2005.

[31] G. J. Sheard, M. C. Thompson, and K. Hourigan. Subharmonic mechanism of the Mode C instability. *Physics of Fluids*, 17(111702), 2005.

[32] B. S. Carmo, S. J. Sherwin, P. W. Bearman, and R. H. J. Willden. Wake transition in the flow around two circular cylinders in staggered arrangements. *Journal of Fluid Mechanics*, 597:1–29, 2008.

[33] S. Kang, H. Choi, and S. Lee. Laminar flow past a rotating circular cylinder. *Physics of Fluids*, 11:3312–3321, 1999.

[34] D. Stojkovic, M. Breuer, and F. Durst. Effect of high rotation rates on the laminar flow around a circular cylinder. *Physics of Fluids*, 14(9):3160–3178, 2002.

[35] S. Mittal and B. Kumar. Flow past a rotating cylinder. *Journal of Fluid Mechanics*, 476:303–334, 2003.

[36] S. Mittal. Three-dimensional instabilities in flow past a rotating cylinder. *Journal of Applied Mechanics*, 71:89–95, 2004.

[37] R. El Akoury, M. Braza, R. Perrin, G. Harran, and Y. Hoarau. The three-dimensional transition in the flow around a rotating cylinder. *Journal of Fluid Mechanics*, 607:1–11, 2008.

[38] J. O. Pralits, L. Brandt, and F. Giannetti. Instability and sensitivity of the flow around a rotating cylinder. *Journal of Fluid Mechanics*, 650:513–536, 2010.

[39] L. J. P. Timmermans. *Analysis of spectral element methods with application to incompressible flow*. PhD thesis, Eindhoven University of Technology, The Netherlands, 1994.

[40] L. J. P. Timmermans, P. D. Minev, and F. N. van de Vosse. An approximate projection scheme for incompressible flow using spectral elements. *International Journal for Numerical Methods in Fluids*, 22:673–688, 1996.

[41] R. N. Kieft, C. C. M. Rindt, A. A. van Steenhoven, and G. J. F. van Heijst. On the wake structure behind a heated horizontal cylinder in cross-flow. *Journal of Fluid Mechanics*, 486:189–211, 2003.

[42] R. Kieft. *Mixed convection behind a heated cylinder*. PhD thesis, Eindhoven University of Technology, 2000.

[43] M. Ren. *Flow transition behind a heated cylinder*. PhD thesis, Eindhoven University of Technology, 2005.

[44] G. E. Karniadakis and G. S. Triantafyllou. Three-dimensional dynamics and transition to turbulence in the wake if bluff objects. *Journal of Fluid Mechanics*, 238:1–30, 1992.

[45] P. D. Minev, F. N. van de Vosse, L. J. P. Timmermans, and A. A. van Steenhoven. A second order splitting algorithm for thermally-driven flow problems. *International Journal of Numerical Methods for Heat & Fluid Flow*, 6(2):51–60, 1995.

[46] C. H. K. Williamson. Defining a universal continuous Strouhal-Reynolds number relationship for the laminar vortex shedding of a circular cylinder. *Physics of Fluids*, 31(10):2742–2744, 1988.

[47] C. H. K. Williamson and G. L. Brown. A series in $1/\sqrt{Re}$ to represent the Strouhal-Reynolds number relationship of the cylinder wake. *Journal of Fluids and Structures*, 12:1073–1085, 1998.

[48] S. Mittal and A. Raghuvanshi. Control of vortex shedding behind circular cylinder for flows at low Reynolds numbers. *International Journal for Numerical Methods in Fluids*, 35:421–447, 2001.

[49] H. Honji, S. Taneda, and M. Tatsuno. Some practical details of the electrolytic precipitation method of flow visualization. *Rep. Res. Inst. Appl. Math.*, 28:83–89, 1980.

[50] R. J. Adrian. Particle-imaging techniques for experimental fluid mechanics. *Annual Review of Fluid Mechanics*, 23:261–304, 1991.

[51] J. Westerweel. *Digital particle image velocimetry - theory and application*. PhD thesis, Delft University of Technology, Delft, The Netherlands, 1993.

[52] M. Raffel, C. E. Willert, S. T. Wereley, and J. Kompenhans. *Particle Image Velocimetry: A practical guide*. Springer Verlag, Berlin, Heidelberg, 2 edition, 2007.

[53] J. Westerweel and F. Scarano. Universal outlier detection for PIV data. *Experiments in Fluids*, 39:1096–1100, 2005.

[54] S. Herpin, C. Y. Wong, and J. Stanislas, M. Soria. Stereoscopic PIV measurements of a turbulent boundary layer with a large spatial dynamic range. *Experiments in Fluids*, 45:745–763, 2008.

[55] J. Jeong and F. Hussain. On the identification of a vortex. *Journal of Fluid Mechanics*, 285:69–94, 1995.

[56] H. Vollmers. Detection of vortices and quantitative evaluation of their main parameters from experimental velocity data. *Measurement Science and Technology*, 12:1199–1207, 2001.

[57] G. K. Batchelor. *An introduction to fluid dynamics*. Cambridge University Press, 2000.

[58] H. Choi, W.-P. Jeon, and J. Kim. Control of flow over a bluff body. *Annual Review of Fluid Mechanics*, 40:113–139, 2008.

[59] P. J. Strykowski and K. R. Sreenivasan. On the formation and suppression of vortex shedding at low Reynolds numbers. *Journal of Fluid Mechanics*, 218:71–107, 1990.

[60] A. Dipankar, T. Sengupta, and S. B. Talla. Suppression of vortex shedding behind a circular cylinder by another control cylinder at low Reynolds number. *Journal of Fluid Mechanics*, 573:171–190, 2007.

[61] C. H. Kuo, L. C. Chiou, and C. C. Chen. Wake flow pattern modified by small control cylinders at low Reynolds number. *Journal of Fluids and Structures*, 23: 938–956, 2007.

[62] O. Marquet, D. Sipp, and L. Jacquin. Sensitivity analysis and passive control of cylinder flow. *Journal of Fluid Mechanics*, 615:221–252, 2008.

[63] H. Sakamoto and H. Haniu. Optimum suppression of fluid forces acting on a circular cylinder. *Journal of Fluids Engineering*, 116:221–227, 1994.

[64] C. Dalton, Y. Xu, and J.C. Owen. The supression of lift on a circular cylinder due to vortex shedding at moderate Reynolds numbers. *Journal of Fluids and Structures*, 15:617–628, 2001.

[65] B. Ahlborn, M. L. Seto, and B. R. Noack. On drag, Strouhal number and vortex-street structure. *Fluid Dynamics Research*, 30:379–399, 2002.

[66] R. N. Kieft, C. C. M. Rindt, and A. A. van Steenhoven. The wake behaviour behind a heated horizontal cylinder. *Experimental and Thermal Fluid Science*, 19: 183–193, 1999.

[67] P. G. Drazin. *Introduction to Hydrodynamic Stability*. Cambridge University Press, 2002.

[68] P. K. Kundu and I. M. Cohen. *Fluid Mechanics*. Academic Press, 4th edition, 2008.

[69] A. Libchaber, C. Laroche, and S. Fauve. Period doubling cascade in mercury, a quantitative measurement. *Le Journal de Physique-Lettres*, 43:L211–L216, 1982.

[70] J.-C. Lin, P. Vorobieff, and D. Rockwell. Space-time imaging of a turbulent near-wake by high-image-density particle image cinematography. *Physics of Fluids*, 8 (2):555–564, 1996.

[71] C. Chyu and D. Rockwell. Evolution of patterns of streamwise vorticity in the turbulent near wake of a circular cylinder. *Journal of Fluid Mechanics*, 320:117–137, 1996.

[72] J. F. Huang, Y. Zhou, and T. Zhou. Three-dimensional wake structure measurement using a modified PIV technique. *Experiments in Fluids*, 40:884–896, 2006.

[73] F. Scarano and C. Poelma. Three-dimensional vorticity patterns of cylinder wakes. *Experiments in Fluids*, 47:69–83, 2009.

[74] P. J. Schmid. Applications of the dynamic mode decomposition to experimental data. *Experiments in Fluids*, 2011. DOI:10.1007/s00348-010-0911-3.

# Summary

### Transition of wire-disturbed cylinder wake flow

The transition of the flow behind bluff bodies has been the main topic of research for many decades. Despite the efforts of many scientist and engineers, understanding of the transition mechanism of wake flows behind both streamlined and bluff bodies is still a challenge.

The focus in this research is the modified flow regime in the wake of a circular cylinder. The modification is obtained by placing a very thin wire at a particular position in the cylinder wake. The occurring transitional flow is denoted as Mode-C transition, in comparison to Mode-A and Mode-B transition for the non-wired cylinder. The flow structures have been investigated both experimentally and numerically for different Reynolds numbers ($Re = 100 - 250$) using flow visualizations based on the tin-precipitation method, velocity measurements using Particle Image Velocimetry(PIV), and numerical simulations based on the Spectral Element method.

In the laminar two-dimensional flow regime ($Re = 100$), it was observed, both numerically and experimentally, that the wake of the cylinder is taking different trajectories with respect to the wire position. A hypothesis was formulated about the reasons of the wake deflection using a Point Vortex Model. The hypothesis is supported with the assessment of vortex trajectories, strengths, lift and drag characteristics. It is concluded that the deflection of the wake is primarily caused by a modification of the vortex arrangement in the wake. This modified vortex arrangement is caused by different formation times of the upper and lower vortices, by different vortex strengths, or by both.

A three-dimensional transition of the wired cylinder flow was observed for $Re > 170$. This transition is characterized by the so-called Mode-C instability. Analysis of the experimental results shows that this Mode-C instability consists of secondary vortices with a period-doubling character, i.e. the secondary vortices alternate sign from one shedding cycle to the next. It is shown that a feedback mechanism of the streamwise vortices between the two consecutively shed upper von Kármán vortices causes the period-doubling character of the wake.

The analysis of Mode-C transition was further extended using the data from com-

prehensive PIV experiments. The three-dimensional wake structure and vortex dynamics were investigated with a particular focus on the energy distribution of the wake, vortex strengths and vortex trajectories. The secondary vortices are shown to be counter-rotating vortex pairs with a spanwise wavelength of $\lambda_z/D = 2.16$.

In the final stage of the research, experiments have been performed to evaluate the wake behind a rotating cylinder, particularly focusing on the so-called Shedding Mode II regime. In literature only numerical proof is found for the existence of this Shedding Mode II for which a single vortex is shed with a much lower frequency compared to the non-rotating case. Both flow visualization and PIV techniques were used to investigate this kind of flow. Shedding Mode II has experimentally been detected for a Reynolds number of $Re = 100$ in the same rotation rate regime as in the numerical studies.

# Acknowledgements

This thesis came into existence with four years of work in the Energy Technology Section at Eindhoven University of Technology. I enjoyed this period of my life very much with the company of several colleagues and friends. In this last section I would like to thank to those who have helped me and created many good memories during these years.

First of all, I would like to express my gratitude to my supervisors prof.dr.ir. Anton van Steenhoven and dr.ir Camilo Rindt for their supervision and support throughout these years. Their constant encouragement and confidence in me helped me to a great extent and kept me motivated for finishing this work. Thank you for your extremely friendly attitude and openness too.

I sincerely thank the Reading Committee members, prof.dr.ir. Gert-Jan van Heijst, prof.dr. M. Fevzi Ünal and prof.dr.ir. Jerry Westerweel for their assessment and valuable comments on my thesis. I would also like to thank to dr. Flavio Giannetti, dr. Luca Brandt and dr. Jan Pralits for inspiring the work about rotating cylinder.

The financial support from the Foundation for Fundamental Research on Matter (FOM) is gratefully acknowledged.

A key factor for a good experimental study is the technical support. At this point, I would like to sincerely thank all staff members of TFE Lab, especially Paul, Henri, Frank, Jan, Geert-Jan and Theo. They were all helpful when needed and without their assistance this thesis wouldn't be achieved. I would also like to thank to Ad Holten from Faculty of Applied Physics for providing me the data acquisition software to perform the experiments. Without his valuable help, things would have been very difficult for me. I would like to express my sincere gratitude to Linda who has been very kind and helpful for me from day one.

My roommates and the fellow ET (ex-)members, Rudi, Ziemowit, Henk, Konstantin, Natascha, Srinidhi, Petra, Beste, Boris, Lakhdar, Zhipeng, JungHan, Eldhose, Joy, Erik, Esubalew, Lucie and Kiran, thank you all for your friendship, stimulating scientific discussions as well as equally stimulating chats about anything during coffee breaks. Couple of years ago, we have started a tradition among PhD students of ET by organizing 'events' and appointing CEO(Chief Event Organizer) for each event. I enjoyed a lot during every event; early-work and best lunch competitions,

cycling, swimming, ice skating, bowling, cricket, football, poker, cooking dinner, movie etc. It was all fun.

Bihter, Çiçek & Tanır, Defne & Ege & Semih, Ela, Irmak, Sandra & Tarkan, Tuba, Ahmet Koray, Ahmet E., Aydın, Başar, Can A., Can N., İlkin, İzzet, Kamil, Kurtuluş, Mehmet, Tuncay, Serdar; thank you very much for your kind friendship. Special thanks to the (ex-)members of 'The Endings'; Gözde, Hilal, Barış Y., İsa, Koray, Marco and Uğur, I enjoyed every moment of your rehearsals and still enjoying. I would like to express my special gratitude to Atike & Koray, Layka, Barış Y., Ergün and İsa for all the wonderful moments, for being available during difficult times to share my mood and for your sincere support. I feel myself very lucky to know people like you all. Atike, I thank you again for your time you've spent on designing my thesis cover.

At the very end, I would like to present my greatest gratitude to my family; my parents Hediye and Beyazıt and my brother Sinan. There are no words to express my gratitude to them who have unconditionally loved and supported me all these years so I will just say: Thank you for everything.

Doktora sürecim boyunca uzakta olsalar bile benim her zaman yanımda olduklarını hissettiren sevgili annem Hediye ve babam Beyazıt ile canım kardeşim Sinan'a çok teşekkür ederim. Onlara olan minnettarlığımı ifade edecek söz bulamadığımdan sadece şunu söylemek istiyorum: Herşey için çok teşekkür ederim, iyi ki varsınız.

İlhan Yıldırım
Eindhoven, May 2011

# Curriculum Vitae

İlhan Yıldırım was born in Lofça, Bulgaria on July 2, 1980. He studied Aeronautical Engineering at Istanbul Technical University, Turkey and got his B.Sc. degree in 2003. Afterwards, he continued his studies in the same department and got his M.Sc. degree in Aerospace Engineering in 2006. His M.Sc. thesis focused on the experimental investigation of wake interaction of a cylinder behind an airfoil. In the meantime, he worked as a Research Engineer in the Rotorcraft Design Center at Istanbul Technical University. In December 2006, he started to work on his Ph.D. project in Energy Technology Section of Mechanical Engineering Faculty of Eindhoven University of Technology under the supervision of prof. dr. ir. A.A. van Steenhoven and dr. ir. C.C.M. Rindt. The results of this work are described in this thesis.